POLITECNICO DI MILANO

SCUOLA DI INGEGNERIA CIVILE, AMBIENTALE E TERRITORIALE

CORSO DI LAUREA MAGISTRALE IN INGEGNERIA CIVILE-CIVIL ENGINEERING

BEHAVIOUR AND DESIGN OF COMPOSITE STEEL-CONCRETE SLABS

Relatore: Prof. Massimiliano Bocciarelli

Relatore: Prof. Gianluca Ranzi

Tesi di laurea magistrale di:
Riccardo Luzzi Matr. 819034

Anno Accademico 2014/2015

To my family,

for its support throughout my life

Contents

Figures...4
Tables...8
Abstract...9
Abstract...10
Introduction...11
Introduction...11
Background...11
Objectives of the study...13
Organization of the thesis...14
1 Literature Review...15
1.1 Introduction...15
1.2 Background...15
1.2.1 Historical Background...18
1.3 Ultimate behaviour...19
1.4 Time-dependent behaviour...25
2 Materials...30
2.1 Introduction...30
2.2 Concrete...30
2.2.1 Time Dependent Deformation of concrete...30
2.2.2 The elastic deformation of concrete...31
2.2.3 Creep...31
2.2.4 Shrinkage...33
2.3 Numerical methods for time analysis of concrete...35
2.3.1 The superposition integral...35
2.3.2 The effective modulus method (EMM)...36
2.3.3 The age-adjusted effective modulus method (AEMM)...36
2.3.4 The Step-by-step method (SSM)...38
2.4 The non-uniform shrinkage on composite slab cross-section...42
2.4.1 Comparison with experimental results...44
2.5 Steel...46
2.5.1 Conventional, non-prestressed reinforcement...46
2.5.2 Metal Sheeting...47
3 Design of composite slab...49
3.1 Introduction...49
3.2 Limit state requirements specified by Australian draft code AS2327...50
3.2.1 Ultimate limit state: Flexure...50
3.2.2 Ultimate limit state: Vertical shear...53
3.2.3 Serviceability limit state: deflection...53
3.2.4 Slab deflection by simplified calculation...56

3.2.4.1 Short term deflection 56
3.2.4.2 Creep deflection 59
3.2.4.3 Shrinkage deflection 60
3.3 Parametric study 61
3.3.1 Considerations on the governing limit state for the design of composite slabs 62
3.3.2 Considerations on the total deflection 78
4 Finite Element Model 81
4.1 Introduction 81
4.2 Euler-Bernoulli beam model and weak form 81
4.2.1 Field displacements 82
4.2.2 Equilibrium 84
4.3 Nonlinear Finite element formulation 87
4.3.1 Shape Functions 87
4.4 Nonlinear analysis using the Newton-Raphson method 91
4.4.1 Overview of the Newton-Raphson Method 91
4.5 Cross-sectional modelling 100
4.5.1 Concrete area discretization 100
4.5.2 Reinforcement discretization 101
4.5.3 Metal sheeting discretization 102
4.6 Validation of the finite element model 103
5 Refined Design Analysis 105
5.1 Introduction 105
5.2 Design of the thickness using FEA 105
5.3 Comparisons on deflection between FEA and code approach 107
5.3.1 General remarks 107
5.3.2 Incremental deflection 107
5.3.3 Total deflection 109
5.3.4 Considerations on uniform shrinkage model 110
6 Conclusions 113
6.1 Introduction 113
6.2 Concluding remarks 113
6.3 Recommendations for future work 117
References 118
A1 Material Properties 122
A.1.1 Concrete 122
A.1.1.1 Strength (AS3600-2009, 3.1.1) 123
A2 Additional Results Chapter 3 127
A2.1 Influence of the live load on total deflection 127
A2.1.1 Profile 1 127
A2.1.2 Profile 2 128
A2.2 Influence of the thickness of the profiled on total deflection 129
A2.2.1 Profile 1 129
A2.2.2 Profile 2 130

A3 Additional Results Chapter 5 131
A3.1 Comparisons between FEA and code for slabs with profile 2 131
A3.1.1 Design of the thickness for profile 2 using FEA 131
A3.1.2 Comparisons on incremental deflection for profile 2 132
A3.1.3 Comparisons on total deflection for profile 2 133
A3.1.4 Comparisons with uniform shrinkage distribution 134

Figures

Fig 1.1 Composite slabs 15

Fig 1.2 Propped slab 16

Fig 1.3 Elements of a composite slab and notations 16

Fig 1.4 Examples of steel sheeting profiles 17

Fig 1.5 Types of shear connections 18

Fig 1.6 Shear-bond failure (Porter , Ekberg , 1975) 20

Fig 1.7 Typical set-up for testing slab elements (Porter , Ekberg , 1975) 21

Fig 1.8 Shear-bond failure relationship (Porter , Ekberg, 1975) 22

Fig 1.9 Horizontal force equilibrium for steel profile (Stark, Brekelmans, 1990) 23

Fig 1.10 Moment-distance from support on partial shear connection strength model (Star , Brekelmans, 1990) 24

Fig 1.11 Shrinkage deflection theory (Montgomery, Kulak, Shwartsburd, 1983) 25

Fig 1.12 Typical shrinkage profile specimens. (Gilbert, Bradford, Gholamhoseini, Chang, 2011) 27

Fig 1.13 Qualitative uniform shrinkage distribution for slab exposed on both sides. 28

Fig 1.14 Qualitative linear shrinkage distribution for composite slab. (Ranzi, Leoni, Zandonini, 2012) 29

Fig 2.1 Concrete strain components (Gilbert, Ranzi, 2010) 31

Fig 2.2 Time-stress history (Gilbert, Ranzi, 2010) 38

Fig 2.3 Time discretization (Gilbert, Ranzi, 2010) 38

Fig 2.4 Composite samples for shrinkage measurement (Al-Deen, Ranzi, 2015b) 42

Fig 2.5 Total long-term measured at different instances in time through the cross-section 42

Fig 2.6 Strain variables describing non-uniform free shrinkage on composite slabs . 44

Fig 2.7 The metal sheeting 47

Fig 2.8 Elastic-plastic constitutive law of steel 47

Fig 2.9 Geometry of the profiled steel sheeting 48

Fig 3.1 Stress distribution for sagging bending if the neutral axis is above the steel sheeting (Draft AS2327) 52

Fig 3.2 Stress distribution for sagging bending if the neutral axis is in the steel sheeting (Draft AS2327) 52

Fig 3.3 Static configuration of the composite slab 54

Fig 3.4 Stress distribution for the computation of cracked cross-section's properties 59

Fig 3.5 Geometry of the profiled sheeting used in the parametric study 61

Fig 3.6 Design ratios and thickness depth for a propped slab with metal sheeting 1 in the case of model A and model B (Q = 3 kPa, tincr=28 days) 63

Fig 3.7 Design ratio and thickness depth for a propped slab with metal sheeting 1 in the case of model C (Q = 3 kPa, tincr=28 days) 65

Fig 3.8 Design ratios and thickness depth for an unpropped slab with metal sheeting 1 for the models A, B and C (Q = 3 kPa, tincr=28 days) 66

Fig 3.9 Design ratios and thickness depth for a propped slab with metal sheeting 2 for the models A, B and C (Q = 3 kPa, tincr=28 days) 67

Fig 3.10 Design ratios and thickness depth for an unpropped slab with metal sheeting 2 for the models A, B and C (Q = 3 kPa, tincr=28 days) 68

Fig 3.11 Design ratios and thickness depth for a propped slab with metal sheeting 1 for the models A, B and C (Q = 3 kPa, tincr=56 days) 69

Fig 3.12 Design ratios and thickness depth for a propped slab with metal sheeting 1 for the models A, B and C (Q = 3 kPa, tincr=84 days) 70

Fig 3.13 Design ratios and thickness depth for a propped slab with metal sheeting 1 without considering the incremental limit as a design criterion (Q = 3 kPa) 72

Fig 3.14 Comparisons among thickness depth computed using the models A, B and C for the profile 1 (Q = 3 kPa) 73

Fig 3.15 Comparisons among thickness depth computed using the models A, B and C for the profile 2 (Q = 3 kPa) 74

Fig 3.16 Comparisons among incremental deflection computed using the models A, B and C for the profile 1 (Q = 3 kPa) 75

Fig 3.17 Comparisons among incremental deflection computed using the models A, B and C for the profile 1 (Q = 3 kPa), without considering the minimum slab thickness limit for 120 mm 76
Fig 3.18 Comparisons among incremental deflection computed using the models A, B and C for the profile 2 (Q = 3 kPa) 76
Fig 3.19 Comparisons among incremental deflection computed using the models A, B and C for t_{incr}=56 days (Q = 3 kPa, profile 1) 77
Fig 3.20 Comparisons among incremental deflection computed using the models A, B and C for t_{incr}=84 days (Q = 3 kPa, profile 1) 77
Fig 3.21 Comparisons among total deflection computed using the models A, B and C for the profile 1 (Q = 3 kPa) 78
Fig 3.22 Comparisons among total deflection computed using the models A, B and C for the profile 2 (Q = 3 kPa) 79
Fig 4.1 Displacement field 82
Fig 4.2 Member loads and nodal actions 84
Fig 4.3 Shape functions used for the approximation of u 88
Fig 4.4 Shape functions used for the approximation of v 89
Fig 4.5 7-dof Euler Bernoulli beam 89
Fig 4.6 Newton-Raphson Method (Ranzi, Gilbert, 2014) 93
Fig 4.7 Concrete strip area 100
Fig 4.8 Cross-sectional discretization and stress diagram 101
Fig 4.9 Circular segment's area 102
Fig 4.10 Geometric quantities of the metal sheeting 102
Fig 5.1 Comparison on the designed depth between Code and FEA for profile 1, with incremental check (Q=3 kPa) 106
Fig 5.2 Comparison on the designed depth between Code and FEA for profile 1, with no incremental check (Q=3 kPa) 106
Fig A- 1 Comparisons among total deflection computed using the models A, B and C for the profile 1 127

Fig A- 2 Comparisons among total deflection ratio computed using the models A, B and C for the profile 2 128
Fig A- 3 Comparisons among total deflection computed using the models A, B and C for the profile 1 129
Fig A- 4 Comparisons among total deflection computed using the models A, B and C for the profile 2 130
Fig A- 5 Comparison on the designed depth between Code and FEA for profile 2, with incremental check (Q=3 kPa) 131
Fig A- 6 Comparison on the designed depth between Code and FEA for profile 2, with no incremental check (Q=3 kPa) 131

Tables

Table 2-1 Validation of the linear shrinkage........45
Table 2-2 Geometric properties of the profiled steel sheeting........48
Table 3-1 Load combinations for the evaluation of deflections in propped construction........55
Table 3-2 Load combinations for the evaluation of deflections in unpropped construction........55
Table 4-1 Function arguments and weighting factors for the Gauss-Legendre formulae (Ranzi, Gilbert, 2014)........97
Table 4-2 Validation of the finite element mode........103
Table 4-3 Validation of the finite element model........104
Table 5-1 Comparison on the incremental deflection between Code and FEA for profile 1 (linear shrinkage, Q=3 kPa)........108
Table 5-2 Comparison on the total deflection between Code and FEA for profile 1 (linear shrinkage, Q=3 kPa)........109
Table 5-3 Comparison on the incremental deflection between Code and FEA for profile 1 (uniform shrinkage, Q=3 kPa)........110

Table A- 1 Value for the basic creep coefficient........124
Table A- 2 Comparison on the incremental deflection between Code and FEA for profile 2 (linear shrinkage, Q=3 kPa)........132
Table A- 3 Comparison on the total deflection between Code and FEA for profile 2 (linear shrinkage, Q=3 kPa)........133
Table A- 4 Comparison on the incremental deflection between Code and FEA for profile 2 (uniform shrinkage, Q=3 kPa)........134

Abstract

Composite steel-concrete slabs are widely used in framed buildings and car parks for their ability to span large distances and their speed in construction.
Despite their wide use, relatively little research has been undertaken on the in-service behaviour of such slabs.
Recent research has identified the occurrence of a shrinkage gradient through the thickness of a composite slab produced by inability of the concrete to dry from its underside due to the presence of the profiled steel sheeting.
Service recommendations specified in available design guidelines do not consider this effect.

This thesis is concerned with the behaviour of simply-supported composite steel-concrete slabs with particular attention devoted to their long-term behaviour and how this is influenced by concrete shrinkage effects. For this purpose, three different service design approaches, reflecting the current state of the art in design, have been considered and vary for the recommended procedure specified to account for shrinkage, i.e. one approach makes use of a shrinkage gradient over the slab thickness in the deflection calculations, one procedure requires the use of a uniform shrinkage profile and the remaining case does not require shrinkage deflections prediction to be carried out

A finite element model has been developed to predict the service response of composite floor slabs. This numerical model has been validated against experimental results available in the literature and it has been used to evaluate the accuracy of available simplified design service models

Abstract

Le solette composte in acciaio-calcestruzzo sono una soluzione largamente diffusa in ambito strutturale per la loro economicità e capacità di coprire luci di grande dimensione. Nonostante il loro elevato utilizzo, relativamente poca ricerca è stata effettuata nella valutazione del comportamento in esercizio di tali strutture, in particolare sull' influenza del ritiro nell'inflessione.

Solamente studi recenti hanno quantificato il profilo di ritiro da essiccamento lungo lo spessore della soletta, il quale risulta notevolmente influenzato dalla presenza della lamiera grecata. Il profilato metallico non permette l'evaporazione dell'acqua dall'intradosso dell'elemento, determinando un gradiente di ritiro lungo la sezione.

Le attuali normative internazionali sulle solette composte non considerano tale fenomeno e rimandano al profilo di ritiro uniforme utilizzato nell'analisi di strutture in calcestruzzo armato ordinario. In alternativa, rendono disponibile trascurare gli effetti del ritiro sull'inflessione.

Questa tesi valuta il comportamento a lungo termine di solette composte semplicemente appoggiate e identifica i parametri chiave che ne influenzano il progetto. Particolare attenzione e' stata rivolta all'influenza del ritiro sull'inflessione in condizioni di esercizio.

Sono stati considerati e confrontati tre diversi modelli progettuali disponibili nelle attuali normative e in letteratura. Questi modelli differiscono per la modalità in cui tengono in conto del ritiro nella sezione della soletta: gradiente da ritiro, ritiro uniforme, assenza del ritiro.

A scopo ti tali analisi sono stati implementati modelli numerici in grado di analizzare il comportamento strutturale delle solette composte. I modelli sono stati infine confrontati tra loro per valutare la loro influenza sul design.

Introduction

Introduction

This thesis investigates the instantaneous and time-dependent behaviour of simply supported composite steel-concrete slabs. Particular attention is given to a review of the design serviceability models available in current international guidelines and literature, which mainly differ for the approach used to account for shrinkage effects in the deflection calculation. This study represents a preliminary evaluation of the shrinkage effects on the response of composite steel-concrete slabs.

The significance of this work is outlined in the next paragraph, followed by the objectives of the thesis, the scope of the work and the thesis layout.

Background

Composite steel-concrete slabs are widely used in framed buildings and car parks for their ability to span large distances and for being economical. With this form of construction, the concrete is poured on a profiled steel sheeting which acts as permanent formwork and, once the concrete hardens, behaves as an external reinforcement. Unlike steel reinforcing bars, which are completely inside the concrete, the sheeting is not embedded in the concrete and the composite action is highly dependent on the interface properties between the concrete and sheeting. The use of the steel sheeting allows faster construction when compared to the use of plywood formwork, because the latter has to be removed and cleaned after curing. It is common practice in Australia to use the steel sheeting as a sacrificial formwork because able to reduce erection costs.

Most research carried out to date has focussed on the ultimate behaviour of composite slabs. For example, experimental studies of composite steel-concrete slabs have involved short-term load test for the characterization of strength and ductility and for the characterisation of possible failure modes. Relatively little research has been undertaken on their in-service behaviour. Long-term tests aimed at studying the time-dependent response of the slab to service loads have been rarely performed. In particular, further investigations should be undertaken about the influence of the shrinkage on the deflection of composite slabs. As concrete shrinks, it gradually compresses the steel sheeting. In order to maintain equilibrium in the section, the steel decking applies an equal and opposite tensile force on the concrete section. This tensile force is eccentric to the centroid of the concrete cross-section and it generates curvature on the cross section. Furthermore, shrinkage effects could generate cracks on the slab: the higher the number of cracks the higher is the deflection of the slab.

Recent research has identified the occurrence of a shrinkage gradient taking place through the slab thickness produced by the inability of the concrete to dry from its underside.

In this context, this Serviceability models, which are available in the current guidelines, do not consider these features. Some of them enable under particular conditions to omit deflection calculation and, when not complying with these requirements, permit the service slab design to be carried out without considering the effects produced by shrinkage. Other approaches are based on considering a uniform shrinkage profile in which the shrinkage strain calculation is based on concrete codes.

A different approach, here pursued, is to account for the occurrence of non-uniform shrinkage.

Objectives of the study

Following the discussion of the above paragraph, the main objectives of this thesis are as follows:

1. to evaluate the most critical limit state for the design of composite slabs (in accordance with international guidelines);
2. to identify the influence of using different serviceability design procedures (varying for the specifications related to shrinkage effects) on the design of composite slabs;
3. to develop a finite element model capable of predicting the service response of composite floor slabs and to validate it against experimental results available in the literature. This numerical model will also be used to evaluate the accuracy of available simplified design service models;
4. to perform an extensive parametric study to evaluate the key variables governing the design considering a wide range of realistic design scenarios.

Organization of the thesis

This thesis consists of 6 chapters and three appendices as detailed below:

Chapter 1 reviews the current literature about the behaviour of composite slabs.

Chapter 2 describes the properties of the composite slabs materials and illustrates the constitutive laws adopted in the numerical models.
In Chapter 3 the design limit states for composite slabs according to the Australian draft code (AS32327) are described. The code formulation has been numerically implemented. It has been used for a review of the governing limit state for the design of composite slabs and for comparisons among the different serviceability approaches.

The formulation and the validation with experimental results of the finite element model (FEA), is presented in chapter 4.

In Chapter 5 the FEA is applied to the design of composite slabs and the results achieved are compared with the recommendation of the current draft of the Australian composite code (AS32327 Draft, 2015).

The conclusion drawn from this thesis are presented in chapter 6 and some recommendations for future work are proposed.

In appendix A1 the material properties according to the Australian Standard code for concrete (AS3600, 2009) are presented.

In appendix A2 and A3 additional results are presented for the comparisons outlined in Chapter 3 and 5 respectively.

1 Literature Review

1.1 Introduction

This chapter provides a review of the literature on composite slabs. Introductory remarks are outlined in the next paragraph. The review of work carried out to date on the ultimate response of composite slab is provided in paragraph 1.3, followed by the research dealing with their service behaviour (paragraph 1.4).

1.2 Background

Composite concrete floor slabs with profiled steel sheeting are commonly used in the construction of frame structures (figure 1.1a). The steel sheeting is normally continuous over two spans between the supports and has two main roles in this system: it serves as a permanent formwork supporting the wet concrete during construction (figure 1.1b) and it acts as external reinforcement for the slab.

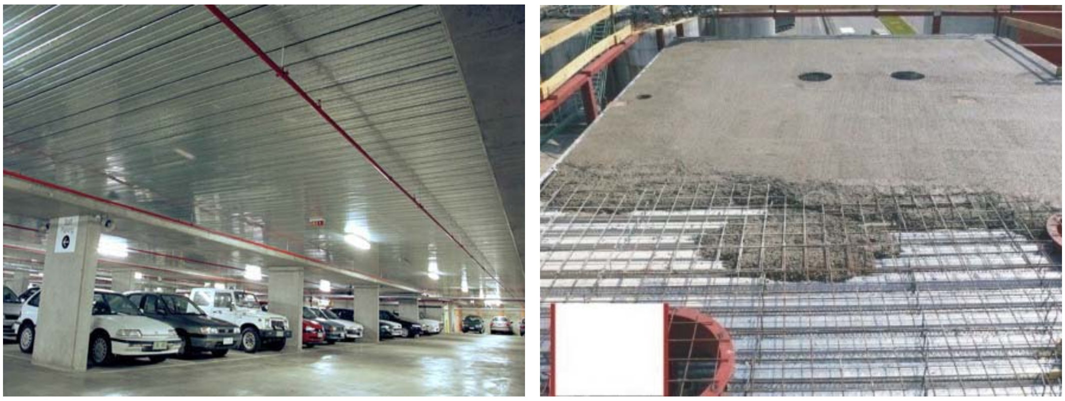

(a) Composite slab and beam floor system (b) Casting stage

Fig 1.1 Composite slabs

During the construction stage the steel sheeting can be supported by means of props (figure 1.2). Such supports are left in place until the concrete has developed adequate resistance.

Fig 1.2 Propped slab

Additional reinforcement might be included in the concrete slab, if the strength provided by the steel sheeting is not sufficient

Composite slabs are commonly one-way. It means that flexural action is significant only in the direction of the ribs. The direction of the ribs defines the longitudinal direction of the slab. The longitudinal length of the slab is referred to as span length L. The transversal direction is referred to as slab width b. The elements of a composite slab and the notations are shown in figure 1.3:

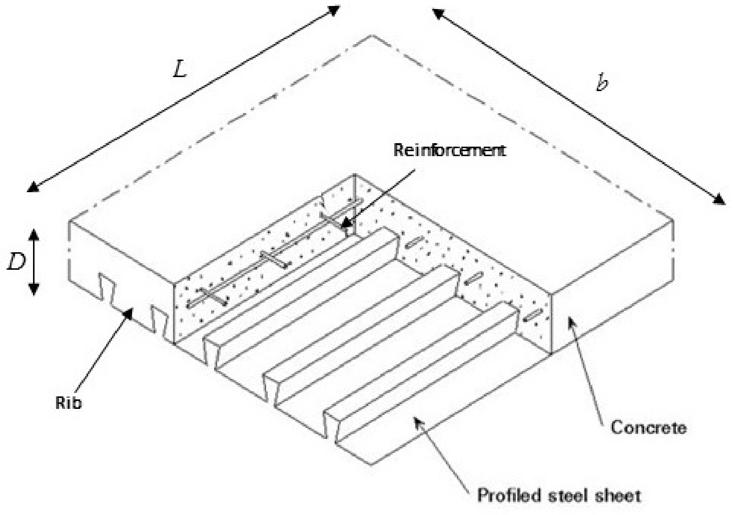

Fig 1.3 Elements of a composite slab and notations

There are many types of profiled steel sheeting used in construction of composite slabs. The shape and thickness of a profiled sheeting are selected depending on the span length, the resistance and stiffness required in the construction and composite stage.

The metal sheeting is available in different profiles, such as re-entrant or trapezoidal ones as shown in figures 1.4:

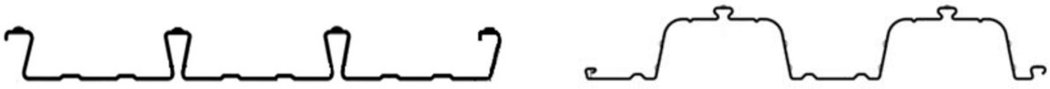

(a) Re-entrant Type Profile (b) Trapezoidal profile

Fig 1.4 Examples of steel sheeting profiles

The composite action between the metal sheeting and the hardened concrete depends on the transmission of horizontal shear stresses acting on the interface between concrete and steel sheeting (Stark, 1978; Johnson, 2004; Ohlers, Bradford, 1999). The transmission of the horizontal shear stresses can be provided by different types of shear connection. The first type is the natural bond, which is the chemical interaction between the concrete and the steel. It develops when concrete hardens. The second type is the frictional interlock, where shear stress is transferred by friction. This is provided by re-entrant profiles. Another shear connection is the mechanical interlock, which is provided by pressing dimples or ribs. A fourth type is the end anchorages. The end of a sheet is anchored on a steel beam by welding studs or other devices. The types of shear connection are depicted in figure 1.5.

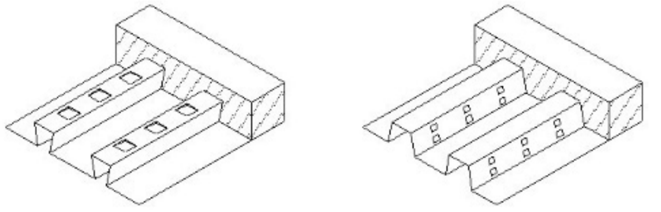

(a) Mechanical interlock

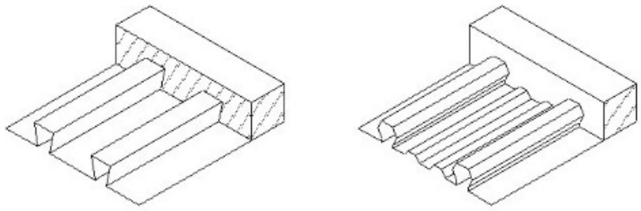

(b) Frictional interlock

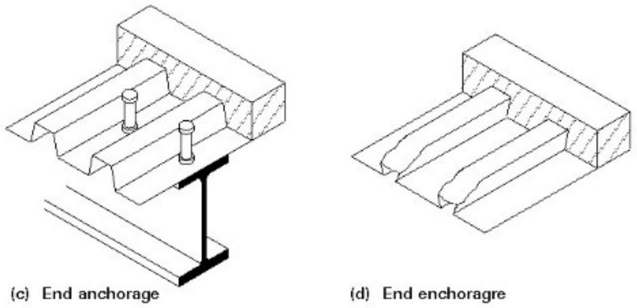

(c) End anchorage

(d) End enchoragre

Fig 1.5 Types of shear connections

1.2.1 Historical Background

Composite concrete dated back to the United States of America where "Keystone" steel decking was developed by Detroit Steel and marketed by the H.H Robertson Company (Krell, 1977). At this time, it did not act as a composite deck, but rather the steel sheeting acted as a sacrificial formwork for the concrete slab.

Shuster (Schuster, 1972) states that the first metal sheeting to rely a composite action to carry load was produced in 1950 by "Cofar", the deck achieved this composite action through the welding of wires onto the metal sheeting surface.

By the early 1960's more sophisticated sheeting were introduced, however due to the complexity of their profile, popularity was limited (Taplin, 1992). By the mid to late

1960s considerable research was undertaken in order to improve upon the performance of the profiles already in use; design was now based upon an allowable bond stress approach. Composite slabs became very popular by the early 1970s which was attributed to their weight savings and the simplicity in which electrical cabling could be installed through the utilization of the recesses in the profiled sheeting.

Composite slabs were introduced into high rise construction in Australia in the 1970's (Taplin, 1992), however there was a decline in popularity towards the end of the decade. With the resurgence in commercial building activity in the late 1980's as well as the subsequent rise in conventional formwork costs, composite slabs became a popular floor system. With an increase in popularity came an interest in the study of the fundamental behaviour of the system. Research into ductility and bond characteristics was then used in an analytical model to predict slab behaviour (Patrick, Poh, 1990; Poh, Attard, 1991), as a result of this Australian research both Australian manufacturers that existed at this time produced new profiles, Lysaght produced Bondeck II and Stramit produced Condeck HP.

There is now a wide range of sheet profiles world-wide as advances have been made in design procedures. The year 1982 hailed the first appearance of The British Standard for the design of composite concrete floors, which was followed by other relevant code such as Eurocode 4 at later dates.

1.3 Ultimate behaviour

Most research carried out to date on composite slabs has focussed on their ultimate behaviour.

Porter and Ekberg (Porter, Ekberg, 1975) identified three main failure modes governing the composite slab's behaviour and these consist of flexural failure of an under-reinforced section, flexural failure of an over-reinforced section and shear bond failure.

Flexural failure modes are similar to those of an ordinary reinforced concrete slab, in which failure of an under-reinforced section is characterized by yielding of the sheeting, while failure on an over-reinforced section is characterized by crushing of concrete in compression.

The longitudinal shear failure is due to shear at the steel-concrete interface and it is the most common type of failure for medium-span slabs at the ultimate limit state.
Load test carried out on full scale composite slabs have shown that significant slip between the metal sheeting and the concrete occurs at relatively high load levels (Porter, Ekberg, 1975; Ong, Mansu, 1986; Poh, Attard, 1991; Abdullah, Samuel Easterling, 2009).
The slippage causes a loss of composite action over the slab's segment taken as the shear span length *L'*. The shear span length is commonly determined by equating the mid-span bending moment obtained in a four-point bending case to that of a uniform loading case. This will result in $L'=L/4$. However, some researchers propose that it should be at one third of the length of the slab ($L'=L/3$) (Tenhovuori, Karkkainen, Kanerva, 1996; Tehnovuori, Leskela, 1998; Veljkovic, 2000).

For a four-point bending test, the shear span is the length from the support to the point load. As shown in figure 1.6, a diagonal crack in the concrete is formed near the load points (Porter, Ekberg, 1975).

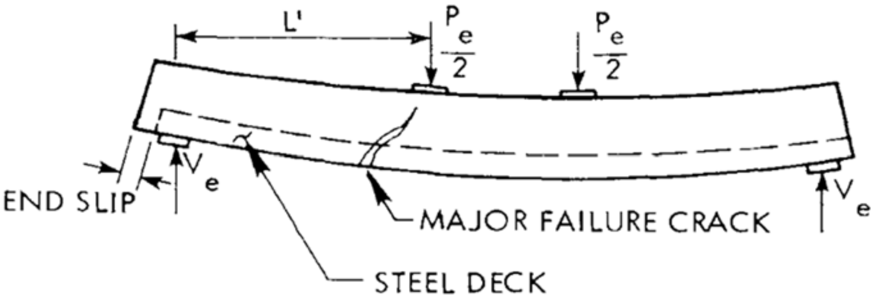

Fig 1.6 Shear-bond failure (Porter , Ekberg , 1975)

Eurocode 4 (EN 1994-1.1, 2004) gives two methods to evaluate the longitudinal shear capacity of composite slabs, known as the *m-k* and *partial shear connection* methods. In both the methods, the longitudinal shear capacity is assessed by using full scale laboratory tests to measure slab performance (figure 1.7). Full scale slab tests are necessary, because the longitudinal shear capacity is dependent on the geometry and flexibility of the particular type of steel sheeting, including the size and spacing of the embossment on the decking, as well as on the slenderness of the slab. The set-up of the test is showed in the figure below:

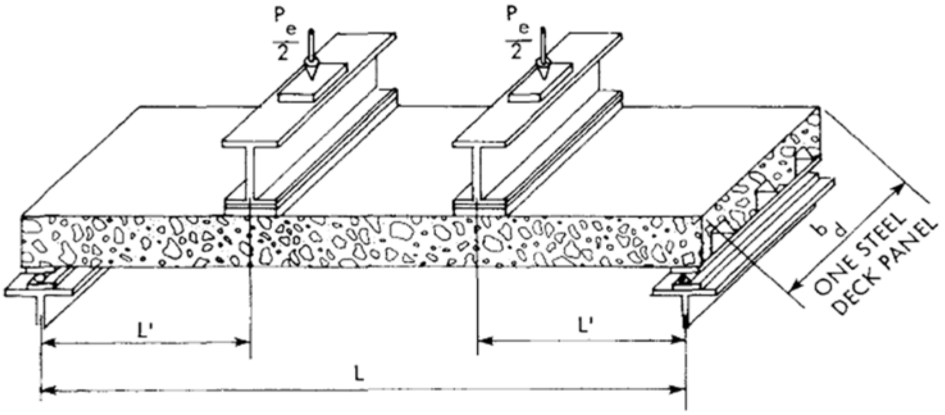

Fig 1.7 Typical set-up for testing slab elements (Porter , Ekberg , 1975)

The *m-k method* is mainly based on the work of Porter and Ekberg (Porter, Ekberg, 1975). They proposed the following shear stress design equation:

$$\frac{V_u\, s}{bd\sqrt{f_c'}} = \frac{m\,\rho\, d}{L'\,\sqrt{f_c'}} + k$$

where V_u is the ultimate shear force, s is the spacing of the shear transferring devices, ρ is the reinforcement ratio, d is the effective depth from the compression fibre to the metal sheeting centroid.

A plot was made of the parameter $V_e\ s/bd\sqrt{f_c'}$ and $\frac{\rho d}{L'}\sqrt{f_c'}$, as shown in figure 1.8

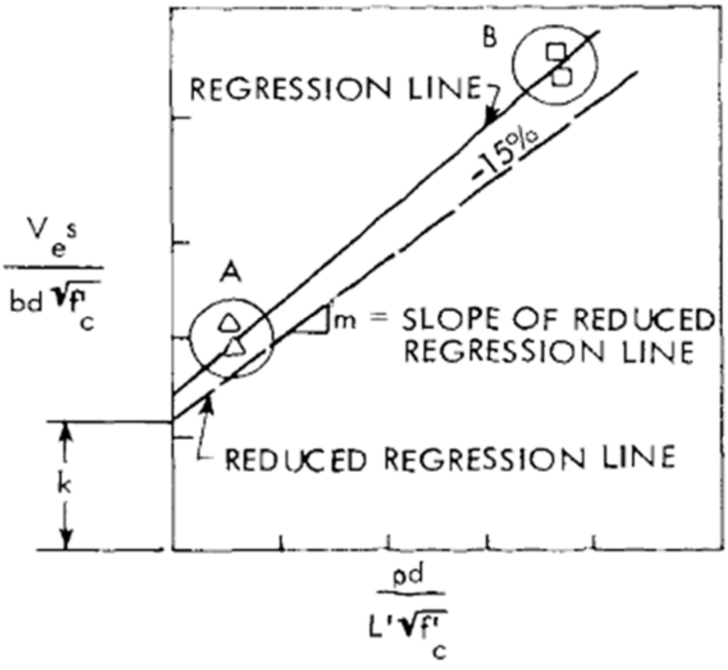
B
REGRESSION LINE
-15%
A
m = SLOPE OF REDUCED REGRESSION LINE
REDUCED REGRESSION LINE
$\frac{V_e^s}{bd\sqrt{f'_c}}$
k
$\frac{\rho d}{L'\sqrt{f'_c}}$

Fig 1.8 Shear-bond failure relationship (Porter , Ekberg, 1975)

A similar relationship was proposed by (Schuster, 1972). The two formulae represent straight lines of general equation:

$$y = m\,x + k$$

The slope m and the intercept k was determined by a linear regression.

Although the *m-k method* results contain the influence of all contributing parameters such as materials properties, slab geometry, longitudinal shear strength the frictional effects of supports reaction and any end anchorage; it is in fact not possible to separate the effects of any one parameter from the others.

Another major disadvantage of the *m-k method* is that it is not based on a mechanical model, then it is greatly test-dependent and a new set of full scale tests are required for any change of sheeting profile, design thickness, embossment type, end anchorage, etc. Other weaknesses related to the lack of a mechanical model are discussed by Bode and Sauerborn (Bode, Dauwell, 1999) and Bode and Dauwell (Bode, Sauerborn, 1992).

In the *partial shear connection method,* proposed firstly by Stark and Brekelmans (Stark, Brekelmans, 1990), the flexural capacity is calculated by using a plastic analysis of the section and by employing rectangular stress block for the concrete.

This is based on the equilibrium of a segment of the slab (figure 1.9). It is necessary a knowledge of the rib resistance per unit length, H_{rib}, and the coefficient of friction μ, coming from slip block tests.

The resultant tensile force T acts on the steel profile is:

$$T = x\, H_{rib}\, b_r + \mu \frac{V_u}{b}$$

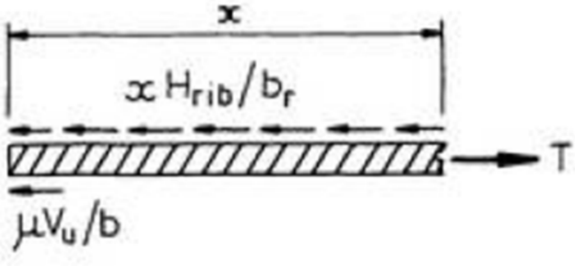

Fig 1.9 Horizontal force equilibrium for steel profile (Stark, Brekelmans, 1990)

The variation of moment capacity, M_{up}, with distance x along the slab can be established as shown in figure 1.10. If the maximum transmitted longitudinal shear force $S_{\max}$ is at least equal to the resulting tensile force T in the sheeting, the slab will fail in a flexural mode. This is defined as a complete shear interaction. It is possible to reach complete shear connection in a middle portion of the element. If the moment due to external loading M^*, increases until the value of M_{up}, the cross-section on this specific position becomes the critical one for flexural collapse. The distance of this section from the nearest support is the length of shear span, if the interaction is not complete.

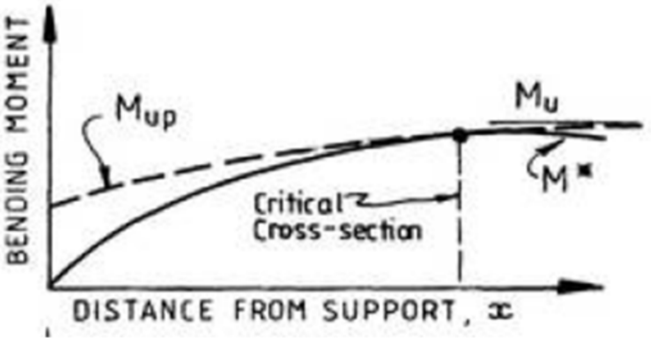

Fig 1.10 Moment-distance from support on partial shear connection strength model (Star , Brekelmans, 1990)

According to Eurocode 4 (EN 1994-1.1, 2004), this method may only be used when the longitudinal shear behaviour has been shown in test to be ductile.

By definition, the longitudinal shear behaviour may be considered to be ductile if the failure load exceeds the load causing a recorded end of slip of 0.1 mm by more than 10%.

1.4 Time-dependent behaviour

Only limited research has been focused on composite slab's serviceability limit state and their long term behaviour.

The work carried out for composite beams was used as a starting point for composite slabs (Roll, 1971; Montgomery, Kulak, Shwartsburd, 1983).

In particular Montgomery at al. (Montgomery, Kulak, Shwartsburd, 1983) predicted theoretically the deflection of a real simply supported beam under dead load.

They computed the creep deflection using an effective Young's modulus for concrete based on the expression of (Bazant, 1972):

$$E_{c,eff} = \frac{E_{c(t0)}}{1 + \chi_{(t,t0)}\varphi_{(t,t0)}}$$

In which $E_{c(t0)}$ is the elastic modulus at the age of first loading, $\varphi_{(t,t0)}$ is the creep coefficient from the age of the loading to the considered age and $\chi_{(t,t0)}$ is the aging coefficient.

In the case of a simply supported beam, shrinkage deflection was evaluated considering the beam bent equally at the edges. Shrinkage deformation was considered uniform through the concrete depth as shown in figure 1.11:

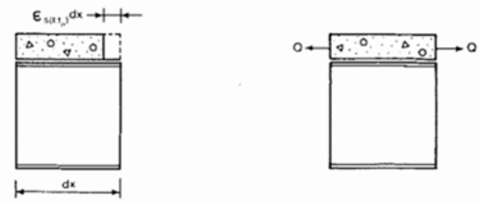

(a) Unrestrained Shrinkage of Concrete Slab

(b) Enforce Compatibility

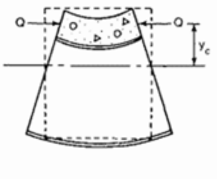

(c) Satisfy Equilibrium

Fig 1.11 Shrinkage deflection theory (Montgomery, Kulak, Shwartsburd, 1983)

Analytical models able to predict the long term behaviour of composite structure were proposed in the late of 80s. They are based on full-shear interaction theory and perfect bond between concrete and metal sheeting (Ghali, Favre, 1986; Gilbert, 1988). Ghali and Favre studied a composite prestressed beam and its time-dependent stress and strain. In the analysis, composite cross section were replaced by transformed section in which steel area were multiplied α times. The coefficient α is the ratio between young modulus of steel and young modulus of concrete. Young modulus of concrete varies considering creep and aging. The gradual development of creep and shrinkage increase the curvature on a generic cross-section of the beam. As a consequence, the beam deflection increases with time.

Gilbert (Gilbert, 1988) proposed to apply the Rate of Creep Method (RCM) to composite structures. The RCM is based on the assumption that the rate of change of creep with time is independent of the age of loading.
A single creep curve could be used for calculating creep strains to any stress history. This could cause an underestimation of creep in old concrete.

These approaches were adopted later to describe composite slabs behaviour, considering uniform shrinkage (UY, 1997; Koukkari, 1999).

Recent studies (Ranzi, Vrcelj, 2009; Bradford, 2010; Al-Deen, 2011; Gilbert, Bradford, Gholamhoseini, Chang, 2011; Ranzi, Leoni, Zandonini, 2012; Al-deen, Ranzi, 2015) have demonstrated the presence of non-uniform shrinkage along a generic cross section. This is due to the presence of the sheeting, which results in a restraint to shrinkage and it prevents moisture's egress from the soffit of composite slab. Experimental tests were performed on slabs in order to quantify non-uniform shrinkage deformations. Generally, a set of specimens were prepared and subdivided in samples free to dry on the bottom faces, samples sealed on the bottom faces by plastic layers and samples with the metal sheeting (figure 1.12). Every single specimen is sealed on the lateral sides in order to eliminate drying in that direction and simulating the continuity of the slab as in a real floor structure.

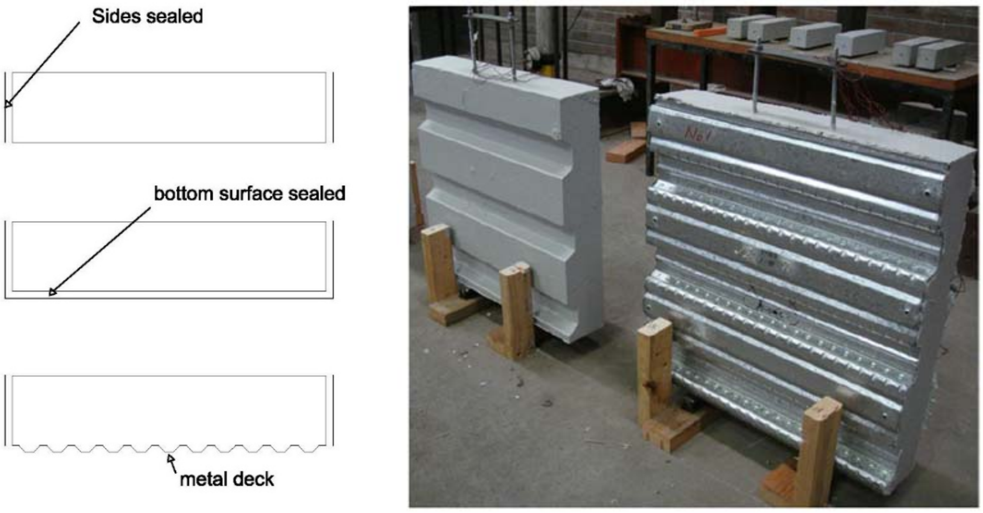

Fig 1.12 Typical shrinkage profile specimens. (Gilbert, Bradford, Gholamhoseini, Chang, 2011)

Long-term deformations are monitored using strain gauges placed on the external surfaces and embedded on the concrete. Sealed and composite samples shows different strain readings through the depth with a higher shortening on the exposed face.

Bottom surface still exhibits non null deformation due to drying shrinkage. This was demonstrated by the presence of significant strain after 1 month of drying, which can't be provided by autogenous shrinkage, because it tends to occur in the first two or three weeks after casting (Gilbert, Bradford, Gholamhoseini, Chang, 2011).

The total strains value on the top surface of the sealed samples could be 20-30% greater than those of samples free to dry on the bottom (Al-deen, Ranzi, 2015). Comparing the strain distribution in sealed and composite slabs, it can be shown the tensile restraining due to the presence of the steel sheeting, which reduces negative strains on bottom and increases them on top.

The thickness of the slab doesn't influence this behaviour, even though deformations due to drying declines with lower value of the ratio of concrete surface to concrete volume.

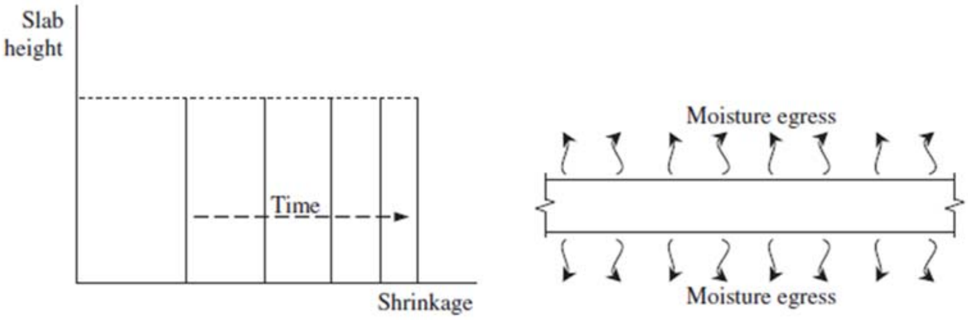

Fig 1.13 Qualitative uniform shrinkage distribution for slab exposed on both sides (Ranzi, Leoni, Zandonini, 2012)

A simplified approach, for taking into account non-uniform shrinkage, was proposed (Al-deen, Ranzi, 2015) . It is based on a linear shrinkage profile, which allows to use uniform shrinkage deformation (figure 1.13) of the reinforced concrete slabs as reference.

The linear assumption (figure 1.14) is the simplest solution for the non-uniform shrinkage description and it is acceptable for design purpose: the uniform shrinkage deformation value, available on codes, is multiplied by coefficients, determined from experimental data, in order to define top and bottom strains of the slab.

Usually the coefficient for the top ranges between 1.1 and 1.2, while the value for the bottom is 0.2-0.3.

In this way the shrinkage profile is defined by a shrinkage strain at the level of the reference axis on the cross section and a shrinkage curvature.

In reality more complex profiles are present through the concrete thickness (Al-deen, Ranzi, 2015), so more refined functions could be used even if they aren't convenient for the design.

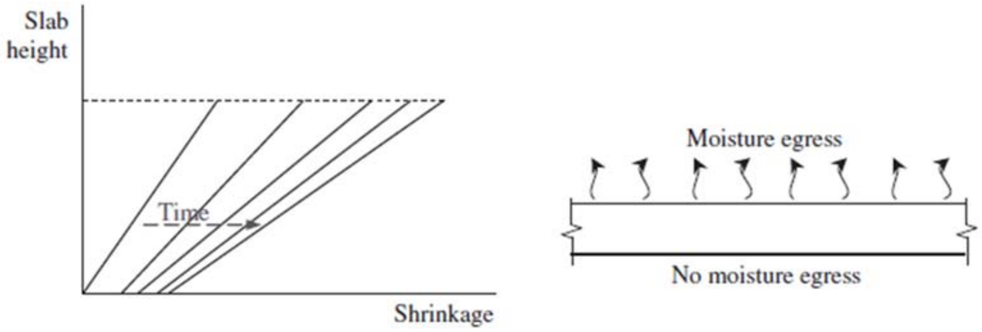

Fig 1.14 Qualitative linear shrinkage distribution for composite slab. (Ranzi, Leoni, Zandonini, 2012)

Analytical formulations in (Bradford, 2010; Ranzi, Vrcelj, 2009) and numerical approach in (Al-deen, Ranzi, 2015; Gilbert, Bradford, Gholamhoseini, Chang, 2011) were proposed only recently in order to take into account the presence of non-uniform shrinkage on the cross-section analysis.

Bradford (Bradford, 2010) proposed a generic model for composite slabs subjected to concrete creep, concrete shrinkage and thermal strains; the method is based on principle of virtual work and a partial shear interaction theory.

Gilbert at al. (Gilbert, Bradford, Gholamhoseini, Chang, 2011) presented a numerical approach extending a long-term formulation described in (Gilbert, Ranzi, 2010) and based on the age-adjusted effective modulus method. Al-Deen and Ranzi (Al-deen, Ranzi, 2015) presented comparisons between calculated deflections using a simplified approach and experimental results available in literature.

2 Materials

2.1 Introduction

This chapter presents the material properties of the components of a composite steel-concrete slab. In the first part of the chapter the time dependent behaviour of concrete is described, followed by the numerical methods that have been used to model it. The model used to take into account non-uniform shrinkage in composite slabs are then described. The material properties and constitutive laws of steel reinforcement and steel sheeting are presented in the last paragraph of the Chapter.

2.2 Concrete

2.2.1 Time Dependent Deformation of concrete

The time-dependent response may be defined as the long-term deformation it undergoes due to delayed strains arising from two phenomena, creep and shrinkage. Concrete creep strain develops over time due to a sustained stress. Conversely, shrinkage strain is completely independent of stress and only depends on the characteristic of particular concrete mix. At service load, this time-dependent inelastic effect may cause issues associated with increased deformation and curvature, and cracking in cases where shrinkage of concrete is restrained. This leads to problems with serviceability and durability of the system. It is possible to assume that the deformation of an uniaxially-loaded concrete specimen is the sum of three different components independent to each other (figure 2.1): the elastic strain $\varepsilon_e(t)$, creep strain $\varepsilon_{cr}(t)$ and shrinkage strain $\varepsilon_{sh}(t)$. The three components could be calculated separately and summed up to obtain the total strain on concrete $\varepsilon_c(t)$ as follows:

$$\varepsilon_c(t) = \varepsilon_e(t) + \varepsilon_{cr}(t) + \varepsilon_{sh}(t) \tag{2.1}$$

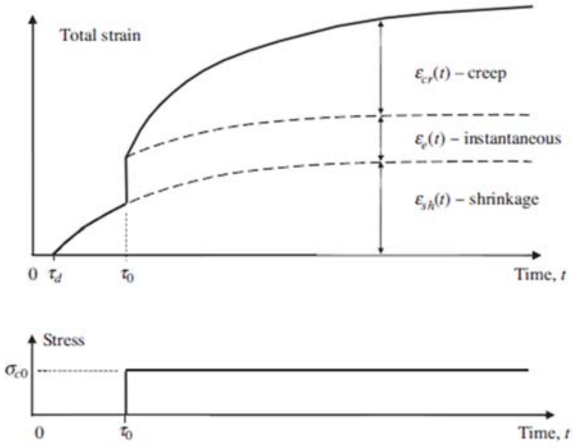

Fig 2.1 Concrete strain components (Gilbert, Ranzi, 2010)

2.2.2 The elastic deformation of concrete

The instantaneous strain occurs immediately after the application of the stress. A suitable constitutive model behaviour is required for the prediction of the instantaneous behaviour of concrete.

When concrete is subjected to compression, it is assumed to remain in its linear-elastic range. If concrete is in tension, the behaviour can be even considered linearly elastic until reaching the tensile capacity. The concrete is expected to crack in tension once it reaches its tensile strength.

For element in flexure, the characteristic flexural tensile strength $f'_{ct,f}$ of concrete has been assumed as a tensile capacity.

The linear-elastic uniaxial model consists of Hooke's Law and can be written as follows:

$$\varepsilon_e(t) = \frac{\sigma_{c0}}{E_c(\tau_0)} \tag{2.2}$$

where τ_0 is the time of loading.

2.2.3 Creep

Creep originates in the hardened cement paste while aggregates provide only restraint to the deformation. The cement paste consists of a rigid cement gel with many capillary, which is made of colloidal sheets formed by calcium silicate hydrates and evaporable water. The mechanism through which creep occurs is causes of controversies among the scientific community and at present there is no satisfactory theory available to describe the formation of creep. Bazant suggested that creep is due to the disorder and instability that characterize the bond between the colloidal sheets. (Bazant, 1972)

Many factors influence the magnitude and the rate of development of creep. These factors are generally categorized in two different groups: the technological parameters and the external parameters. The technological parameters are associated the concrete mix (water/cement ratio, type of aggregates, mechanical properties and type of cement). In general, an increase in either the aggregate content or the maximum aggregate size reduces creep. The same happens with the use of a stiffer aggregate. Creep decreases also with lower water-to-cement ratio. The second group of parameters are the one associated with the ambient conditions, the geometry of the element and the loading conditions. Creep increases as the relative humidity decreases and it is also greater in members with large surface-area-to-volume ratios, such as slabs. It is also dependent on the ambient temperature. Higher temperature increases the deformability of the cement paste and accelerates drying. This accelerates creep. In addition, creep depends on the loading history, e.g. the magnitude and duration of the stress and the age of concrete when the stress is first applied. It shows a marked aging effect: older concrete creeps less than concrete loaded at early ages, even if creep never totally disappears. If the concrete stress is less than about $0.5f_c'$, creep is approximately proportional to the stress and is known as *linear creep.* At higher level of stress creep increases non-linearly with respect to stress. This behaviour is thought to be related to an increase of micro cracking.

In general creep increases over time until the load is maintained, tending to an asymptotic value (which can be equal to 3-4 times the initial elastic deformation). Its rate of increase slows down with time. If the load is removed, it can be observed an instantaneous recovery of the elastic deformation and a gradual reduction of part of creep over time. Creep is significantly greater when accompanied by shrinkage. The additional creep due to drying is known as drying creep. If the specimen is in hygral equilibrium with the environment, the time dependent deformation due to the stress is referred as basic creep.

2.2.4 Shrinkage

Shrinkage may be defined as the change in concrete volume over time. The strain is independent of stress. Shrinkage can be of different types: plastic shrinkage, chemicals shrinkage, thermal shrinkage and drying shrinkage.

The plastic shrinkage is a contraction the concrete volume undergoes when is still in the plastic phase. The plastic shrinkage affects mostly on horizontal surface exposed to the air, which is therefore exposed to the risk of cracking: it tends to contract, but is opposed by the core below that does not shrink; the cortical zone enters then in traction. If the traction exceeds the (very low) tensile strength of the concrete in phase plastic, cracks will appear. At this stage the bond between the plastic concrete and the reinforcement has not yet developed, so the steel can't control cracks. Plastic shrinkage can be avoided while maintaining the jet in an environment saturated with steam, for example through the use of anti-evaporating membranes.

Chemical shrinkage (also called autogenous shrinkage) is a contraction of the concrete volume undergoes after hardening, even when it is maintained at a constant temperature and prevents any possible moisture exchange with the external environment. It is associated to chemical reactions, i.e. the hydration reaction of cement. The effects of autogenous shrinkage are exhausted in the first days after casting and are usually not noticeable in ordinary concrete. Instead, in high performance concrete, which mixture is characterized by a low ratio water / cement, the effects of autogenous shrinkage are well more than appreciable and may even cause the cracking of the elements if prevented by internal or external constraints (Tazawa , Miyazawa , 1992).

In ordinary structures made of concrete with low water/cement ratio, the effects of autogenous shrinkage can be mitigated by careful and prolonged curing of the surfaces to air.

If the concrete is located in an environment with not saturated humidity (RH <95%) tends to dry out and shrink. This effect is known as drying shrinkage, and can affect the hardened concrete of any age, as long as this is exposed to an environment with U.R. less than 95%. It increases in time with decreasing rate.

Thermal shrinkage is the contraction due to the dissipation of heat coming from hydration. It results in the first few hours after casting.

2.3 Numerical methods for time analysis of concrete

2.3.1 The superposition integral

The time dependent behaviour of concrete is described by means of the superposition integral which is defined based on the guideline proposed in (CEB, 1984) as follows:

$$\varepsilon_c(t) = \int_{\tau 0}^{t} \frac{[1+\varphi(t,\tau)]}{E_c(\tau)}\, d\sigma_c(\tau) + \varepsilon_{sh}(t) = \int_{\tau 0}^{t} J(t,\tau)\, d\sigma_c(\tau) \; + \varepsilon_{sh}(t)$$

(2.3)

Where t is the time from casting, τ is the time of loading, τ_0 is the time of first loading, σ_c is the concrete axial stress, $\varphi(t, \tau)$ is the creep coefficient and $J(t, \tau)$ is the creep function. The creep coefficient is defined as the strain at time t caused by a constant unit stress first applied at age τ. It can be expressed as follows:

$$\varphi(t,\tau) = \frac{\varepsilon_{cr}(t,\tau)}{\varepsilon_e(\tau)}$$

(2.4)

Summing the instantaneous and creep strains due to an unitary stress, the creep function $J(t,\tau)$ is obtained as follows:

$$J(t,\tau) = \frac{1}{E_c(\tau)}\, [1+\varphi(t,\tau)]$$

(2.5)

Numerical values of $\varphi(t, \tau)$ and $\varepsilon_{sh}(t)$ are available in standard codes. In this work thesis, the Australian standard code for concrete structures (AS3600, 2009) has been used. The formulation is outlined in Appendix 1.

The superposition integral is based on the principle of superposition. The principle of superposition was applied first to concrete by McHenry (McHenry, 1943). It stated that strain produced by a stress increment applied at any time τ is not affected by any stress applied either earlier or later.

Since the superposition integral cannot be solved in closed form, numerical solutions of the integral are necessary.

2.3.2 The effective modulus method (EMM)

The instantaneous and creep components of strain were combined and an effective modulus for concrete $E_{ef}(t,\tau_0)$ was defined. In the EMM, equation 2.3 is approximated by assuming that the stress-dependent deformations are produced only by a sustained stress equal to the final value of the stress history at time t. The formulation is outlined in the following:

$$\varepsilon_c(t) = \int_{\tau 0}^{t} J(t,\tau)\, d\sigma_c(\tau) \;+ \varepsilon_{sh}(t) \approx \frac{[1+\varphi(t,\tau_0)]}{E_c(\tau_0)}\sigma_c(t) + \varepsilon_{sh}(t)$$
$$= \frac{\sigma_c(t)}{E_{ef}(\tau_0)} + \varepsilon_{sh}(t)$$

(2.6)

Where the effective modulus has been defined as follows:

$$E_{ef}(t,\tau_0) = \frac{E_c(\tau_0)}{[1+\varphi(t,\tau_0)]}$$

(2.7)

Creep is treated as a delayed elastic strain and it is taken into account simply reducing the elastic modulus of concrete with time.

The ageing of the concrete has been ignored.

2.3.3 The age-adjusted effective modulus method (AEMM)

A simple adjustment of the effective modulus method to account the ageing of concrete was proposed by Trost (Trost, 1967). Later the method was more rigorously formulated and further developed by Dilger and Nevile (Dilger, Neville, 1971) and Bazant (Bazant, 1972).

A reduced creep coefficient can be used to calculate creep strain if stress is gradually applied. The reduced creep coefficient is $\chi(t,\tau_0)\varphi(t, \tau)$, where the coefficient $\chi(t,\tau_0)$ is called the ageing coefficient.

Using the AEMM the total strain at time t can be expressed as the sum of the strains produced by $\sigma_c(\tau_0)$ (instanteneous and creep), and the strains produced by a gradually applied stress increment $\Delta\sigma_c(t)$.

The concrete strain at time t can be expressed as follows:

$$\varepsilon_c(t) = \frac{\sigma_c(\tau 0)}{E_{ef}(\tau_0)} + \frac{\Delta\sigma_c(t)}{\bar{E}_{ef}(t,\tau_0)} + \varepsilon_{sh}(t)$$

(2.8)

where $E_{ef}(t,\tau_0)$ is the effective modulus method of equation 2.7 and $\bar{E}_{ef}(t,\tau_0)$ is the age adjusted effective modulus given by:

$$\bar{E}_{ef}(t,\tau_0) = \frac{E_c(\tau_0)}{[1 + \chi(t,\tau_0)\ \varphi(t,\tau_0)]}$$

(2.9)

With the AEMM, two analyses need to be carried out: one at first loading (time τ_0) and one at time t.

2.3.4 The Step-by-step method (SSM)

Considering the stress history in figure 2.2, the time under load could be divided into n steps. The continuously time-stress curve could be approximated by a series of small stress increments.

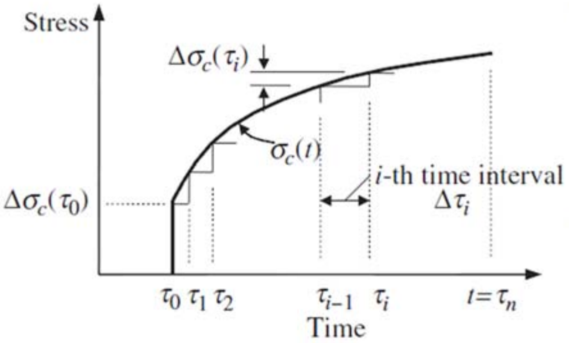
Stress
$\Delta\sigma_c(\tau_i)$
$\sigma_c(t)$
i-th time interval
$\Delta\tau_i$
$\Delta\sigma_c(\tau_0)$
τ_0 τ_1 τ_2
τ_{i-1} τ_i
$t=\tau_n$
Time

Fig 2.2 Time-stress history (Gilbert, Ranzi, 2010)

The actual stress history is approximated by a step-wise variation of stress. In this simplification, the period of sustained stress is divided into k time intervals with the age at first loading designated τ_0 and the end of the period of sustained stress designated τ_k(figure 2.3).

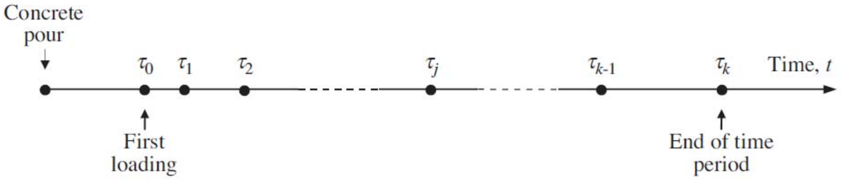
Concrete pour
τ_0 τ_1 τ_2
τ_j
$\tau_{k\text{-}1}$
τ_k
Time, t
First loading
End of time period

Fig 2.3 Time discretization (Gilbert, Ranzi, 2010)

The time discretization used in this thesis work, based on a geometrical progression, is the following:

$$\tau_j = \tau_0 + (\tau_k k)^{1/(k-1)}\,(\tau_{j-1} - \tau_0)$$

$$\tau_1 = \tau_0 + \frac{(\tau_k - \tau_0)}{\tau_k k}$$

(2.10)

where $(\tau_k - \tau_0)$ is the period in which sustained stress is present, k is the total number of time intervals and j is the time interval considered.

The total concrete strain at the end of the $j-th$ time period may be approximated by:

$$\varepsilon(t_j) = J(t_j, \tau_0)\sigma_c(\tau_0) + \sum_{i=1}^{j} J(\tau_j, \tau_i)\Delta\sigma_c(\tau_i) + \varepsilon_{sh}(\tau_j)$$

(2.11)

where:

$J(t_j, \tau_i)$ is the creep (compliance) function calculated at time t_j related to a unit stress applied at time t_i.

$\Delta\sigma_c(\tau_i)$ is calculated as $\sigma_c(\tau_i) - \sigma_c(\tau_{i-1})$ and represents the stress variation that occurs between times τ_{i-1} and τ_i. The simplification introduced by the step-by-step method is that the stress is assumed to remain constant during each time interval and so for a more accurate prediction is needed a big number of time intervals. The bigger this number, the higher is the computational difficulty.

The time discretization should be such that an approximately equal portion of the creep coefficient $\varphi(t, \tau_i)$ develops during each time step (Gilbert, Ranzi, 2010).

In this thesis, the equation approximates the integral-type creep law by means of the so-called rectangular rule.

Simplifying the notation, the equation (2.11) becomes:

$$\varepsilon_j = J_{j,0}\sigma_{c,0} + \sum_{i=1}^{j} J_{j,I}\Delta\sigma_{c,i} + \varepsilon_{sh,j}$$

(2.12)

Rearranging the equation (2.12):

$$\varepsilon_j - \varepsilon_{sh,j} = J_{j,0}\sigma_{c,0} + \sum_{i=1}^{j} J_{j,i}\Delta\sigma_{c,i}$$

$$= J_{j,0}\sigma_{c,0} + J_{j,j}\left(\sigma_{c,j} - \sigma_{c,j-1}\right) + \sum_{i=1}^{j-1} J_{j,i}\left(\sigma_{c,i} - \sigma_{c,i-1}\right)$$

$$= J_{j,0}\sigma_{c,0} + J_{j,j}\sigma_{c,j} - J_{j,j}\sigma_{c,j-1} + \sum_{i=1}^{j-1} J_{j,i}\sigma_{c,i} - \sum_{i=1}^{j-1} J_{j,i}\sigma_{c,i-1}$$

$$= J_{j,0}\sigma_{c,0} + J_{j,j}\sigma_{c,j} - J_{j,j}\sigma_{c,j-1} + \sum_{i=1}^{j-1} J_{j,i}\sigma_{c,i} - \sum_{i=0}^{j-2} J_{j,i+1}\sigma_{c,i}$$

$$= J_{j,0}\sigma_{c,0} + J_{j,j}\sigma_{c,j} - J_{j,j}\sigma_{c,j-1} + J_{j,j-1}\sigma_{c,j} + \sum_{i=1}^{j-2} (J_{j,i} - J_{j,i+1})\sigma_{c,i} - J_{j,1}\sigma_{c,0}$$

$$= (J_{j,0} - J_{j,1})\sigma_{c,0} + J_{j,j}\sigma_{c,j} + \sum_{i=1}^{j-1} (J_{j,i} - J_{j,i+1})\sigma_{c,i}$$

$$= J_{j,j}\sigma_{c,j} + \sum_{i=0}^{j-1} (J_{j,i} - J_{j,i+1})\sigma_{c,i}$$

(2.13a-g)

The equation (2.13g) can be arranged in terms of stress and the constitutive relationship for the concrete becomes:

$$\sigma_{c,j} = \frac{\varepsilon_j - \varepsilon_{sh,j}}{J_{j,j}} - \sum_{i=0}^{j-1} \frac{J_{j,i} - J_{j,i+1}}{J_{j,j}}\sigma_{c,i} = E_{c,j}(\varepsilon_j - \varepsilon_{sh,j}) - \sum_{i=0}^{j-1} F_{e,j,i}\sigma_{c,i}$$

(2.14)

Where $E_{c,j}$ is the elastic modulus of concrete at τ_j:

$$E_{c,j} = \frac{1}{J_{j,j}}$$

(2.15)

And $F_{e,j,i}$is the stress modification factor:

$$F_{e,j,i} = \frac{J_{j,i} - J_{j,i+1}}{J_{j,j}}$$

(2.16)

For each time step, $E_{c,j}$ and $F_{e,j,i}$ must be specified and the previous stress history must be stored throughout the analysis.

However, the SSM is not subject to many of the simplifying assumptions contained in other methods of analysis and generally leads to reliable results. For most practical problems, satisfactory results are obtained using as few as 6–10 time intervals (Gilbert, Ranzi, 2010).

2.4 The non-uniform shrinkage on composite slab cross-section

If drying occurs at different rate from the top and bottom surfaces, the total strain distribution is no longer uniform over the depth of the section.

As previously discussed, recent studies (Ranzi, Vrcelj, 2009; Bradford, 2010; Al-Deen, 2011; Gilbert, Bradford, Gholamhoseini, Chang, 2011; Ranzi, Leoni, Zandonini, 2012; Al-deen, Ranzi, 2015b) have demonstrated the occurrence of non-uniform shrinkage on composite slab cross-section (as shown in figure 2.4 and figure 2.5).

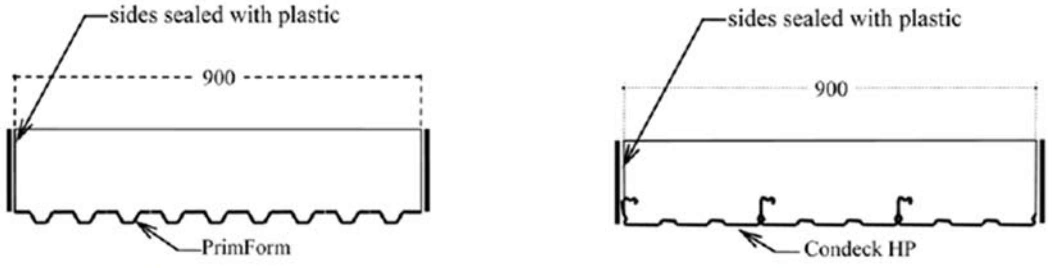

(c) Sample type PF

(d) Sample type CK

Fig 2.4 Composite samples for shrinkage measurement (Al-Deen, Ranzi, 2015b)

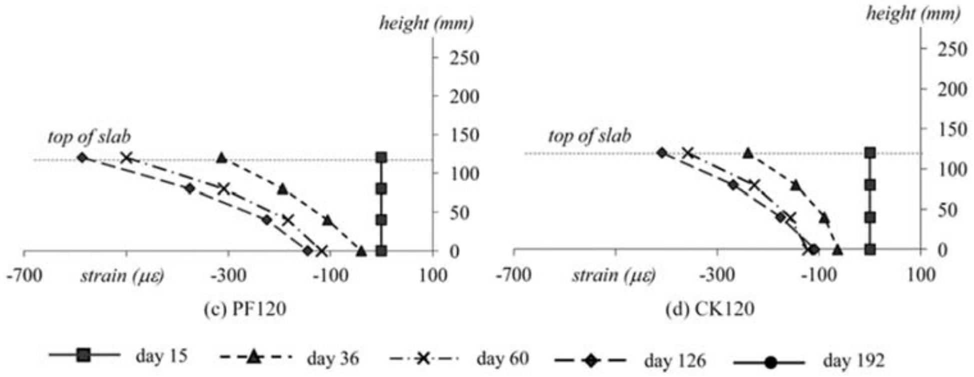

(c) PF120

(d) CK120

Fig 2.5 Total long-term measured at different instances in time through the cross-section

In current design guidelines, the non-uniform free shrinkage distribution is not present. The simplest possible profile to model non-uniform shrinkage is a linear distribution, even though more complex shrinkage profiles occur through the thickness. For this purpose Al-Deen and Ranzi (Al-deen, Ranzi, 2015b) proposed a linear shrinkage distribution based on the free shrinkage for conventional concrete slabs. This distribution is available from codes or measured experimentally.

The non-uniform free shrinkage profile for composite slabs can be described by the top and bottom strain:

$$\varepsilon_{t,sh,k} = \eta_{t,k}\,\varepsilon_{sh,k}$$
$$\varepsilon_{b,sh,k} = \eta_{b,k}\,\varepsilon_{sh,k}$$

(2.17)

where subscript indices k refers to the time instant in which strains are computed. $\varepsilon_{sh,k}$ is the free shrinkage distribution of a slab exposed on both sides.

The coefficients $\eta_{t,k}$ and $\eta_{b,k}$ are determined experimentally in the study (Al-deen, Ranzi, 2015b). For routine design it has been recommended to set this coefficient as follows:

$$\eta_{t,k} = 1.2$$
$$\eta_{b,k} = 0.2$$

(2.18)

The shrinkage profile could be also express by the shrinkage strain measured at the level of the cross-section reference axis, $\varepsilon_{r,sh,k}$ and an additional curvature $\kappa_{r,sh,k}$.

$$\varepsilon_{r,sh,k} = \frac{(h - h_r)\eta_{t,k} + h_r\eta_{b,k}}{h}\varepsilon_{sh,k}$$
$$\kappa_{r,sh,k} = \frac{\eta_{t,k} - \eta_{b,k}}{h}\varepsilon_{sh,k}$$

(2.19)

In which h_r is the position of the reference axis with respect of top (figure 2.6).

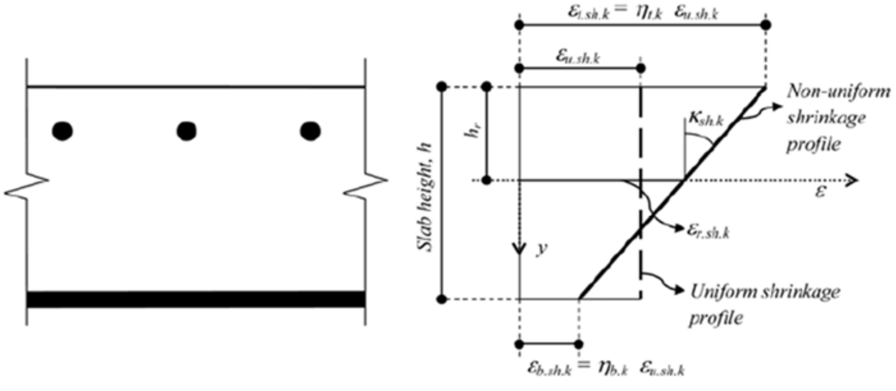
ε_t.sh.k = η_t.k ε_u.sh.k
ε_u.sh.k
Non-uniform shrinkage profile
κ_sh.k
h_r
Slab height, h
ε
ε_r.sh.k
y
Uniform shrinkage profile
ε_b.sh.k = η_b.k ε_u.sh.k

(a) Typical composite slab cross-section

(b) Shrinkage profile

Fig 2.6 Strain variables describing non-uniform free shrinkage on composite slabs

2.4.1 Comparison with experimental results

A sectional analysis using the linear shrinkage profile, above introduced, has been used for the calculation of a slab deflection in (Al-deen, Ranzi, 2015b), where the behavior of concrete was modeled using the age-adjusted effective modulus method. The results were compared with the experimental results of samples described in (Al-deen, Ranzi, Uy, 2015; Ranzi, Al-Deen, Ambrogi, Uy, 2013). It turned out that, when the linear shrinkage profile is assumed, the calculation predicted the long-term deflections of the slabs with acceptable accuracy. The study highlighted also that the use of uniform shrinkage profiles leads to underestimation of the deflections.

Another validation has been done using experimental results achieved at the Laboratory of the School of Civil and Environmental Engineering - The University of New South Wales (Gholamhoseini, 2014). The experimental program involved the testing of ten simple-span composite slabs under different sustained, uniformly distributed load for periods up to 240 days. In particular, the validation considered four out of ten slabs, which are identified by the codes 1LT-70-0, 2LT-70-3, 3LT-70-3 and 4LT-70-6. The four slabs have the same metal sheeting profile.

The centre to centre distance between the two end supports was 3100 mm. The slabs were subjected to different levels of sustained loading, which has been applied at age 64 days.

Slab 1LT-70-0 carried only the self-weight for the full test duration, slabs 2LT-70-3 and 3LT-70-3 were identical and carried a constant superimposed sustained load of 3.4 kPa and slab 4LT-70-6 carried a sustained load of 6 kPa.

The results of the comparisons between experimental long-term deflection and the computed long-term deflection are outlined in table 2-1.

	247 days		
SLAB	TEST	LINEAR SHRINKAGE	
		CALCULATED	RATIO
1LT-70-0	4.04	3.76	0.93
2LT-70-3	6.72	6.22	1.08
3LT-70-4	5.84	6.22	0.94
4LT-70-6	6.4	8.50	0.75

Note: deflection in mm

Table 2-1 Validation of the linear shrinkage

The results highlight the linear shrinkage profile assumption well represents the long term behaviour of composite slab. It is worth to notice the computation of deflections has been performed by means of a cross-sectional analysis, which is a relatively simple approach suitable for practical applications.

2.5 Steel

2.5.1 Conventional, non-prestressed reinforcement

With regard to serviceability, steel reinforcement can be useful to reduce both immediate and time-dependent deformations. Adequate quantities of bonded, non-prestressed steel also provide crack control.

In Australia, reinforcing bars are two types, Grade R250N and Grade D500N (250 and 500 refers to the characteristic yield stresses f_y of 250 MPa and 500 MPa, respectively). Grade R250N bars are hot-rolled plain round bars of 6 or 10 mm diameter (designated R6 and R10 bars) and are commonly used for fitments such as ties and stirrups. Grade D500N bars are hot-rolled deformed bars with sizes ranging from 12 to 40 mm diameter (in 4 mm increments).

In design calculations, the constitutive law of steel is usually considered to be elastic-perfectly plastic. In the elastic range, steel stress σ_s is proportional to the steel strain ε_s :

$$\sigma_s = E_s \varepsilon_s$$

Where E_s is the elastic modulus of the steel. After yielding the stress–strain curve was assumed to be horizontal (perfectly plastic), ignoring the hardening. The stress-strain curve in compression is equal to that in tension. At service loads, the stress in the non-prestressed steel is usually less than the yield stress and behaviour is linear-elastic.

2.5.2 Metal Sheeting

In many cases, the deflection under fresh concrete is the parameter governing the sheet selection. The steel sheeting has to support not only concrete weight during hardening, but also the heaping of concrete and the pumping loads.

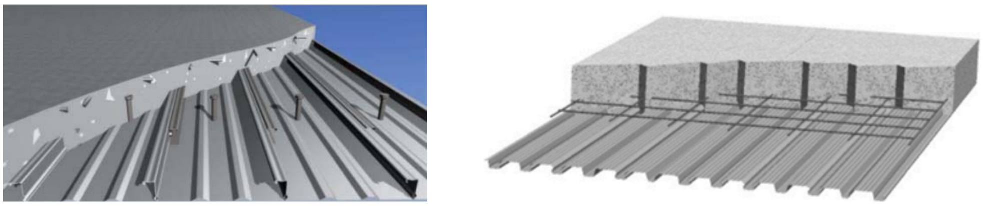

Fig 2.7 The metal sheeting

The sheeting thickness ranges between 0.6 mm and 1.2 mm. It is very thin for economic reasons. Typically, they are 1 m wide and up to 6 m long and they are designed to span only in one direction. The sheets are usually pressed or cold-formed and are galvanized to resist corrosion,

The nominal yield strength is that of the flat sheet from which the element is made. Now, products are available with a yielding stress equal to $f_y = 550$ MPa. The elastic modulus is $E_s = 200000$ MPa.

The considered constitutive law is assumed elastic-perfectly plastic as ordinary reinforcement steel (figure 2.8).

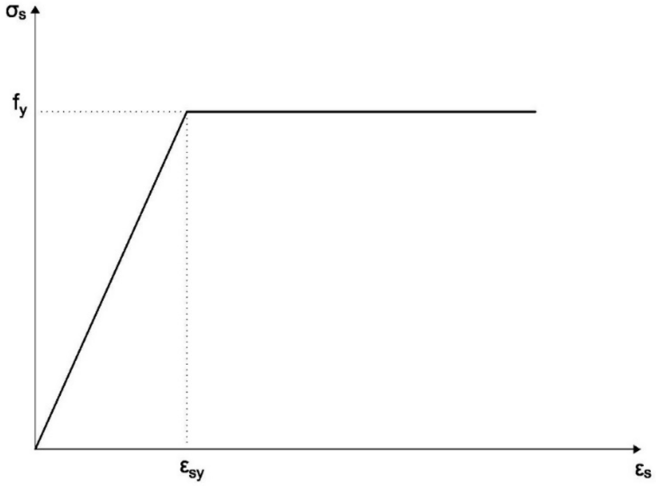

Fig 2.8 Elastic-plastic constitutive law of steel

In this thesis, two different profiles have been considered, which are referred to as profile 1 and profile 2 (figure 2.9). The geometric properties are summarized in table 2-2.

Profile [.]	t_{ms} [mm]	A_{ms} [mm^2/m]	y_{ms} [mm]	I_{ms} [mm^4/m]	Mass [kg/m^2]
1	1	1678	15.50	445050	13.79
2	1	1620	15.40	647000	13.31

Table 2-2 Geometric properties of the profiled steel sheeting

Where t_{ms} is the thickness of the profile. A_{ms} is the area per unit width of the profile, y_{ms} is the centroid of the metal sheeting with respect to the bottom flange, I_{ms} is the inertia per unit width.

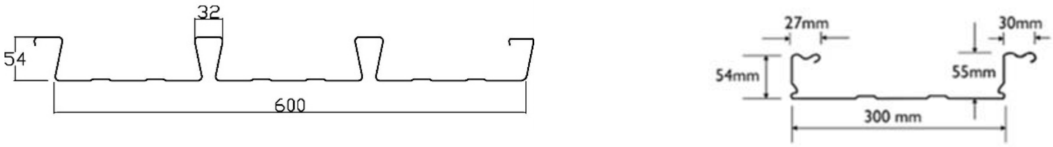

(a) Profile 1 (b) Profile 2

Fig 2.9 Geometry of the profiled steel sheeting

3 Design of composite slab

3.1 Introduction

This chapter describes the ultimate and service limit state design of simply-supported composite steel-concrete slabs based on the Australian design rules as reference. In particular, the proposed formulation is based on the new Australian draft code for composite steel-composite structures (AS2327 Draft, 2015). The ultimate limit state design rules specified in this code are similar to those recommended in the European guidelines (EN 1994-1.1, 2004) and are presented in the first part of the chapter, followed by the description of the serviceability requirements. The Australian approach differs from current international guidelines for the attention placed at considering a concrete shrinkage gradient, which develops dues to the inability of the concrete to dry from its underside, for the serviceability limit state requirements. In particular, this non-uniform shrinkage profile has been accounted for with a linear distribution as presented in chapter 2. Other international guidelines enable, within specified range of span to-depth-ratio, to omit deflection calculations and, when not satisfying these requirements, permit to carry out the service slab design without considering the occurrence of shrinkage. When shrinkage effects are considered, the design is based on a uniform shrinkage profile.

In the second part of the chapter, an extensive parametric study is carried out considering the design of composite slabs carried out based on the three serviceability models, i.e. the first model accounting for the shrinkage gradient, the second approach relying on a constant (uniform) shrinkage profile and the third procedure ignoring shrinkage effects. The numerical calculations and design have been implemented in a Matlab program. The main aims of the parametric study are to evaluate the differences produced by the three serviceability procedures on the composite slabs' design for different loading conditions, cross-sectional properties and floor arrangements.

3.2 Limit state requirements specified by Australian draft code AS2327

3.2.1 Ultimate limit state: Flexure

The draft code states that the bending resistance M_{Rd} shall be determined by plastic theory based on full or partial shear connection and that the partial shear connection method can be used for slabs with a ductile longitudinal shear behaviour.

The design bending moment shall not exceed the design resistance M_{Rd} which is:

$$M_{Rd} = N_{p,d} z + M_{pr,d} \tag{3.1}$$

where:

$N_{p,d}$ = design axial force resisted by the profiled sheeting

$M_{pr,d}$ = plastic resistance moment of the profiled steel sheeting reduced by the axial force $N_{p,d}$. Its value can be taken equal to:

$$1.25 M_{pa,d} \left(1 - \frac{N_{p,d}}{N_{yp,d}}\right) \leq M_{pa,d}$$

$M_{pa,d}$ = design plastic resistance in bending of the profiled sheeting

$= \phi\, M_{pa}$

ϕ = capacity reduction factor

M_{pa} = nominal plastic resistance in bending of profiled sheeting

z = composite level arm calculated with equation (3.2)

The design axial load force resisted by the profiled sheeting $N_{p,d}$ at a particular cross-section is:

$N_{p,d}$ = $\min(N_{\tau,d}\, , N_{FSC,d})$

where:

$N_{FSC,d}$ is the design axial force resisted by the profiled sheeting in full shear connection expressed as follows:

$$N_{FSC,d} = \min(N_{yp,d}, N_{c,d})$$

in which:

$N_{yp,d}$ = design axial force resisted by the profiled sheeting at yield

$= f_{yp,d} A_{pe}$

$f_{yp,d} = \phi\, f_{yp}$

$N_{c,d} = f_{cd}\, h_c\, b$

$f_{cd} = \phi_c\, f_c'$

ϕ_c = capacity reduction factor

and

$N_{\tau,d}$ = design axial force resisted by the shear connection between the profiled sheeting and the concrete slab relying on the mechanical or frictional interlock

$= \tau_{u,Rd}\, b\, L_x$

$\tau_{u,Rd}$ = design shear strength obtained from slab test meeting the basic requirements of the partial connection method.

L_x = distance of the cross-section being considered to the nearest support for a simply supported slab

At a particular cross-section, the design is classified as based on full or partial shear connection depending on the magnitude of the axial force resisted by the profiled sheeting:

full shear connection if $N_{p,d} = N_{FSC,d}$

partial shear connection if $N_{p,d} < N_{FSC,d}$

For simplification, the distance z shall be determined based on:

$$z = h - 0.5\, h_1 - e_p + (e_p - e)\frac{N_{p,d}}{N_{yp,d}} \tag{3.2}$$

where:

$h_1 = x_{pl}$ when the section is designed in partial shear connection or when the section is designed in full shear connection with $x_{pl} < h_c$ (i.e. if the neutral axis is above the steel sheeting as shown in figure 3.1); or

$= h_c$ when the section is designed in full shear connection and $x_{pl} > h_c$ (i.e. if the neutral axis is in the steel sheeting as shown in figure 3.2).

x_{pl} = location of the plastic neutral axis from the extreme compressive fibre of the composite slab

$= N_{p,d}/(0.85\, f_{cd}\ b)$

e = distance from the centroidal axis of the profiled sheeting to the extreme fibre of the composite slab in tension

e_p = distance from the plastic neutral axis of the profiled sheeting to the extreme fibre of the composite slab in tension

Figures 3.1 and 3.2 show the stress distribution on the cross-section if the neutral axis is above and below the steel sheeting respectively:

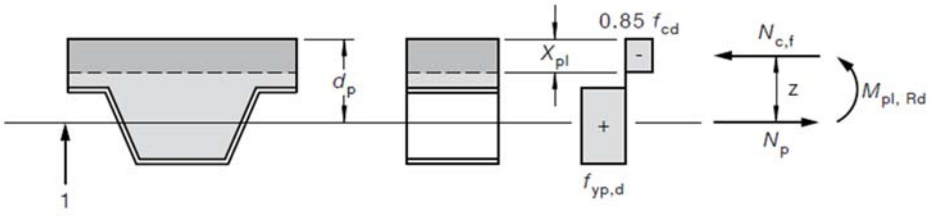

Fig 3.1 Stress distribution for sagging bending if the neutral axis is above the steel sheeting (Draft AS2327)

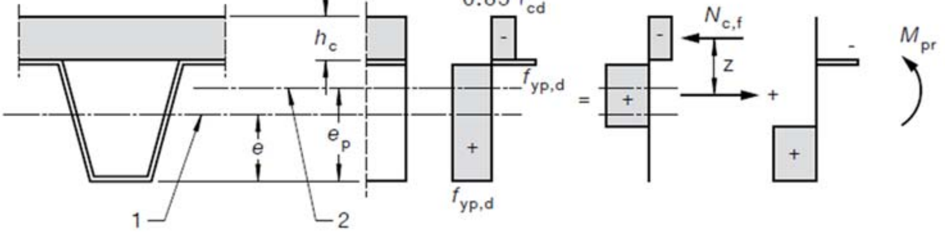

Fig 3.2 Stress distribution for sagging bending if the neutral axis is in the steel sheeting (Draft AS2327)

3.2.2 Ultimate limit state: Vertical shear

A composite steel concrete slab can be considered as a beam without shear reinforcement. The vertical shear resistance V_{rd} can be determined in accordance with the Australian standard code for concrete structures (AS3600, 2009)as follows:

$$V_{rd} = \beta b_v d_0 f_{cv} \left(\frac{A_{st}}{b_v d_0}\right)^{1/3}$$

where:

$f_{cv} = (f_c')^{1/3} \leq 4\ Mpa$

$\beta = \beta_1 \beta_2 \beta_3$

$\beta_1 = 1.1(1.6 - d_0/1000) \geq 0.8$

$\beta_2 = 1$ (if no axial action is considered)

$\beta_3 = 1$ (if only gravity loadings are presented)

d_0 = the distance from the extreme compression fibre of the concrete to the centroid of the outermost layer of tensile reinforcement

A_{st} = the area of the longitudinal steel provided in the tensile zone (the metal sheet for composite slab)

b_v = minimum effective web width in mm (the width for composite slab)

3.2.3 Serviceability limit state: deflection

The calculated defection should not exceed the deflection limits that are appropriate to the structure and its intended use. The deflection limits are expressed in terms of deflection-to-span ratio and are applied to both total deflection and incremental deflection.

The total deflection δ_{tot} is the final long-term deflection of the slab that is calculated as the sum of the short-term and time-dependent deflection caused by the dead load (including self-weight), the expected in service live load and the effects of shrinkage.

The limit on the incremental deflection is imposed to avoid damages on brittle partitions or floor finishes.

The incremental deflection δ_{incr} is a portion of the total deflection that occurs after the attachment or installation of the non-structural elements that can be damaged. Total deflection and incremental deflection can be expressed as follows:

$$\delta_{tot} = \delta_{inst} + \delta_{cc} + \delta_{cs}$$
$$\delta_{incr} = \delta_{inst,incr} + \delta_{cc,incr} + \delta_{cs,incr}$$

(3.3 a,b)

where:

δ_{inst} = instantaneous deflection

δ_{cc} = creep deflection

δ_{cs} = shrinkage deflection

and the subscript *incr* refers to the incremental deflection.

The loads resisted by the composite floor system for the purpose of the deflection calculations vary depend on the adopted construction procedure. In the case of unpropped construction, the self-weight of the wet concrete is carried by the steel sheeting which acts as permanent formwork, while all loads applied after the removal of the props are resisted by the composite action. In the case of propped construction, the composite member resists all applied loads, including its self-weight.

The total and incremental deflections are usually calculated and measured from the top of the concrete slab, unless particular aesthetics requirements are specified for the underside of the floor.

The service load combinations adopted for propped and unpropped construction are summarized in tables 3-1 and tables 3-2, respectively. The static configuration of the slab is shown in figure 3.3.

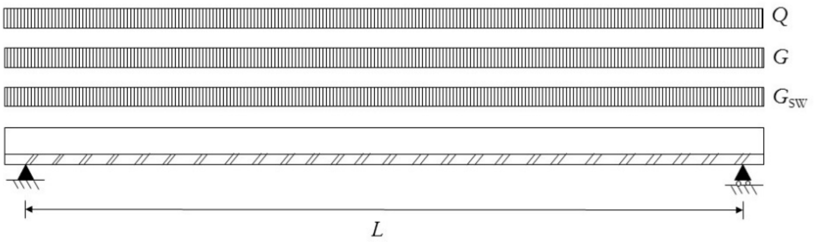

Fig 3.3 Static configuration of the composite slab

Propped construction

Total deflection

Load for	δ_{inst}	Gsw + G + 0.7 Q
Load for	δ_{cc}	creep due to Gsw
		+ creep due to G
		+ creep due to 0.4 Q
Load for	δ_{cs}	shrinkage

(a) total deflection

Propped construction

Incremental deflection

Load for	δ_{inst}	0.7 Q
Load for	δ_{cc}	creep due to Gsw
		+ creep due to G
		+ creep due to 0.4 Q
Load for	δ_{cs}	shrinkage

(b) incremental deflection

Table 3-1 Load combinations for the evaluation of deflections in propped construction

Unpropped construction

Total deflection

Load for	δ_{inst}	G + 0.7 Q
Load for	δ_{cc}	creep due to G
		+ creep due to 0.4 Q
Load for	δ_{cs}	shrinkage

(a) total deflection

Unpropped construction

Incremental deflection

Load for	δ_{inst}	0.7 Q
Load for	δ_{cc}	creep due to G
		+ creep due to 0.4 Q
Load for	δ_{cs}	shrinkage

(b) incremental deflection

Table 3-2 Load combinations for the evaluation of deflections in unpropped construction

3.2.4 Slab deflection by simplified calculation

The simplified approach for the deflection calculations can be used when the effects of end slip are negligible, i.e. the slip can be neglected when the initial slip load in the composite slab standard test (based on a four points loading arrangement) exceeds 1.2 times the design service load.

3.2.4.1 Short term deflection

The deflection of a simply supported slab due to a distributed load (*q*) can be computed under the hypothesis of linear elastic material as:

$$\delta_{inst} = \frac{5}{384}\frac{q_{inst}L^4}{E_c I_{ef}} \tag{3.4}$$

in which:

q_{inst} = short term loading as defined in tables 3-1 and 3-2

E_c = mean value of the modulus of elasticity of the concrete determined at the time of loading. It is determined in accordance with (AS3600, 2009)

I_{ef} = second moment of area of the cross-section with the steel reinforcement and steel sheeting transformed to an equivalent area of concrete. It is referred to the centroid of the section.

The effective second moment of area (I_{ef}) is an empirical adjustment of the second moment of area of a cracked member to account for tension stiffening. For a simply supported slab, the value is computed at mid-span and is calculated by the Branson's formula:

$$I_{ef} = I_{cr} + (I_{uncr} - I_{cr})\left(\frac{M_{cr}}{M_s^*}\right)^3 \leq I_{ef,max} \tag{3.5}$$

where:

$I_{ef,max}$ = maximum effective second moment of area, equal to I_{uncr}

I_{cr} = second moment of area of the cracked slab section, ignoring the contribution of concrete in tension. The steel reinforcement and steel sheeting are transformed into an equivalent area of concrete.

I_{uncr} = second moment of area of the uncracked slab section with the steel reinforcement and steel sheeting transformed into an equivalent area of concrete

M_s^* = maximum in-service moment resisted by the cross-section

M_{cr} = $Z\ (f'_{ct,f} - \sigma_{cs})$ bending moment when cracking occurs

(3.6)

$f'_{ct,f}$ = characteristic flexural tensile strength

Z = section modulus of the uncracked cross-section, referred to the extreme fibre at which cracking occurs

σ_{cs} = maximum shrinkage-induced tensile stress on the uncracked section at the extreme fibre at which cracking occurs

The value of σ_{cs} can be obtained from sectional analysis using an arbitrary reference axis on the cross-section as follows:

$$\sigma_{cs} = \frac{E_{ef.sc}}{R_{I.sh}R_{A.sh} - R_{B.sh}^2}\left[\left(R_{I.sh} - yR_{B.sh}\right)f_{sh1} + \left(R_{B.sh} - yR_{I.sh}\right)f_{sh2}\right] - E_{ef.sc}\left(\varepsilon_{r.sh} - y\kappa_{sh}\right)$$

(3.7)

where:

$E_{ef,sc}$ = $\frac{E_c}{1+0.55\ \varphi_{cc}}$ is the concrete elastic modulus for shrinkage analysis calculated at the time of interest t for a load applied at time t_0

φ_{cc} = creep coefficient for concrete computed at time t for a load applied at time t_0

$R_{A.sh}$ = axial rigidity of the cross-section computed with $E_{ef,sc}$ as elastic modulus

$R_{B.sh}$ = rigidity related to the first moment of area of the cross-section computed with $E_{ef,sc}$ as elastic modulus

$R_{I.sh}$ = flexural rigidity of the cross-section computed with $E_{ef,sc}$ as elastic modulus

The terms f_{sh1} and f_{sh2} are the equivalent loads for shrinkage and shall be computed as follows:

$$\begin{bmatrix} f_{sh1} \\ f_{sh2} \end{bmatrix} = E_{ef.sc} \begin{bmatrix} A_c & -B_c \\ -B_c & I_c \end{bmatrix} \begin{bmatrix} \varepsilon_{r.sh} \\ \kappa_{sh} \end{bmatrix} = E_{ef.sc} \begin{bmatrix} A_c \varepsilon_{r.sh} - B_c \kappa_{sh} \\ -B_c \varepsilon_{r.sh} + I_c \kappa_{sh} \end{bmatrix} \tag{3.8}$$

In which A_c, B_c and I_c are the geometric properties of the concrete part of the cross-section.

The terms $\varepsilon_{r,sh}$ and κ_{sh} are the generalized free shrinkage strains on the cross-section with respect to the reference axis.

It is possible to rearrange equation (3.6) for M_{cr} as follows:

$$M_{cr} = \frac{R_I R_A - R_B{}^2}{E_c \left(R_B - y R_A \right)} \left(f'_{ct,f} - \sigma_{cs} \right) \tag{3.9}$$

in which R_A, R_B and R_I are the uncracked cross-sectional rigidities.

The flexural rigidities referred to the centroid of the uncracked and cracked cross-section can be computed using the rigidities related to the reference axis, as follows:

$$E_c I_{uncr} = \frac{R_I R_A - R_B^2}{R_A} \tag{3.10}$$

$$E_c I_{cr} = \frac{R_{I.cr} R_{A.cr} - R_{B.cr}^2}{R_{A.cr}} \tag{3.11}$$

The calculation of the cracked rigidities is carried out by determining the position of the neutral axis on the cracked cross-section. The procedure for the evaluation of its location does not consider tension resistance for concrete and can be resumed as follows:

$$\alpha_r = \frac{A_{deck}}{bd_{deck}} \frac{E_s}{E_c}$$

$$k = \sqrt{\alpha_r^2 + 2\alpha_r} - \alpha_r$$

$$d_{cr} = kd_{deck}$$

(3.12 a,b,c)

The term d_{cr} and d_{deck} are the position of the neutral axis and the deck with respect to the top of the slab, as shown in figure 3.4.

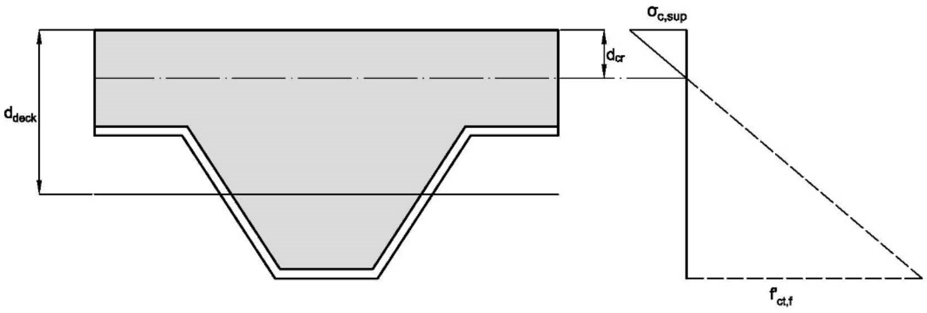

Fig 3.4 Stress distribution for the computation of cracked cross-section's properties

3.2.4.2 Creep deflection

The deflection component due to creep δ_{cc} is determined by multiplying the short-term deflection produced by sustained load by the creep multiplier as follows:

$$\delta_{cc} = \delta_{inst.sust} \alpha_{cc}$$

(3.13)

where:

$\delta_{inst.sust}$ = instantaneous deflection of the sustained load

$\alpha_{cc} = \frac{E_c I_{ef}}{E_{ef.cc} I_{ef.cc}} - 1$ creep multiplier

$E_{ef,cc} = \frac{E_c}{1+\varphi_{cc}}$ is the effective modulus of the concrete

$I_{ef,cc}$ = is the effective second moment of area expressed in terms of the concrete and calculated with the effective modulus $E_{ef,cc}$

When evaluating $I_{ef,cc}$, the second moment of area associated with the cracked cross-section can be determined based on the cracked geometry identified in equations 3.12.

3.2.4.3 Shrinkage deflection

The effects of shrinkage on the deflection can be taken into account as an induced curvature (κ_{sh}) applied on the slab as follows:

$$\delta_{cs} = \frac{\bar{\kappa}_{sh} L^2}{8} \tag{3.14}$$

in which the induced curvature (κ_{sh}) is:

$$\bar{\kappa}_{sh} = \left[1-\left(\frac{M_{cr}}{M_s^*}\right)^2\right]\bar{\kappa}_{sh,cr} + \left[\left(\frac{M_{cr}}{M_s^*}\right)^2\right]\bar{\kappa}_{sh,uncr} \tag{3.15}$$

where:

$\bar{\kappa}_{sh,uncr}$ = curvature produced by shrinkage over an uncracked section based on a long term analysis and considering the effective modulus of elasticity $E_{ef,sc}$

$\bar{\kappa}_{sh,cr}$ = curvature produced by shrinkage over a cracked section based on a long term analysis and considering the effective modulus of elasticity $E_{ef,sc}$

The curvatures $\bar{\kappa}_{sh,uncr}$ and $\bar{\kappa}_{sh,cr}$ can be expressed both as follows:

$$\bar{\kappa}_{sh,i} = \frac{E_{ef.sc}}{\mathrm{R}_{\mathrm{I,i}}\mathrm{R}_{\mathrm{A,i}} - \mathrm{R}_{\mathrm{B,i}}}[R_{B,i}(A_{c,i}\varepsilon_{r.sh} - B_{c,i}\kappa_{sh}) + R_{A,i}(-B_{c,i}\varepsilon_{r.sh} + I_{c,i}\kappa_{sh})] \tag{3.16}$$

where the index i refers to the computation of the uncracked or cracked quantities.

3.3 Parametric study

This paragraph presents the results of an extensive parametric study aimed at establishing the influence of using different serviceability models in the design of the composite slabs. In particular, three service models are considered (referred to as Models A, B and C in the following for ease of reference) and these differ for the approach used to account for shrinkage effects: (A) shrinkage gradient as specified in the current Australian draft code (AS2327 Draft, 2015) ; (B) uniform shrinkage profile in which the shrinkage strains are computed as suggested in the concrete codes (AS3600, 2009; EN 1992-1-1, 2004); (C) no shrinkage effects .

In the parametric study, span lengths varied between 2 m and 6 m with length increments of 0.2 m.

Both propped and unpropped conditions of the slab during construction phases have been considered.

Two profiled sheeting, widely used in Australia, have been considered. They have been referred to in the following as profile 1 and profile 2, and their geometries are shown in figure 3.5:

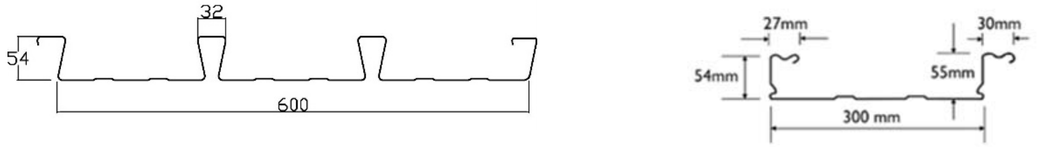

(a) Profile 1 (b) Profile 2

Fig 3.5 Geometry of the profiled sheeting used in the parametric study

The total and incremental deflection limits used are $\frac{\delta_t}{L} = 1/250$ and $\frac{\delta_{incr}}{L} = 1/500$, respectively (where L is the span length).

The superimposed permanent load and the concrete strength are equal to 1 kPa and 32 MPa respectively. The final time for the analyses is 30 years.

Based on Australian industry practice, minimum slab thickness of 120 mm were used in the design.

3.3.1 Considerations on the governing limit state for the design of composite slabs

The ultimate and the serviceability limit states considered in the analysis are expressed in terms of design ratios. For the ultimate limit states, the design ratio is defined as the ratio of the design value of the considered internal force to the design value of the resistance:

Flexural design ratio $= \frac{M_{ed}}{M_{rd}}$

Vertical shear design ratio $= \frac{V_{ed}}{V_{rd}}$

For the deflection limit states, the design ratio is defined as the ratio between the actual deflection of the slab and the design deflection (the deflection limit). For the total deflection and the incremental deflection, they are expressed as:

Total deflection design ratio $= \frac{\delta_t}{\delta_{t,lim}} = \frac{\delta_t}{L/250}$

Incremental deflection design ratio $= \frac{\delta_{incr}}{\delta_{incr,lim}} = \frac{\delta_t}{L/500}$

The limit state verification is satisfied if its design ratio is less or equal to one. The highest deign ratio governs the design of the slab thickness. An optimal design has the governing design ratio close to one.

For example, in figure 3.6, the design ratios are presented for a propped slab with profile 1 for the case of linear shrinkage profile (model A) and uniform-shrinkage (model B).

The 28th day after pouring has been considered as the starting day for the evaluation of the incremental deflection.

The graphs show the design ratio-span curves (markers connected by straight lines) and the design depth-span graph (markers only). For each adopted span length, isolated markers represent the minimum slab depth D_c which satisfies the design requirements, while connected ones represent the corresponding (to the designed slab's depth) design ratios.

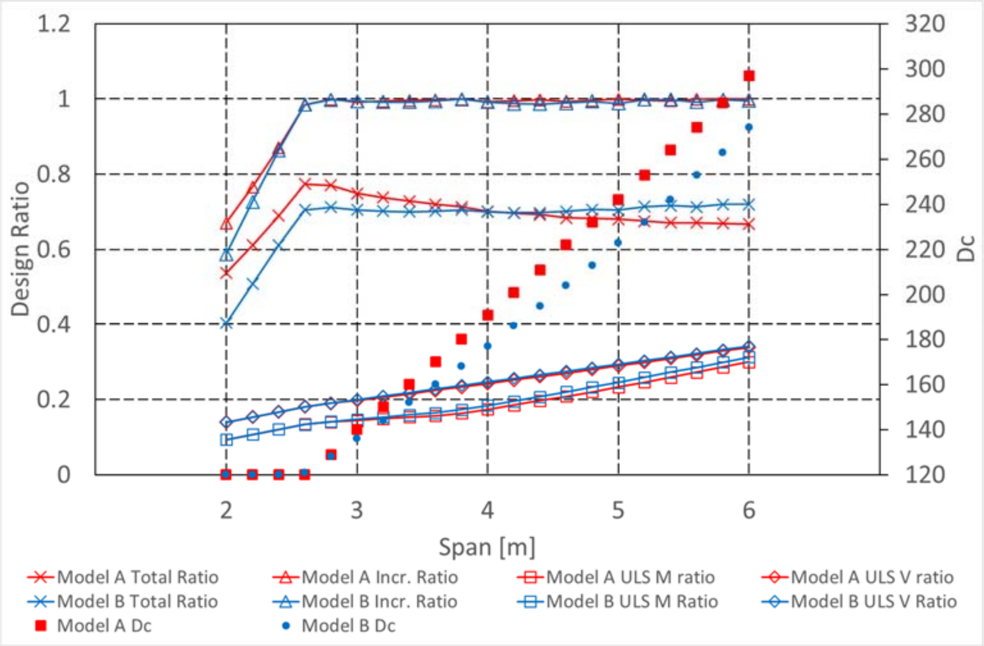

Fig 3.6 Design ratios and thickness depth for a propped slab with metal sheeting 1 in the case of model A and model B (Q = 3 kPa, tincr=28 days)

In the case of the model A, the minimum 120 mm slab thickness governs the design for span up to 2.6 m.

For span lengths larger than 2.6 m, the design requires thicker slabs. The governing limit state design becomes the incremental deflection.

The total deflection design ratio is the second highest for the slab design.

The ultimate limit state ratios are always below 0.4. This means that the thickness of the slab, provided by the serviceability limit state, ensures a large safety margin for the flexural and vertical shear limit state.

The previous trend is confirmed also for the model B. The designed depths obtained with model A and B are relatively close, while the inclusion of the linear shrinkage profile leads to thicker slab depths.

The difference between the depth obtained with model A and model B increases for larger spans. This is due to the combined action of cracking and shrinkage. The model with uniform shrinkage (model B) results more cracks in the slab than model A. This can be considered recalling equations 3.7 and 3.9: model B returns a higher value of the maximum shrinkage-induced tensile stress σ_{cs} and a consequent smaller value of M_{cr}. Because of the cracking, it is necessary a higher value of the thickness for satisfying the verifications, further details are presented in chapter 5.

The shrinkage effects depend on the size of the (uncracked) concrete part of the section and this is reflected on equations 3.15 and 3.16. A cracked slab is less affected to the shrinkage actions than an uncracked slab, because the geometric quantities are smaller. As a consequence, the slabs computed with model A are less cracked, but the shrinkage effects are large. For small spans, the combination results closer value of thickness between the two models.

In figure 3.7 the same typology of graph is used to show the results for model C. Despite the fact that effects of shrinkage are not considered, the serviceability behaviour of the slab still governs the design for span length greater than 3.8 m, while for shorter spans the minimum thickness limit (i.e. 120 mm) is adopted.

The depths obtained without considering shrinkage effect are much smaller with respect to the other models. As an example, the thickness of a 6 m span slab is equal to 297 mm for model A, 274 mm for model B and 210 mm for model C

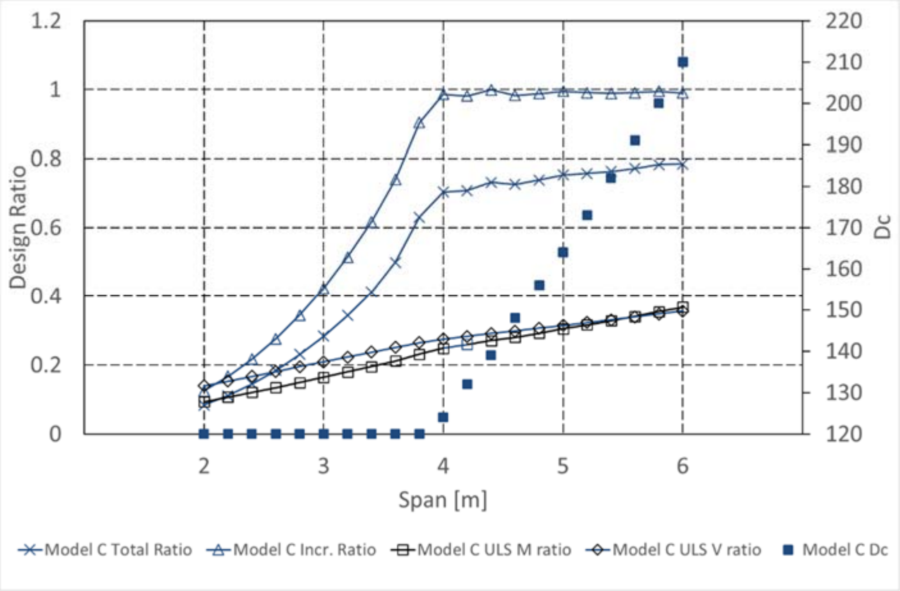

Fig 3.7 Design ratio and thickness depth for a propped slab with metal sheeting 1 in the case of model C (Q = 3 kPa, tincr=28 days)

If the same slab is not propped during the construction phase the contribution of the dead load to the deflection is neglected, and the result is a thinner slab depth. Also in this case the deflection limit state, in particular the incremental deflection, defines the depth of the slab for the three shrinkage models. It can be seen in figures 3.8:

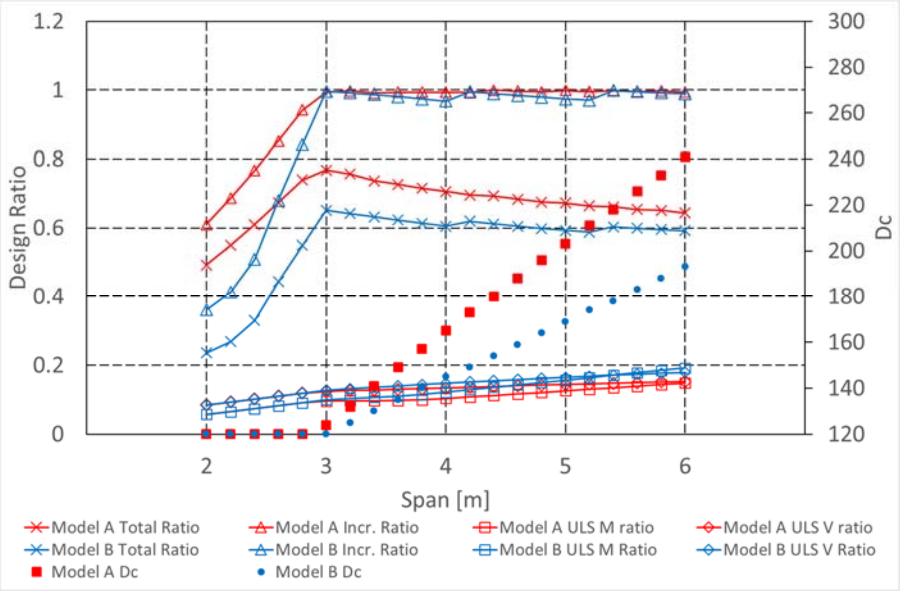

(a) Model A and Model B

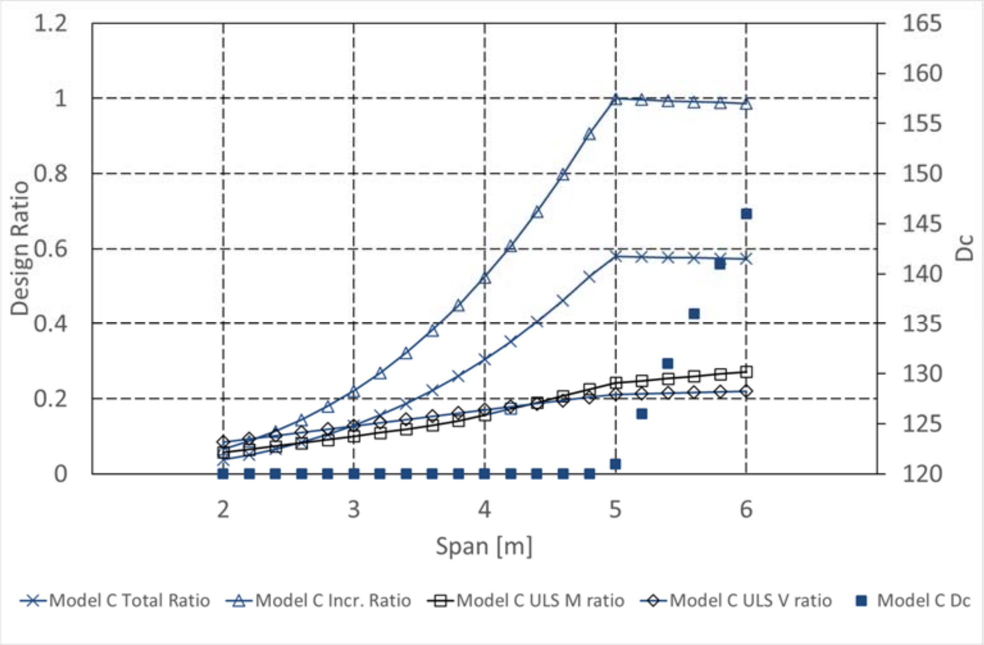

(b) Model C

Fig 3.8 Design ratios and thickness depth for an unpropped slab with metal sheeting 1 for the models A, B and C (Q = 3 kPa, tincr=28 days)

The results for the steel sheeting 2 are similar to the first one and are reported in figures 3.9 and 3.10.

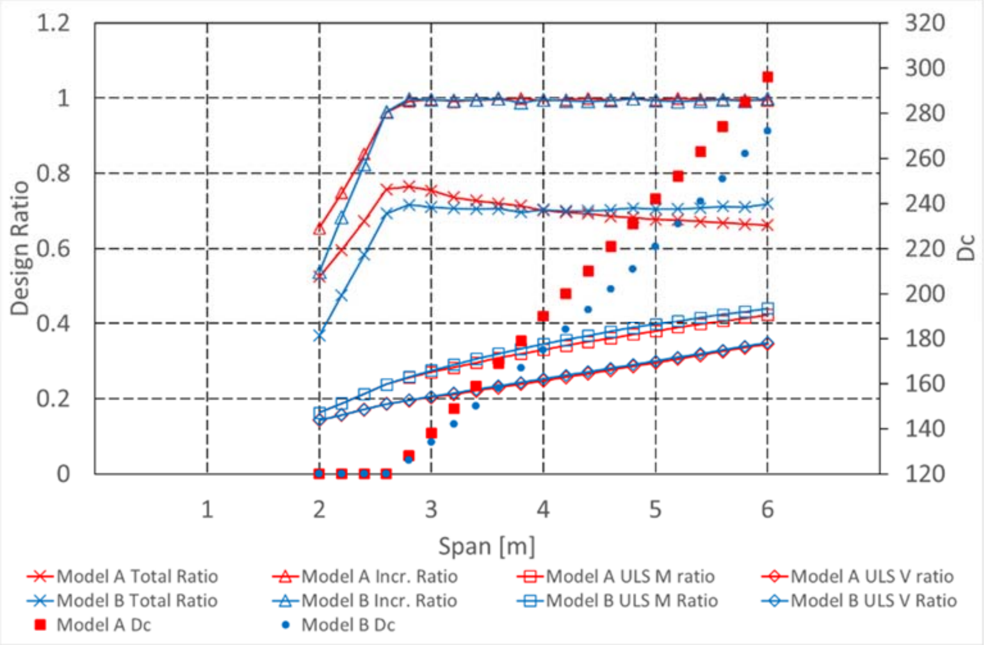

(a) Model A and B

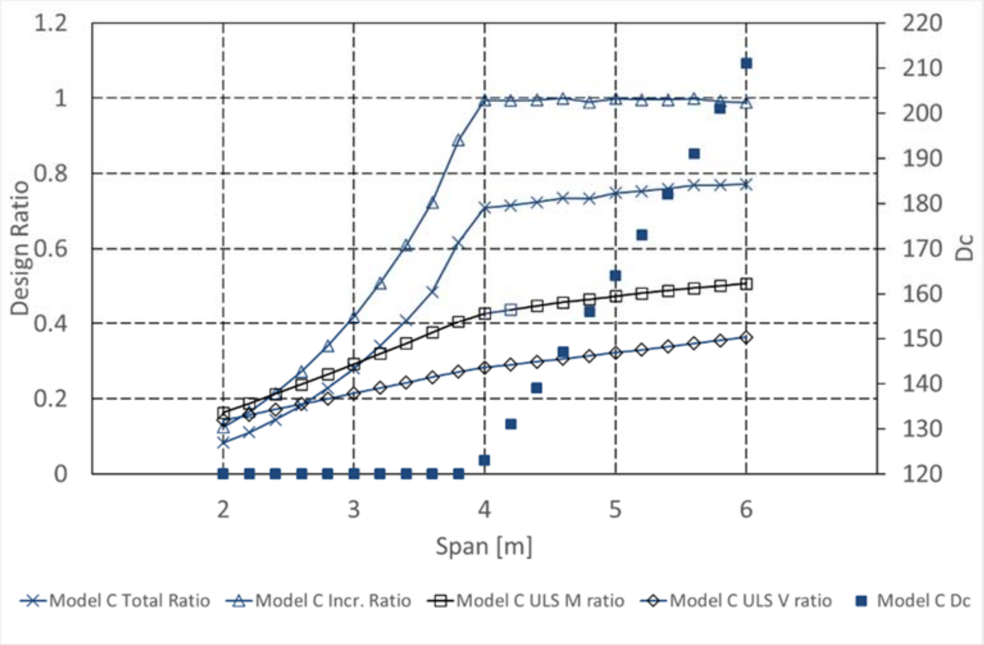

(b) Model C

Fig 3.9 Design ratios and thickness depth for a propped slab with metal sheeting 2 for the models A, B and C (Q = 3 kPa, tincr=28 days)

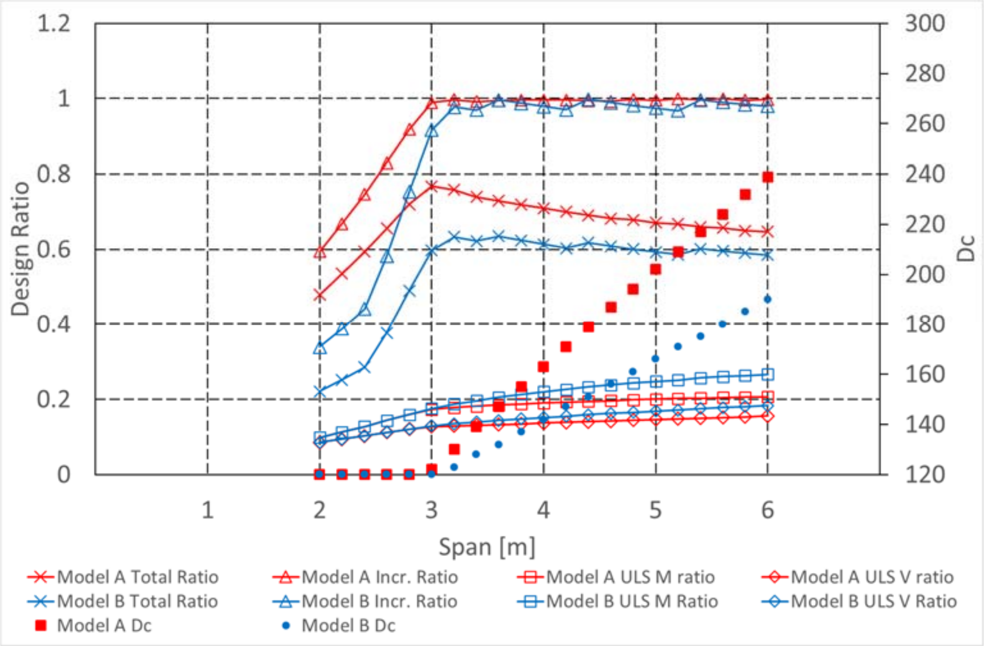

(a) Model A and B

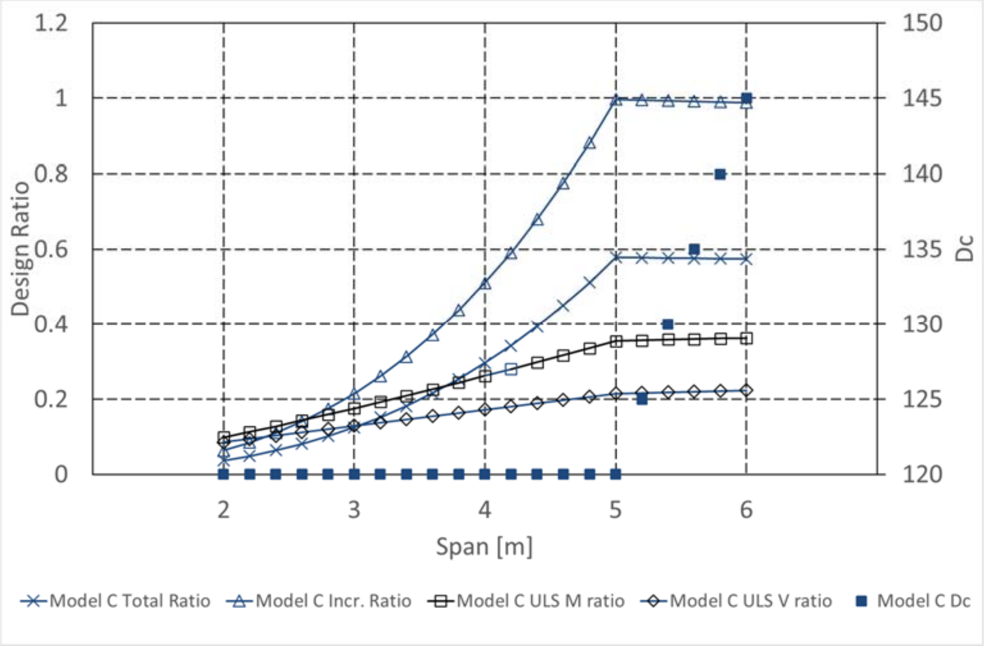

(b) Model C

Fig 3.10 Design ratios and thickness depth for an unpropped slab with metal sheeting 2 for the models A, B and C (Q = 3 kPa, tincr=28 days)

The following figures 3.11 and 3.12 show the results, for the profile 1, where the starting incremental times are 56 days and 84 days. In these cases, the total deflection curves tend to shift up and get closer to the incremental curves. This implies that the total deflection is becoming more important for the design if the partitions are built at a later date from casting. The ultimate limit state curves are still far to the serviceability curves for model A and B, but they gained importance for small spans when considering model C, as shown in figures 3.11b and 3.12b.

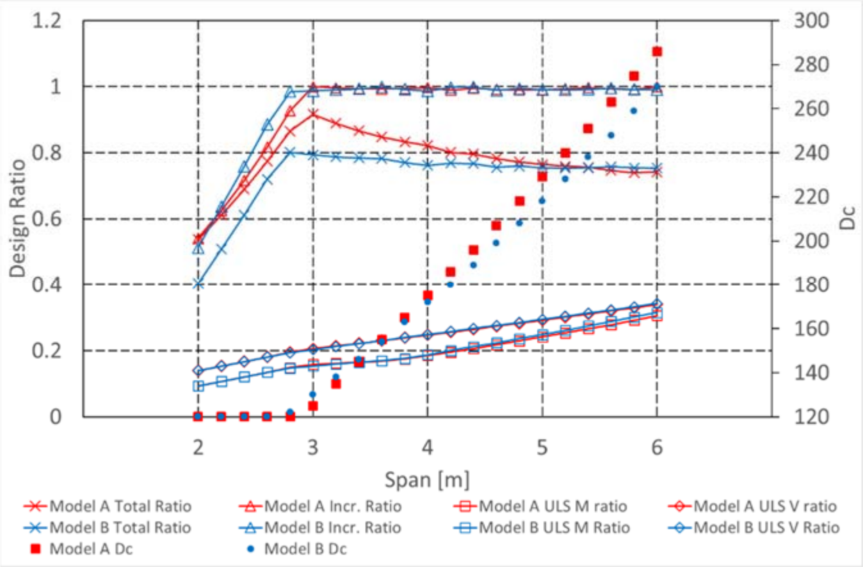

(a) Model A and Model B

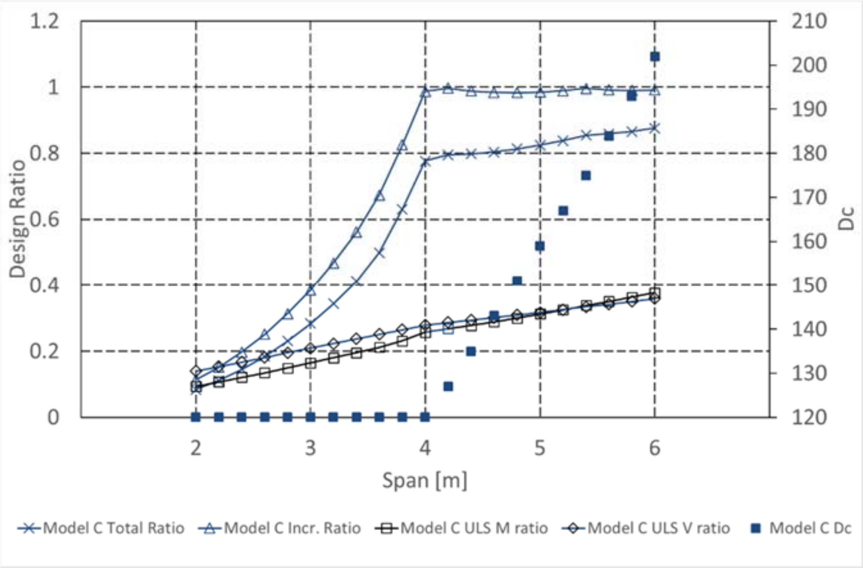

(b) Model C

Fig 3.11 Design ratios and thickness depth for a propped slab with metal sheeting 1 for the models A, B and C (Q = 3 kPa, tincr=56 days)

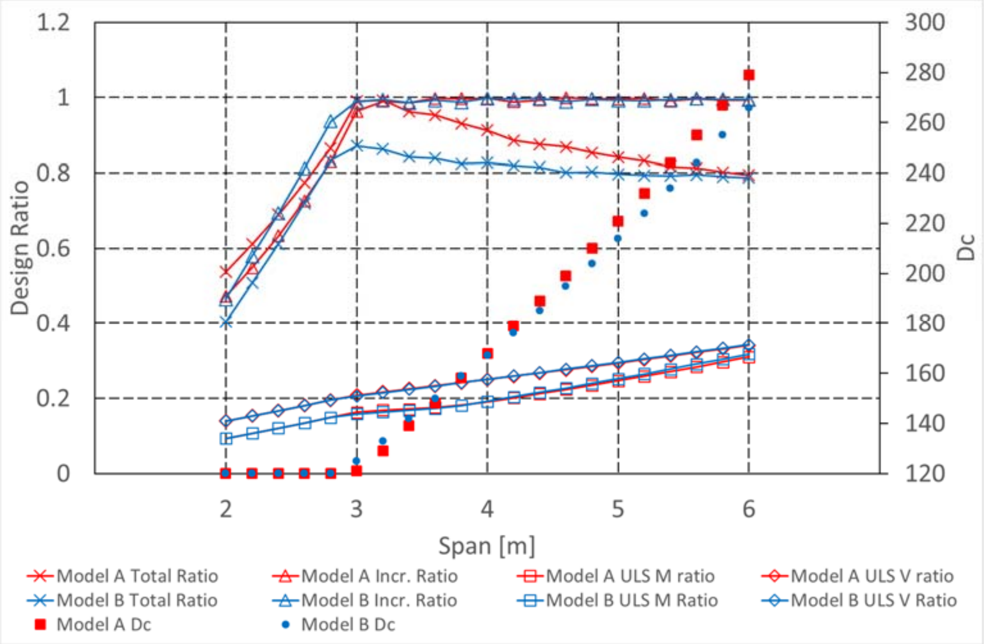

(a) Model A and Model B

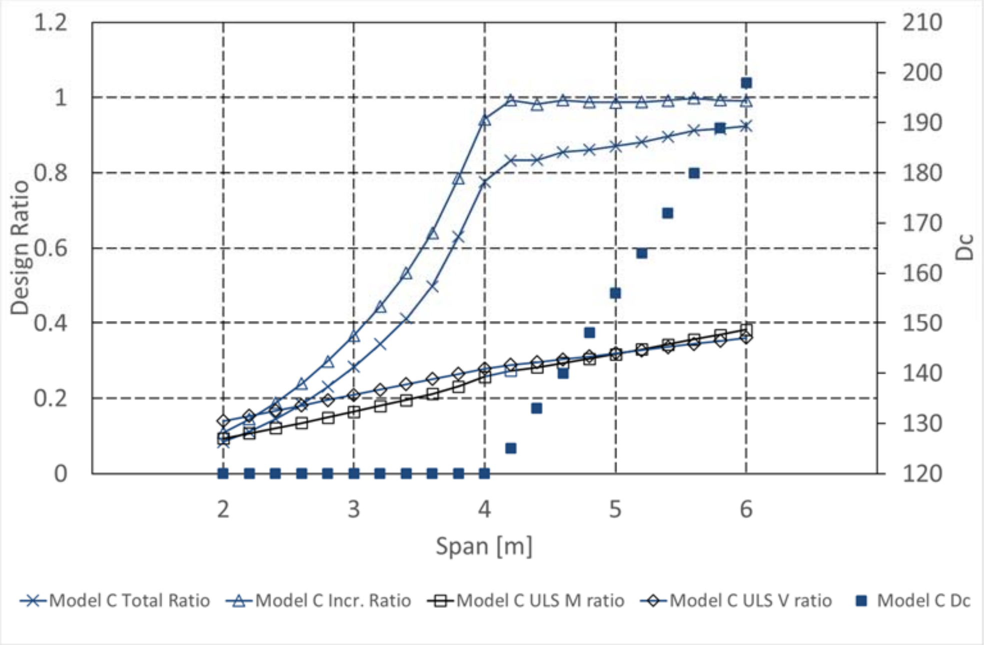

(b) Model C

Fig 3.12 Design ratios and thickness depth for a propped slab with metal sheeting 1 for the models A, B and C (Q = 3 kPa, tincr=84 days)

Results related to cases for which verification of the incremental deflections may not be needed are presented in figure 3.13. In particular, figure 3.13a highlights that the service behaviour of the slab continues to govern the design of the thickness slab. The incremental deflection curves are still plotted for completeness and they overpass unity, meaning that the slabs would not satisfy the incremental deflection requirement. In model C, the ultimate limit state design is important for small span range, in which flexural limit state and vertical shear limit state result more restrictive conditions than the serviceability criteria (although the minimum thickness has been adopted). This has been showed in figure 3.13b.

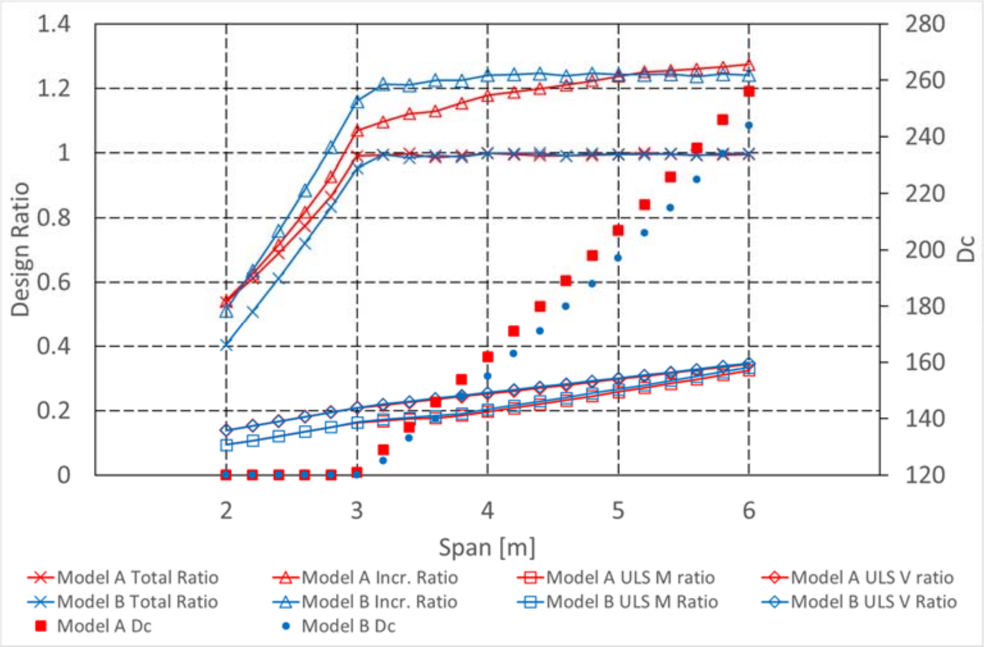

(a) Model A and Model B

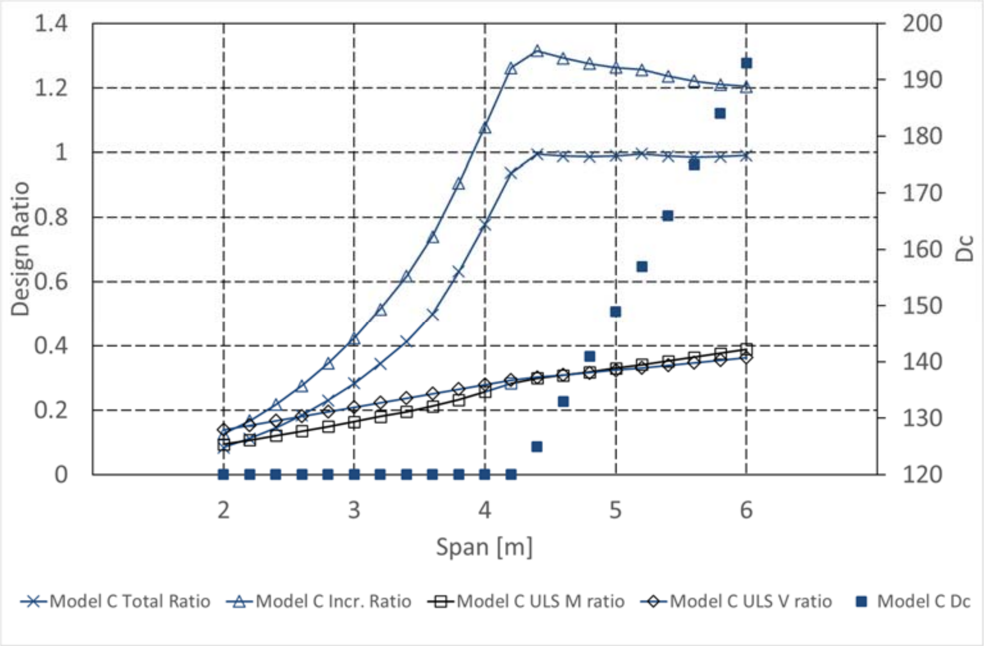

(b) Model C

Fig 3.13 Design ratios and thickness depth for a propped slab with metal sheeting 1 without considering the incremental limit as a design criterion (Q = 3 kPa)

These results have shown that the incremental deflection governs the design in all the considered cases for linear shrinkage model (model A) and uniform shrinkage model (model B). If the starting day for the incremental deflection computation is postponed, the total deflection limit becomes more important and can govern the design. When the incremental deflection check is not considered, the total deflection controls the design while the ultimate limit state requirements have not influence the slab design in the cases considered in this study. Regarding the model C, the incremental deflection governs in the span range where no minimum thickness for the slab is adopted. The ultimate limit states become significant for small spans.

The three models produce different slab thicknesses. The following figures 3.14 and 3.15 show the comparison among the designed slab thickness based on the three models, in relation to profiles 1 and 2, respectively.

The results from model A and C are shown also dimensionalised against the values computed from model B. Since the incremental deflection may be not considered as a design criterion, the results have been reported also for the case in which the incremental check has been removed.

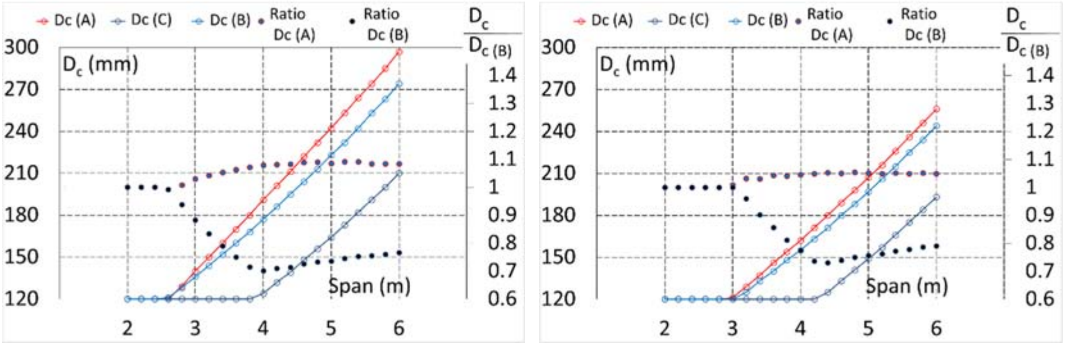

(a) propped slab, check incremental (b) propped slab, no check incremental

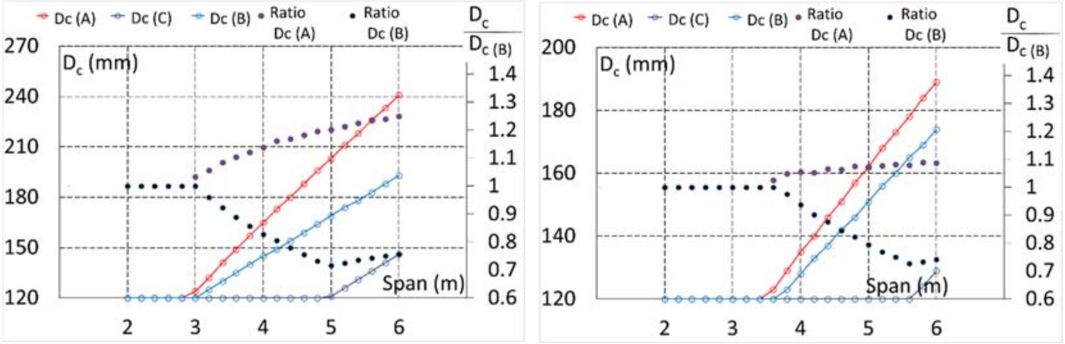

(c) unpropped slab, check incremental (d) unpropped slab, no check incremental

Fig 3.14 Comparisons among thickness depth computed using the models A, B and C for the profile 1 (Q = 3 kPa)

Considering the spans where non-minimum thickness is required, the ratios between model C and B remain in the range of 0.7 and 0.8, while the ratios calculated with model A is close to 1.1. It means that the results obtained with model C are far from the results of the models A and B in terms of the design thickness. The differences among model A and B are lower, but not negligible.

While comparing propped and unpropped cases, it is observed that the first condition results thicker slab to satisfy verifications. This is because the self-weight component is not considered applied to the composite slab in the unpropped case.

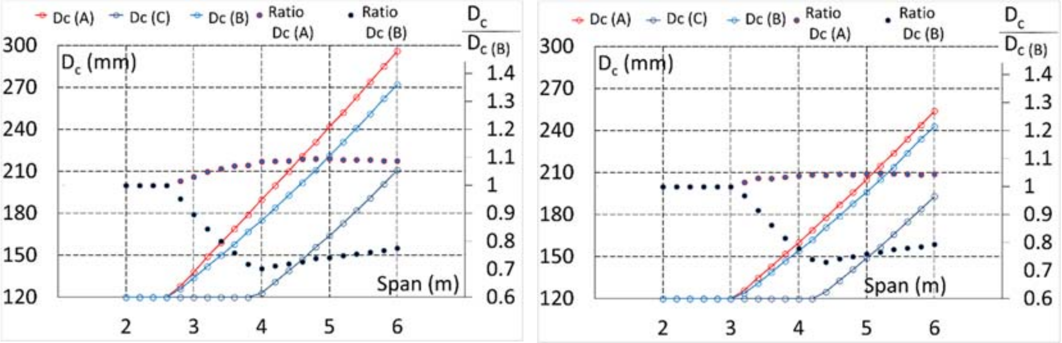

(a) propped slab, check incremental (b) propped slab, no check incremental

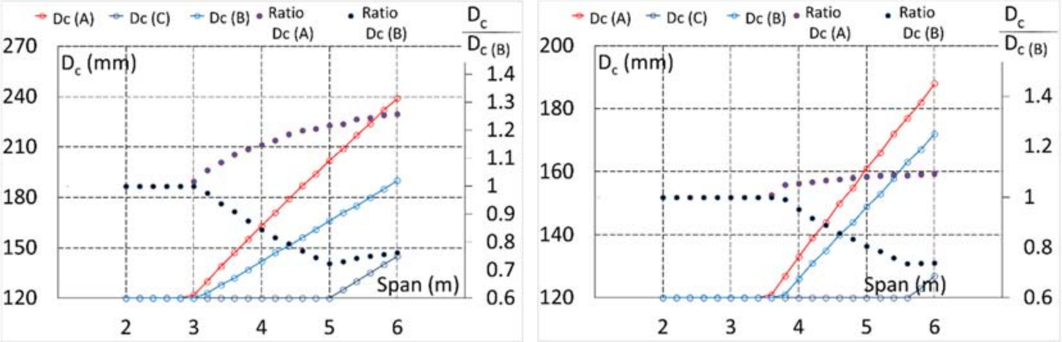

(c) unpropped slab, check incremental (d) unpropped slab, no check incremental

Fig 3.15 Comparisons among thickness depth computed using the models A, B and C for the profile 2 (Q = 3 kPa)

In the following graphs, a comparison on the incremental deflection between the three models is presented. The incremental deflection has been calculated assuming the same slab depth for all the models. The slab depth varied with the span and was determined using the design rules in the model B as a reference.

In the figures 3.16, comparisons are presented for both the cases of propped and unpropped slabs with profile 1, considering a live load value equal to 3 kPa.

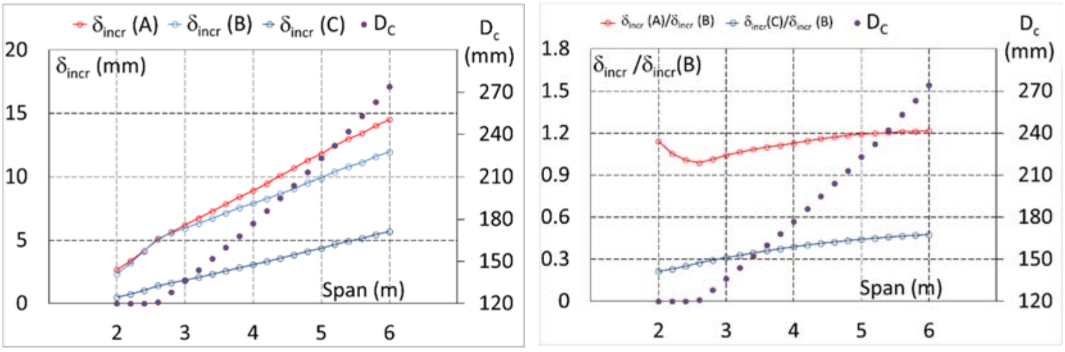

(a) propped slab (b) propped slab

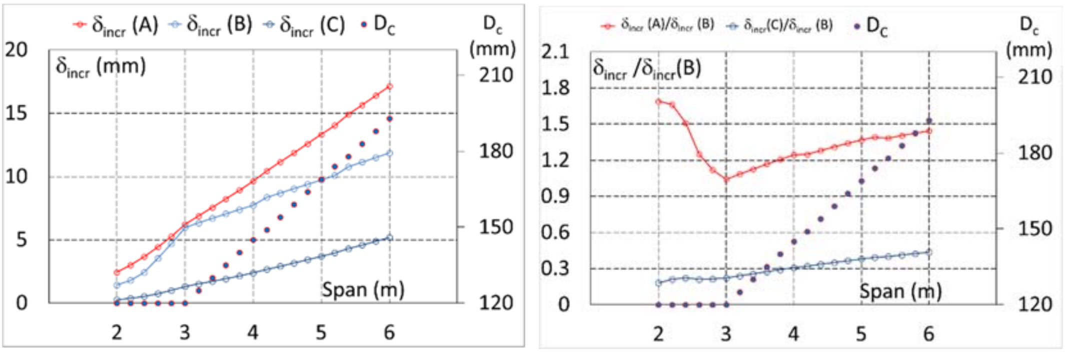

(c) unpropped slab (d) unpropped slab

Fig 3.16 Comparisons among incremental deflection computed using the models A, B and C for the profile 1 (Q = 3 kPa)

In the range of spans where the design is not governed by the minimum thickness of 120 mm, the incremental deflection calculated with model A and B are relatively close, while the values obtained with model C are much smaller.

These trends are highlighted in the figures 3.16b and 3.16d, in which the incremental deflections from model A and C have been non-dimensionalised against the values computed from model B. For propped slabs with span larger than 3 m, the ratios between the incremental deflections computed between model A and B remain close to 1.2.

For completeness, the minimum slab limit of 120 mm is removed from the design calculations in figures 3.17 and figures 3.18. In these cases, the deflection computed with model B, for propped slabs, is higher than the deflection computed with model A for span up to 3 m (figure 3.17).

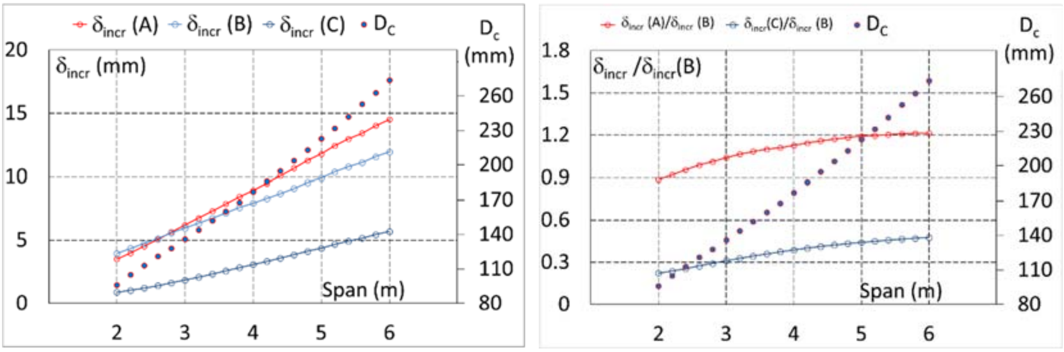

Fig 3.17 Comparisons among incremental deflection computed using the models A, B and C for the profile 1 (Q = 3 kPa), without considering the minimum slab thickness limit for 120 mm

For the unpropped slabs, the difference between the values obtained with linear shrinkage and uniform shrinkage increase (as shown in the figure 3.16d, the ratios range from about 1 to 1.5). In the figures 3.18 and 3.19 the same trends are depicted also for the profile 2.

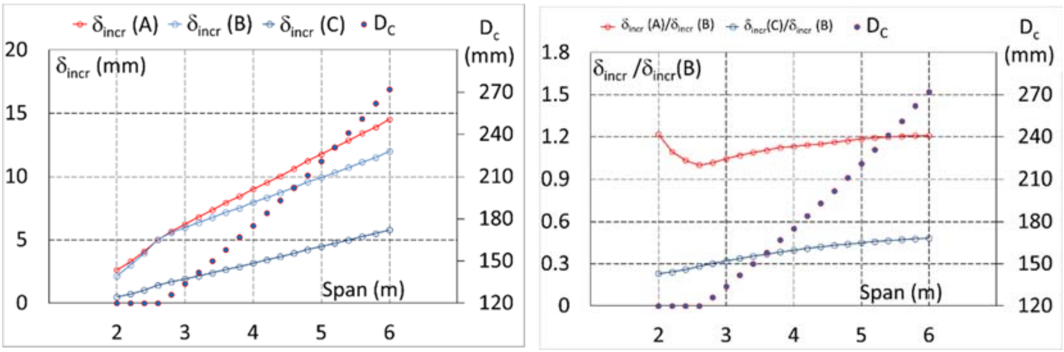

(a) propped slab (b) propped slab

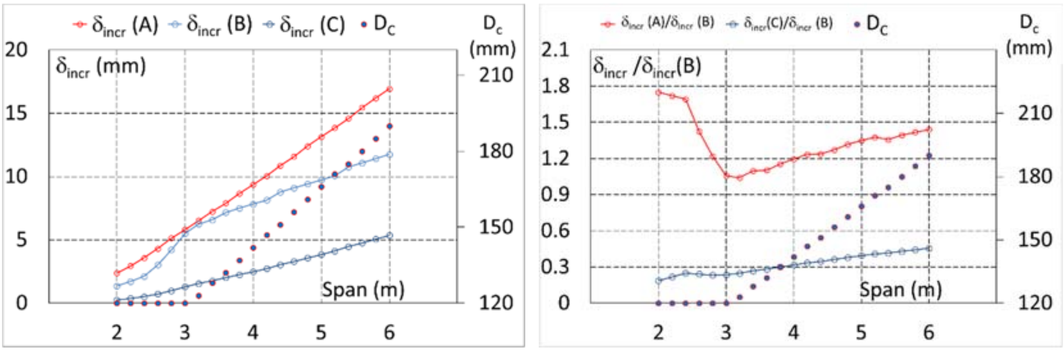

(c) unpropped slab (d) unpropped slab

Fig 3.18 Comparisons among incremental deflection computed using the models A, B and C for the profile 2 (Q = 3 kPa)

The calculations of the incremental deflection assuming the starting day equal to 56 and 84 confirm the trends previously shown. The results of those analyses are reported in figures 3.19 and 3.20 for propped slabs constructed with profile 1.

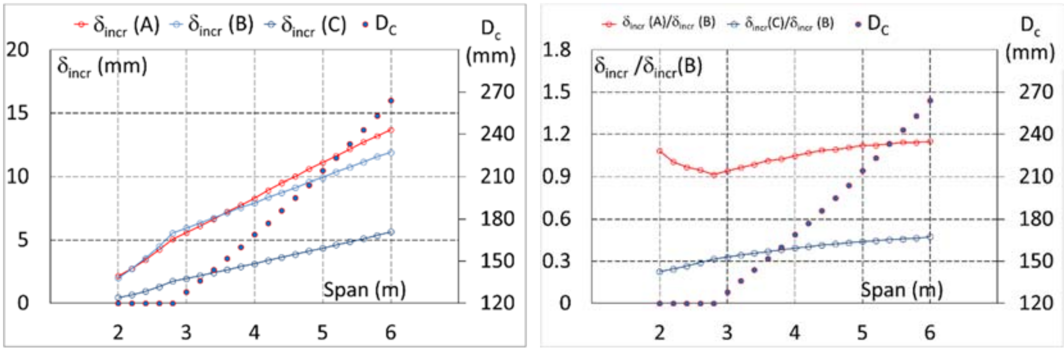

Fig 3.19 Comparisons among incremental deflection computed using the models A, B and C for t_{incr}=56 days (Q = 3 kPa, profile 1)

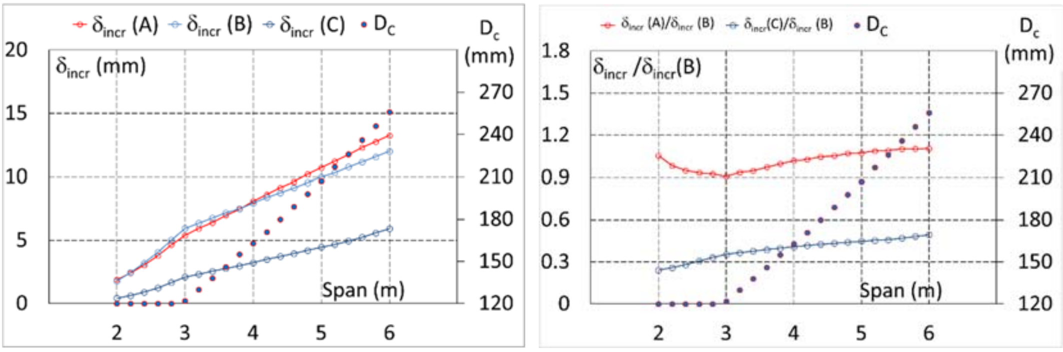

Fig 3.20 Comparisons among incremental deflection computed using the models A, B and C for t_{incr}=84 days (Q = 3 kPa, profile 1)

This section has shown the significant differences on the incremental deflection values obtained with models A and B when they are compared with model C. The design performed considering uniform shrinkage could return smaller value of incremental deflection with respect to the linear shrinkage model.

In the following and last section, the design limit of the incremental deflection is no more considered to evaluate the influence of total deflection design criteria.

3.3.2 Considerations on the total deflection

Not considering the check on the incremental deflection does not influence the trend, which has been already highlighted in the previous sections.

The figures 3.21 and 3.22 show the comparison for the profile 1 and 2 with a live load of 3 kPa. Further results for a live load of 10 kPa are presented in the appendix. The differences between the three models slightly decrease for higher levels of live load. The same trend is highlighted when thicker profile sheeting is used. Relevant comparisons are reported in appendix.

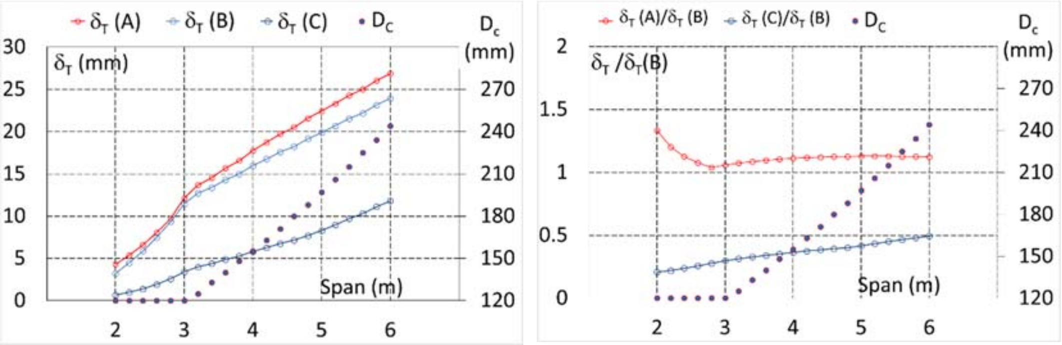

(a) propped slab

(b) propped slab

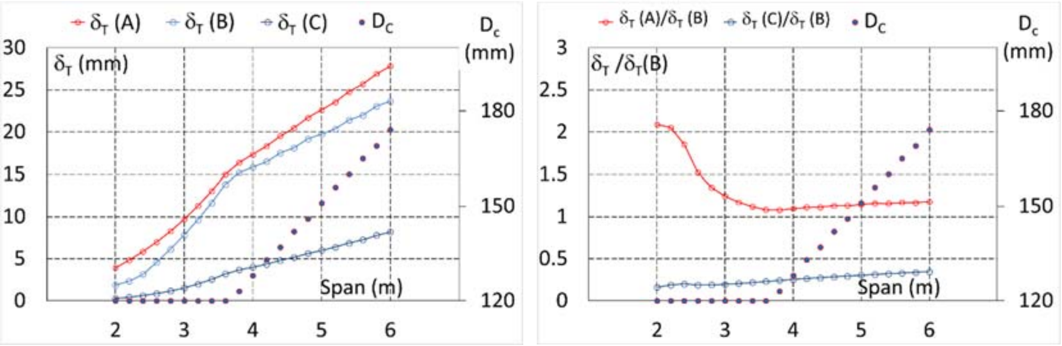

(c) unpropped slab

(d) unpropped slab

Fig 3.21 Comparisons among total deflection computed using the models A, B and C for the profile 1 (Q = 3 kPa)

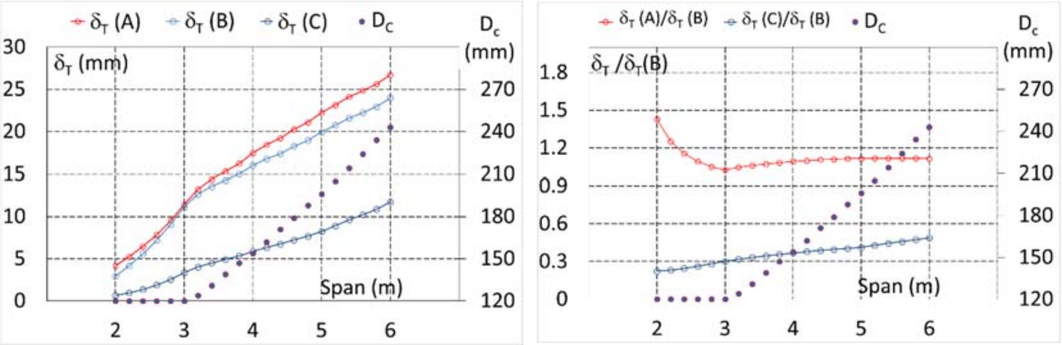

(a) propped slab

(b) propped slab

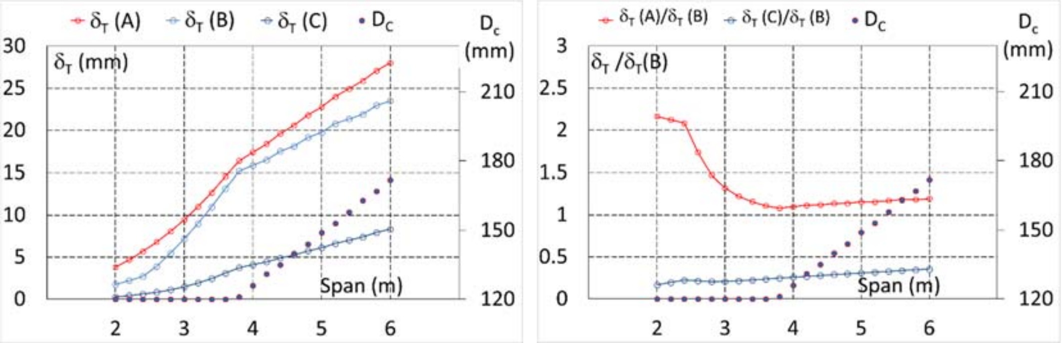

(c) unpropped slab

(d) unpropped slab

Fig 3.22 Comparisons among total deflection computed using the models A, B and C for the profile 2 (Q = 3 kPa)

In summary, this chapter has shown the significant importance of the serviceability limit states on the design of composite steel-concrete slabs.

Comparisons among the three different models have been made such as: comparisons on incremental deflection, on the designed thickness and on the total deflection.

All the results highlight the significant differences between the design quantities calculated with model A and B when compared to those of model C, therefore emphasizing the importance of including shrinkage effects in the service calculation.

The value of the slab depth and deflection carried out with model A are higher in almost all the cases when compared with the results obtained with model B.

For small span, it was observed that the model B could give more conservative results than model A. This is due to the higher level of cracking on the slab computed with the model B with respect to the model A. Since this last remark is related to a few cases (i.e span less than 3 m), it is recommended to use the model A to account for shrinkage effects, because validated against long-term test on composite slabs and is more conservative than the other models in almost all the cases.

Despite the differences on the above described design results of the three models, real slabs do not use to suffer of excessive deflection in real structures. Possible explanations can be as follows:

- Real slabs use to be continuous over two spans (at least) and, for this reason, they tend to deflect less than a simply supported slab, as international standards allow to consider a continuous slab.
- Floor finishes could influence the drying shrinkage. The floor finishes could mitigate the shrinkage effects and, therefore, the deflection of the slab.

The ultimate limit state conditions are far to govern the design of the composite slab when shrinkage is considered in the analysis.

If the effect of shrinkage is neglected, the ultimate limit state verifications become significant for small spans (despite the design is governed by the minimum slab thickness limit of 120 mm).

4 Finite Element Model

4.1 Introduction

This chapter provides a description of the analytical model adopted for the analysis of the service behaviour of composite steel-concrete slabs. The numerical implementation of the model carried out based on the finite element method is also presented, providing insight into the various steps of the numerical formulation capable of handling the time-dependent behavior of the concrete and material nonlinearities, relying on the Newton-Raphson method to solve the nonlinear equations resulting from the formulation. The formulation used for the finite element is a displacement-based type.

4.2 Euler-Bernoulli beam model and weak form

The behavior of a composite floor slab is governed by its flexural deformation and, for this reason, the Euler–Bernoulli beam model has been adopted in this study to predict its response. Perfect bond is assumed between the concrete and the reinforcement, and full shear interaction is adopted between the metal sheeting and concrete, i.e. no slip can occur between the slab and the sheeting. The cross-section is assumed to be symmetric about the y-axis, and no torsion and out-of-plane effects are considered. Plane sections are assumed to remain plane and perpendicular to the beam axis after deformations.

4.2.1 Field displacements

The kinematic behaviour of the Euler-Bernoulli beam model is illustrated in figure 4.1. For a point Q lying on the x axis, its kinematic is described by its displacement along the member axis $u(x)$ (commonly referred as axial displacement) and by its deflection $v(x)$.

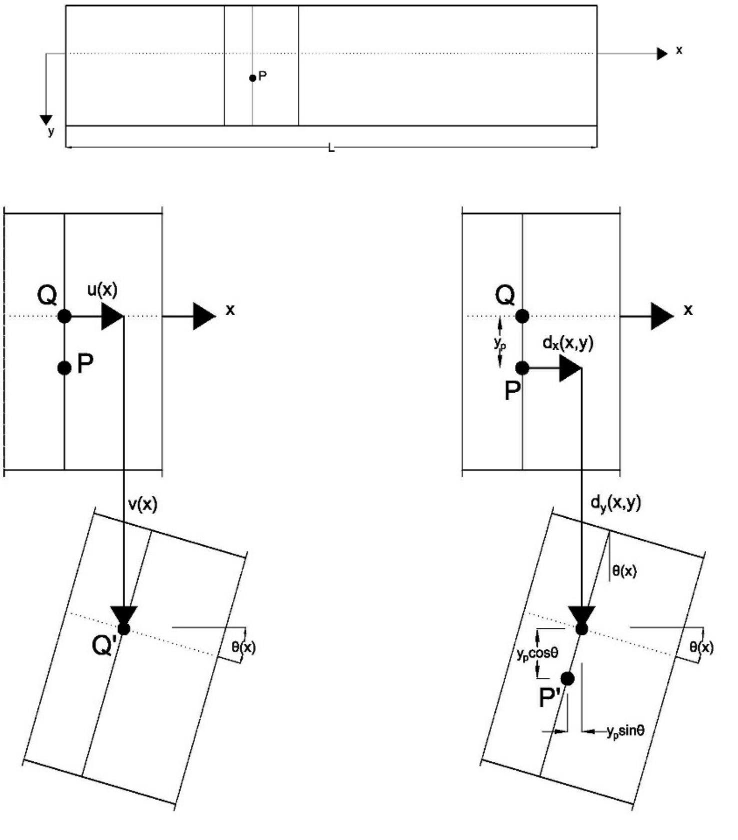

x
P
y
L
Q
u(x)
x
P
v(x)
Q'
θ(x)
Q
x
y_p
d_x(x,y)
P
d_y(x,y)
θ(x)
θ(x)
y_pcosθ
P'
y_psinθ

Fig 4.1 Displacement field

The displacement field of a point P located away from the member axis can be expressed as follows:

$$d_x(x,y) = u(x) - y\ sin\theta(x) \tag{4.1a}$$

$$d_y(x,y) = v(x) - \mathrm{y} + y\ cos\theta(x) \tag{4.1b}$$

where $u(x)$, $v(x)$ and $\theta(x)$ represent the axial displacement, deflection and rotation, respectively, at a particular cross-section located at x (figure 4.1).

In the framework of small displacements, suitable for the composite slab analyses performed in this study, the following simplifications can be introduced:

$$cos\theta(x) = 1 \quad sin\theta(x) = \theta(x)$$

(4.2 a,b)

and, under the Euler-Bernoulli assumptions of plane sections remaining perpendicular to the member axis after deformations, the following relationship exists between the rotation and deflection:

$$\theta(x) = v(x)'$$

(4.3)

Based on the assumptions introduced in equations (4.2) and (4.3), it is possible to rewrite equations (4.1) as follows:

$$d_x(x, y) = u(x) - y\, v'(x)$$
$$d_y(x, y) = v(x)$$

With this kinematic representation, the only non-zero deformation component is the axial strain component, defined as:

$$\varepsilon_x = \frac{d}{dx}\big(dx(x, y)\big) = u'(x) - y\, v''(x)$$

(4.4)

where $v''(x) = \theta'(x) = \kappa$ is the curvature of the beam.

4.2.2 Equilibrium

Equilibrium is here enforced by means of the principal of virtual work, which equates the internal work to the external work of the beam for each virtual kinematic-consistent variation of the displacement field. The internal work is the work produced by the internal stress and the generic admissible variation on the deformation field. The external work is the work due to external actions and the virtual admissible variation of the displacements. The external forces applied to the beam are shown in figure 4.2.

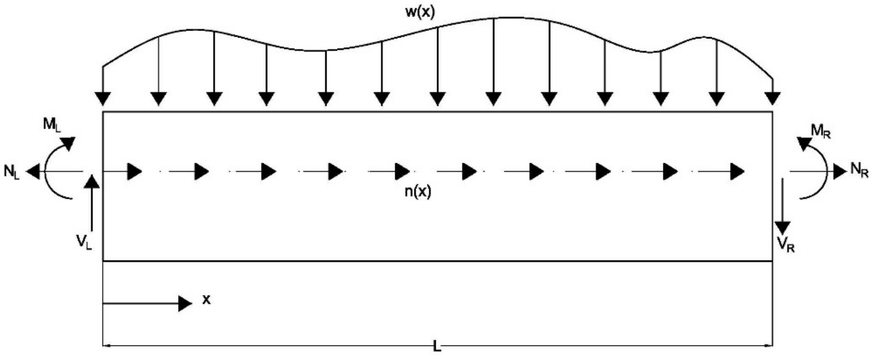

Fig 4.2 Member loads and nodal actions

The principle of virtual work for an element with length L is expressed as follows:

$$\int_L \int_A \sigma_x \hat{\varepsilon}_x dx =$$

$$= \int_L (w\hat{v} + n\hat{u})dx + S_L\hat{v}_L + N_L\hat{u}_L + M_L\hat{\theta}_L + S_R\hat{v}_R + N_R\hat{u}_R + M_R\hat{\theta}_R \tag{4.5}$$

where this relationship is valid for each virtual admissible variation of the displacements and corresponding strains. The terms $w(x)$ and $n(x)$ represent the vertical and horizontal distributed load along beam axis, while subscript L and R refers to the left or right end of the beam.

Including the equation of axial strain component (equation 4.4), the internal work can be rewritten as:

$$\int_L \int_A \sigma_x \hat{\varepsilon}_x dAdx = \int_L \int_A \sigma_x(\widehat{u'} - y\,\widehat{v}'')dAdx$$

Introducing the definition of the internal actions *N* and *M*:

$$N = \int_L \sigma_x dL$$

$$N = -\int_L y\,\sigma_x dL$$

The integral at the cross section on the left hand side of equation (4.5) can be replaced by:

$$\int_L \left(N\widehat{u'} + M\,\widehat{v}''\right)dx =$$

$$= \int_L (w\hat{v} + n\hat{u})dx + S_L\hat{v}_L + N_L\hat{u}_L + M_L\hat{\theta}_L + S_R\hat{v}_R + N_R\hat{u}_R + M_R\hat{\theta}_R$$

This relationship can be rearranged in matrix form and isolating the terms with N and M:

$$\int_L \begin{bmatrix} N \\ M \end{bmatrix} \cdot \begin{bmatrix} \widehat{u'} \\ \widehat{v}'' \end{bmatrix} dx = \int_L \begin{bmatrix} n \\ w \end{bmatrix} \cdot \begin{bmatrix} \hat{u} \\ \hat{v} \end{bmatrix} dx + \begin{bmatrix} N_L \\ S_L \\ M_L \end{bmatrix} \cdot \begin{bmatrix} \hat{u}_L \\ \hat{v}_L \\ \hat{\theta}_L \end{bmatrix} + \begin{bmatrix} N_R \\ S_R \\ M_R \end{bmatrix} \cdot \begin{bmatrix} \hat{u}_R \\ \hat{v}_R \\ \hat{\theta}_R \end{bmatrix} \tag{4.6}$$

In equation (4.7) the nodal actions included on the right-hand side of equation (4.6) have been ignored, because these can be included in the beam analysis during the assembly of the load vector:

$$\int_L \begin{bmatrix} N \\ M \end{bmatrix} \cdot \begin{bmatrix} \widehat{u'} \\ \widehat{v}'' \end{bmatrix} dx = \int_L \begin{bmatrix} n \\ w \end{bmatrix} \cdot \begin{bmatrix} \hat{u} \\ \hat{v} \end{bmatrix} dx \tag{4.7}$$

and introducing the notation:

$$\boldsymbol{r} = \begin{bmatrix} N \\ M \end{bmatrix}$$

$$\hat{\boldsymbol{e}} = \begin{bmatrix} \hat{u} \\ \hat{v} \end{bmatrix}$$

$$\hat{\boldsymbol{\varepsilon}} = \begin{bmatrix} \widehat{u'} \\ \widehat{v}'' \end{bmatrix} = \begin{bmatrix} \partial & 0 \\ 0 & \partial^2 \end{bmatrix} \begin{bmatrix} \hat{u} \\ v \end{bmatrix} = \boldsymbol{A}\hat{\boldsymbol{e}}$$

$$\boldsymbol{p} = \begin{bmatrix} n \\ w \end{bmatrix}$$

(4.8 a-d)

the equation (4.7) is written in terms of vector:

$$\int_L \boldsymbol{r} \cdot \boldsymbol{A}\hat{\boldsymbol{e}}\, dx = \int_L \boldsymbol{p} \cdot \hat{\boldsymbol{e}} dx$$

$$\forall \hat{\boldsymbol{e}}$$

(4.9)

In this form, the constitutive laws for the materials are not yet specified and will be introduced in order to compute the internal actions $\boldsymbol{r}$ as a function of the displacements $\hat{\boldsymbol{e}}$.

4.3 Nonlinear Finite element formulation

4.3.1 Shape Functions

The generalized displacements are approximated by means of polynomials. The axial displacement is modelled by a parabolic function and the deflection with a cubic polynomial. The general equations are expressed as follows:

$$u(x) = a_0 + a_1 x + a_2 x^2$$
$$v(x) = b_0 + b_1 x + b_2 x^2 + b_3 x^3$$

(4.10 a,b)

Where the coefficients $a_i$and $b_j$are the unknown coefficients to be determined from the analysis.

Starting from the axial displacement the three coefficients in the equations (4.10) can be replaced with three other terms. The three terms are the displacement values at the left node u_L, in the middle of the element u_M at the right node u_R.

$$u(x=0) = a_0 + a_1\, 0 + a_2\, 0^2 = u_L$$
$$u(x=L/2) = a_0 + a_1 \frac{L}{2} + a_2 \left(\frac{L}{2}\right)^2 = u_M$$
$$u(x=L) = a_0 + a_1 L + a_2 (L)^2 = u_R$$

(4.11 a,b,c)

Solving the system of equations (4.11) with respect to a_0, a_1 and a_2, the three terms are found:

$$a_0 = u_L$$
$$a_1 = \frac{3\, u_L - 4\, u_M + u_R}{L}$$
$$a_2 = \frac{2(\, u_L - 2\, u_M + u_R)}{L^2}$$

Substituting in the polynomial equation of u (equation 4.10a):

$$u = u_L - \frac{3\,u_L - 4\,u_M + u_R}{L}x + \frac{2(\,u_L - 2\,u_M + u_R)}{L^2}x^2$$

and collecting the nodal displacements, it follows:

$$u = N_{u1}u_L + N_{u2}u_M + N_{u3}u_R$$

where:

$$N_{u1} = 1 - \frac{3x}{L} + \frac{2x^2}{L^2}$$

$$N_{u2} = \frac{4x}{L} - \frac{4x^2}{L^2}$$

$$N_{u3} = -\frac{x}{L} + \frac{2x^2}{L^2}$$

are the shape functions for the axial displacement. They are illustrated in figure 4.3

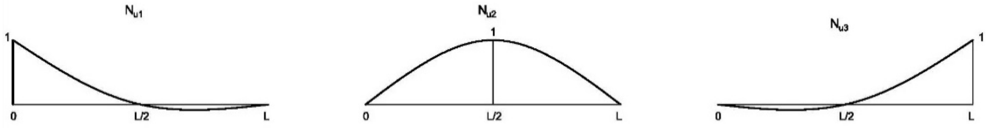

Fig 4.3 Shape functions used for the approximation of u

In a similar way the shape functions for the deflection component are obtained, assuming as nodal quantities both displacements and rotations:

$$N_{v1} = 1 - \frac{3x^2}{L^2} + \frac{2x^3}{L^3}$$

$$N_{v2} = x - \frac{2x^2}{L} + \frac{x^3}{L^2}$$

$$N_{v3} = \frac{3x^2}{L^2} - \frac{2x^3}{L^3}$$

$$N_{v4} = -\frac{x^2}{L} + \frac{x^3}{L^3}$$

which are illustrated in figure 4.4

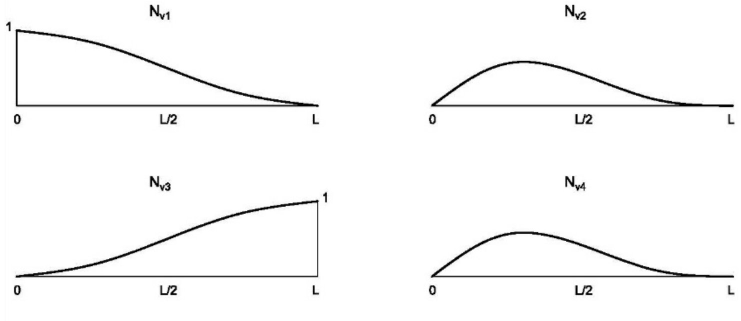

Fig 4.4 Shape functions used for the approximation of v

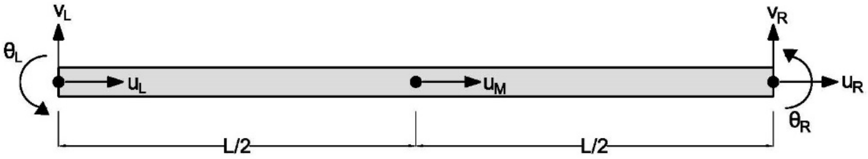

Fig 4.5 7-dof Euler Bernoulli beam

In the figure 4.5, the 7-dof Euler Bernoulli beam finite element is shown. It is worth to notice that the shape functions reflect a positive vertical displacement when it's upward. This convention has been used in the finite element program and it is opposite to the one showed in the Euler Bernoulli beam formulation.

The equations of the displacement field can be rearranged in matrix form:

$$\boldsymbol{e} = \begin{bmatrix} u \\ v \end{bmatrix} \approx \begin{bmatrix} N_{u1} & 0 & 0 & N_{u2} & N_{u3} & 0 & 0 \\ 0 & N_{v1} & N_{v2} & 0 & 0 & N_{v3} & N_{v4} \end{bmatrix} \begin{bmatrix} u_L \\ v_L \\ \theta_L \\ u_M \\ u_R \\ v_R \\ \theta_R \end{bmatrix} = \boldsymbol{N_e d_e} \tag{4.12}$$

where $\boldsymbol{N_e}$ is the matrix of the shape functions and $\boldsymbol{d_e}$ is the vector of the element's nodal displacements.

This proposed 7-dof finite element represents the simplest elements that fulfils the consistency requirements by approximating the displacements by means of polynomial and thereby avoids potential locking problems that may arise when the member local *x*-axis does not pass through the centroid of the member cross-section. A formulation with the origin of the reference system not necessarily coincident with the centroid of the section is fundamental when dealing with material nonlinearities as the location of the actual centroid of a cross-section with nonlinear material behaviour varies depending on the level of applied loading or deformation. From a practical viewpoint, the consistency requirement is satisfied when the independent displacements (or their derivatives) present in the expression of the strains of the model possess the same order of approximation (i.e. *u*' and *v*" have the same order) (Ranzi, Gilbert, 2014).

Combining equation (4.8c) with equation (4.12) the variables describing the strain distribution can be expressed as follows:

$$\boldsymbol{\varepsilon} = \boldsymbol{A}\boldsymbol{N_e}\boldsymbol{d_e} = \boldsymbol{B}\boldsymbol{d_e}$$

(4.13)

$$\boldsymbol{B}^T = \begin{bmatrix} N'_{u1} & 0 \\ 0 & N''_{v1} \\ 0 & N''_{v2} \\ N'_{u2} & 0 \\ N'_{u3} & 0 \\ 0 & N''_{v3} \\ 0 & N''_{v4} \end{bmatrix}$$

where matrix **B** describes the strain field in the element. By substituting the equation (4.12) and (4.13) into (4.9), the so-called discretized weak form of the problem expressed in terms of nodal displacements is produced:

$$\int_L \boldsymbol{B^T}\boldsymbol{r} \cdot \widehat{\boldsymbol{d}}_{\boldsymbol{e}}\, dx = \int_L \boldsymbol{N_e^T}\boldsymbol{p} \cdot \widehat{\boldsymbol{d}}_{\boldsymbol{e}}\, dx$$

$$\forall\, \widehat{\boldsymbol{d}}_{\boldsymbol{e}}$$

(4.14)

4.4 Nonlinear analysis using the Newton-Raphson method

4.4.1 Overview of the Newton-Raphson Method

The Newton-Raphson algorithm is an iterative procedure suitable for the solution of nonlinear problem. The nonlinear equilibrium equations can be written in general form as:

$$\boldsymbol{K}(\boldsymbol{D}) = \boldsymbol{Q} \tag{4.15}$$

Where Q is the vector of external loads applied to the structure and $\mathbf{K(D)}$ are the internal actions vector. The latter is nonlinearly dependent on the displacement vector D. The solution found on a generic iteration i is based on the results coming from the previous iteration. If the iteration is the first one, an initial hypothesized set of results is assumed (usually zero displacements or the solution of the previous load-step). The results are then improved in subsequent iterations until a convergence criterion is satisfied.

Considering the result from a generic i-th iteration $\boldsymbol{D}^{(i)}$, the solution of the next iteration is computed by approximating the nonlinear equations (4.15) with the first term of its series expansion:

$$\boldsymbol{K}\left(\boldsymbol{D}^{(i+1)}\right) \approx \boldsymbol{K}\left(\boldsymbol{D}^{(i)}\right) + \boldsymbol{K_t}\left(\boldsymbol{D}^{(i)}\right)\Delta\boldsymbol{D}^{(i)} = \boldsymbol{Q}$$

in which $\Delta\boldsymbol{D}^{(i)}$ is the unknown displacement increment vector to sum up to the displacement of the previous iteration, in order to get the new solution:

$$\boldsymbol{D}^{(i+1)} = \boldsymbol{D}^{(i)} + \Delta\boldsymbol{D}^{(i)}$$

The tangent stiffness matrix $\boldsymbol{K_t}\left(\boldsymbol{D}^{(i)}\right)$ describes the tangent behaviour of the structure based on the stiffness calculated with $\boldsymbol{D}^{(i)}$. The equation can be re-organized to highlight the part related to the unknown $\Delta\boldsymbol{D}^{(i)}$:

$$\boldsymbol{K_t}\left(\boldsymbol{D}^{(i)}\right)\Delta\boldsymbol{D}^{(i)} = \boldsymbol{Q}_{\boldsymbol{R}}^{(i)}$$

(4.16)

where

$$\boldsymbol{Q}_{\boldsymbol{R}}^{(i)} = \boldsymbol{Q} - \boldsymbol{K}\left(\boldsymbol{D}^{(i)}\right)$$

(4.17)

is usually called residual.

The i-th iteration solution can be then determined and the convergence of the final solution has to be evaluated. The convergence criteria are usually based on check of either residual value or displacements value:

$$norm_1 = \frac{\left|\Delta\boldsymbol{D}^{(i)}\right|}{\left|\boldsymbol{D}^{(i+1)}\right|}$$

$$norm_2 = \frac{\left|\boldsymbol{Q}_R^{(i+1)}\right|}{|\boldsymbol{Q}|}$$

(4.18 a,b)

If the value is over a certain tolerance, then another iteration is required; otherwise the solution is convergent. In this model $norm_1$ and $norm_2$ are implemented both. The norm $norm_1$ is preferred in the analysis, because shrinkage produces deflection without the presence of external load. If no loads are applied, $norm_2$ cannot be used, because the denominator of its formula would be zero. The resume of the strategy of the Newton-Raphson methods is illustrated in figure 4.6. The first iteration starts by using the initial tangent stiffness $\boldsymbol{K_t}\left(\boldsymbol{D}^{(1)}\right)$, which is calculated by the guessed displacement $\boldsymbol{D}^{(1)}$

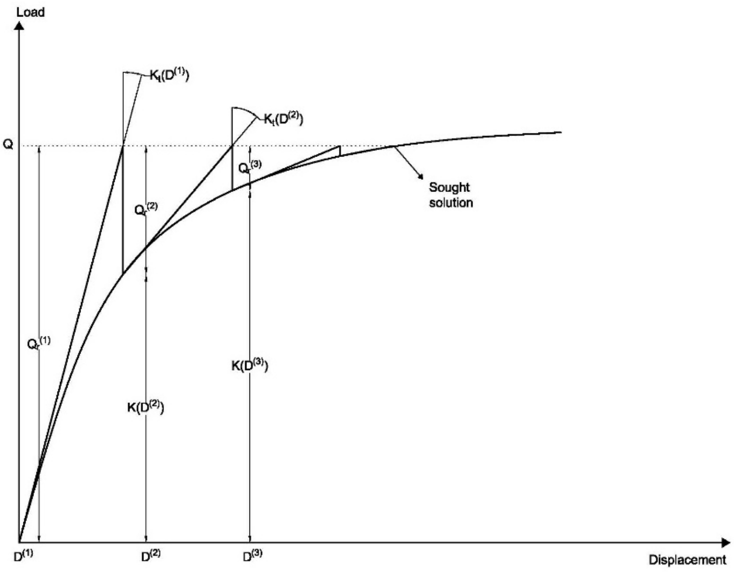

Fig 4.6 Newton-Raphson Method (Ranzi, Gilbert, 2014)

This allows the calculation of the displacement increment $\Delta \boldsymbol{D}^{(1)}$, from which $\boldsymbol{D}^{(2)}$ is obtained. If the convergence criteria is satisfied, no more iteration are required, otherwise another one is carried out with the new tangent stiffness matrix $\boldsymbol{K_t}\left(\boldsymbol{D}^{(2)}\right)$. This process is repeated till the convergence is verified.

In this work the Newton-Raphson algorithm is intended to be used in each time step defined by equation 2.10. For the ease of notation, an index related to the time variable is omitted in the following formulation.

4.4.2 Finite element analysis using the Newton-Raphson method

The Newton-Raphson method applied to finite element approach is based on the steps of the previous paragraph, where the vector of displacements $\boldsymbol{D}^{(i)}$is replaced by the finite element nodal freedoms $\boldsymbol{D}_e^{(i)}$of the assembled structure . The equations 4.16 and 4.17 can be adapted as follows:

$$\boldsymbol{K_t}\left(\boldsymbol{D_e^{(i)}}\right)\Delta\boldsymbol{D}_e^{(i)} = \boldsymbol{Q}_r^{(i)}$$

$$\boldsymbol{Q}_r^{(i)} = \boldsymbol{Q} - \boldsymbol{K}(\boldsymbol{D}_e^{(i)}) \tag{4.19}$$

(4.20)

In which $\boldsymbol{Q}$ and $\boldsymbol{Q}_r^{(i)}$ are expressed in terms of nodal freedoms. The norms for the convergence criteria shown in equation (4.18) are re-written based on the finite element nodal displacement or the residual actions:

$$norm_1 = \frac{\left|\Delta \boldsymbol{D}_e^{(i)}\right|}{\left|\boldsymbol{D}_e^{(i+1)}\right|}$$

$$norm_2 = \frac{\left|\boldsymbol{Q}_R^{(i+1)}\right|}{|\boldsymbol{Q}|}$$

(4.21 a,b)

The derivation of the stiffness matrix and the tangent stiffness matrix for a single finite element will be now described.

We recall equation (4.14), which defines the weak form of the problem expressed in terms of nodal displacements:

$$\int_L \boldsymbol{B}^{\boldsymbol{T}}\boldsymbol{r} \cdot \widehat{\boldsymbol{d}}_{\boldsymbol{e}}\, dx = \int_L \boldsymbol{N}_{\boldsymbol{e}}^{\boldsymbol{T}}\boldsymbol{p} \cdot \widehat{\boldsymbol{d}}_{\boldsymbol{e}}\, dx \qquad \forall\, \widehat{\boldsymbol{d}}_{\boldsymbol{e}}$$

(4.14)

This can be re-arranged to isolate the virtual nodal displacement $\widehat{\boldsymbol{d}}_{\boldsymbol{e}}$ on one side of the dot product:

$$\int_L \boldsymbol{B}^{\boldsymbol{T}}\boldsymbol{r}\, dx \cdot \widehat{\boldsymbol{d}}_{\boldsymbol{e}} = \int_L \boldsymbol{N}_{\boldsymbol{e}}^{\boldsymbol{T}}\boldsymbol{p}\, dx \cdot \widehat{\boldsymbol{d}}_{\boldsymbol{e}} \qquad \forall\, \widehat{\boldsymbol{d}}_{\boldsymbol{e}}$$

Since this equations is valid for each virtual admissible value of $\widehat{\boldsymbol{d}}_{\boldsymbol{e}}$, the following relationship is valid:

$$\int_L \boldsymbol{B}^{\boldsymbol{T}}\boldsymbol{r}\, dx = \int_L \boldsymbol{N}_{\boldsymbol{e}}^{\boldsymbol{T}}\boldsymbol{p}\, dx$$

which is possible to summarize as follows:

$$\boldsymbol{K_e}(\boldsymbol{d_e}) = \boldsymbol{q_e}$$

(4.22)

where

$$\boldsymbol{K_e}(\boldsymbol{d_e}) = \int_L \boldsymbol{B^T r}\, dx$$

(4.23)

defines the vector of the internal actions and

$$\int_L \boldsymbol{N_e^T p}\, dx$$

(4.24)

is the vector of nodal actions describing member loads.

The internal action vector **r** is dependent on the position of the member along the axis *x* and nodal displacements vector **de**. In order to account for the material nonlinearities, the cross sections is discretized in n_j layers (j=1,…,*nj*) of area A_j and centroidal coordinate y_j:

$$\boldsymbol{r}(x, \boldsymbol{de}) = \begin{bmatrix} N(x, \boldsymbol{d_e e}) \\ M(x, \boldsymbol{d_e}) \end{bmatrix} = \begin{bmatrix} \int_A \sigma(x, y, \boldsymbol{d_e}) dA \\ -\int_A y\, \sigma(x, y, \boldsymbol{d_e}) dA \end{bmatrix} = \begin{bmatrix} \sum_{j=1}^{n_j} \sigma(x, y_j, \boldsymbol{d_e}) A_j \\ -\sum_{j=1}^{n_j} y_j\, \sigma(x, y_j, \boldsymbol{d_e}) A_j \end{bmatrix}$$

in which the stress σ is defined by a uniaxial constitutive model, which relates stresses and strain. In this paragraph we refer to it as a generic relationship:

$$\sigma = f(\varepsilon)$$

where in the finite element model:

$$\varepsilon\left(x, y_j, \boldsymbol{d_e}\right) = [1 \quad -y_j]\boldsymbol{B}\boldsymbol{d_e}$$

(4.25)

The two terms $\boldsymbol{K_e}(\boldsymbol{d_e})$ and $\boldsymbol{q_e}$ are evaluated numerically using the Gauss-Legendre formulae:

$$\boldsymbol{K_e}(x, \boldsymbol{d_e}) = \int_L \boldsymbol{B^T}(x)\boldsymbol{r}(x, \boldsymbol{d_e})dx \approx \frac{L}{2}\sum_{k=1}^{n_G} w_k \boldsymbol{B^T}(x_k)\boldsymbol{r}(x_k, \boldsymbol{d_e})$$

(4.26)

$$\boldsymbol{q_e}(x) = \int_L \boldsymbol{N_e^T}(x)\boldsymbol{p}(x)\, dx \approx \frac{L}{2}\sum_{k=1}^{n_G} w_k \boldsymbol{N_e}^{\boldsymbol{T}}(x_k)\boldsymbol{p}(x_k)$$

(4.27)

Where n_G is the number of gauss point along the finite element length where the two quantities are computed. The position of the gauss point is determined by $x_k = \frac{L}{2}(\bar{x}_k + 1)$.

The terms w_k and x_k are the weights and the position of each Gauss point, as provided in the table 4-1:

ng	$\bar{x}_k$	w_k
1	$x_1 = 0$	$w_1 = 2$
2	$x_1 = -0.577350269$	$w_1 = 1$
	$x_2 = 0.577350269$	$w_2 = 1$
3	$x_1 = -0.774596669$	$w_1 = 0.5555556$
	$x2 = 0$	$w_2 = 0.88888888$
	$x_3 = 0.774596669$	$w_3 = 0.5555556$
4	$x_1 = -0.861136312$	$w_1 = 0.3478548$
	$x_2 = -0.339981044$	$w_2 = 0.6521452$
	$x_3 = 0.339981044$	$w_3 = 0.6521452$
	$x_4 =0.861136312$	$w_4 = 0.3478548$
5	$x_1 = -0.906179846$	$w_1 = 0.2369269$
	$x_2 = -0.538469310$	$w_2 = 0.4786287$
	$x_3 = 0$	$w_3 = 0.5688888$
	$x_4 = 0.538469310$	$w_4 = 0.4786287$
	$x5 = 0.906179846$	$w_5 = 0.2369269$
6	$x_1 = -0.932469514$	$w_1 = 0.1713245$
	$x_2 = -0.661209386$	$w_2 = 0.3607616$
	$x_3 = -0.238619186$	$w_3 = 0.4679139$
	$x_4 = 0.238619186$	$w_4 = 0.4679139$
	$x_5 = 0.661209386$	$w_5 = 0.3607616$
	$x_6 = 0.932469514$	$w_6 = 0.1713245$

Table 4-1 Function arguments and weighting factors for the Gauss-Legendre formulae (Ranzi, Gilbert, 2014)

The method requires to compute the tangent stiffness matrix of the single finite element at the i-th iteration:

$$\boldsymbol{K_{et}}\left(x,\boldsymbol{d}^{(i)}{}_{\boldsymbol{e}}\right)=\frac{\partial}{\partial \boldsymbol{d}_e}\int_L \boldsymbol{B^T}(x)\boldsymbol{r}(x,\boldsymbol{d}^{(i)}{}_{\boldsymbol{e}})dx=\int_L \boldsymbol{B^T}(x)\frac{\partial}{\partial \boldsymbol{d}_e}\boldsymbol{r}(x,\boldsymbol{d}^{(i)}{}_{\boldsymbol{e}})dx \tag{4.28}$$

Adopting the same numerical integration as before, equation (4.28) can be approximated by:

$$\boldsymbol{K_{et}}\left(x,\boldsymbol{d}^{(i)}{}_{\boldsymbol{e}}\right)\approx\frac{L}{2}\sum_{k=1}^{n_G}w_k\boldsymbol{B}^{\boldsymbol{T}}(x_k)\frac{\partial}{\partial\boldsymbol{d}_e}\boldsymbol{r}\left(x_k,\boldsymbol{d}^{(i)}{}_{\boldsymbol{e}}\right)$$

$$=\frac{L}{2}\sum_{k=1}^{n_G}w_k\begin{bmatrix}N'_{u1}(x_k) & 0\\ 0 & N''_{v1}(x_k)\\ 0 & N''_{v2}(x_k)\\ N'_{u2}(x_k) & 0\\ N'_{u3}(x_k) & 0\\ 0 & N''_{v3}(x_k)\\ 0 & N''_{v4}(x_k)\end{bmatrix}\begin{bmatrix}\frac{\partial}{\partial\boldsymbol{d_e}}N(x_k,\boldsymbol{d}_e^{(i)})\\ \frac{\partial}{\partial\boldsymbol{d_e}}M(x_k,\boldsymbol{d}_e^{(i)})\end{bmatrix}$$

the partial derivatives can be simplified by using the chain rule as follows:

$$\frac{\partial}{\partial\boldsymbol{d_e}}N\left(x_k,\boldsymbol{d}_e^{(i)}\right)=\int_A\frac{\partial\sigma\left(x_k,y,\boldsymbol{d}_{\boldsymbol{e}}^{(\boldsymbol{i})}\right)}{\partial\boldsymbol{d_e}}dA$$

$$=\int_A\frac{\partial\sigma\left(x_k,y,\boldsymbol{d}_{\boldsymbol{e}}^{(\boldsymbol{i})}\right)}{\partial\boldsymbol{\varepsilon}}\frac{\partial\boldsymbol{\varepsilon}\left(x_k,y,\boldsymbol{d}_{\boldsymbol{e}}^{(\boldsymbol{i})}\right)}{\partial\boldsymbol{d_e}}dA$$

$$\frac{\partial}{\partial\boldsymbol{d_e}}M\left(x_k,\boldsymbol{d}_e^{(i)}\right)=-\int_A y\frac{\partial\sigma\left(x_k,y,\boldsymbol{d}_{\boldsymbol{e}}^{(\boldsymbol{i})}\right)}{\partial\boldsymbol{d_e}}dA$$

$$=-\int_A y\frac{\partial\sigma\left(x_k,y,\boldsymbol{d}_{\boldsymbol{e}}^{(\boldsymbol{i})}\right)}{\partial\boldsymbol{\varepsilon}}\frac{\partial\boldsymbol{\varepsilon}\left(x_k,y,\boldsymbol{d}_{\boldsymbol{e}}^{(\boldsymbol{i})}\right)}{\partial\boldsymbol{d_e}}dA$$

and considering the discretization of the cross-section:

$$\frac{\partial}{\partial \boldsymbol{d_e}} N\left(x_k, \boldsymbol{d}_e^{(i)}\right) = \int_A \frac{\partial \sigma\left(x_k, y, \boldsymbol{d_e^{(i)}}\right)}{\partial \boldsymbol{\varepsilon}} \frac{\partial \boldsymbol{\varepsilon}\left(x_k, y, \boldsymbol{d_e^{(i)}}\right)}{\partial \boldsymbol{d_e}} dA$$

$$\approx \sum_{j=1}^{n_j} A_j \frac{\partial \sigma\left(x_k, y_j, \boldsymbol{d_e^{(i)}}\right)}{\partial \boldsymbol{\varepsilon}} \frac{\partial \boldsymbol{\varepsilon}\left(x_k, y_j, \boldsymbol{d_e^{(i)}}\right)}{\partial \boldsymbol{d_e}}$$

$$\frac{\partial}{\partial \boldsymbol{d_e}} M\left(x_k, \boldsymbol{d}_e^{(i)}\right) = -\int_A y \frac{\partial \sigma\left(x_k, y, \boldsymbol{d_e^{(i)}}\right)}{\partial \boldsymbol{\varepsilon}} \frac{\partial \boldsymbol{\varepsilon}\left(x_k, y, \boldsymbol{d_e^{(i)}}\right)}{\partial \boldsymbol{d_e}} dA$$

$$\approx -\sum_{j=1}^{n_j} y_j A_j \frac{\partial \sigma\left(x_k, y_j, \boldsymbol{d_e^{(i)}}\right)}{\partial \boldsymbol{\varepsilon}} \frac{\partial \boldsymbol{\varepsilon}\left(x_k, y_j, \boldsymbol{d_e^{(i)}}\right)}{\partial \boldsymbol{d_e}}$$

The partial derivatives of the stress depend on the material in the layer j and on the type of constitutive model.

The tangent stiffness matrix, and the loading vector for the entire structure have to be assembled starting from the contributions of the individual elements produced by equations 3.26, 3.27 and 3.29. This can be achieved following standard finite element procedures.

4.5 Cross-sectional modelling

4.5.1 Concrete area discretization

The cross-section is subdivided through the depth D in n layers of constant thickness t (figure 4.7).

If bars or voids are present in layer z, the area of those has to be subtracted to the area of concrete's strip.

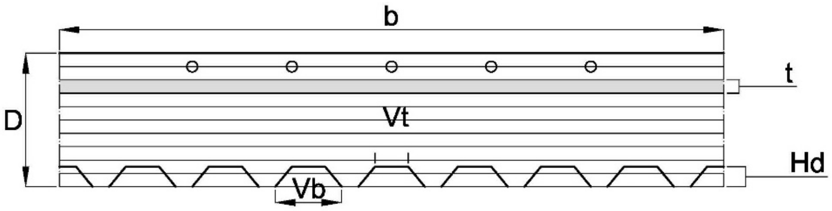

Fig 4.7 Concrete strip area

The stress in the z-th layer of concrete is assumed constant and it is calculated at the centroid of the layer as shown in figure 4.8. Equation (2.14) has been used as constitutive law for concrete, which is recalled in the following:

$$\sigma_{c,j} = E_{c,j}(\varepsilon_j - \varepsilon_{sh,j}) - \sum_{i=0}^{j-1} F_{e,j,i}\sigma_{c,i} \tag{2.14}$$

It is worth to notice that, in this equation, the index j refers to the j-th time step and the index i refers to the previous time steps.

The term ε_j is computed by equation (4.25), $\varepsilon_{sh,j}$ is the value of the free shrinkage deformation on the layer and the term $\sum_{i=0}^{j-1} F_{e,j,i}\sigma_{c,i}$ takes into account the effect of creep due to the stress in the previous time steps $\sigma_{c,i}$.

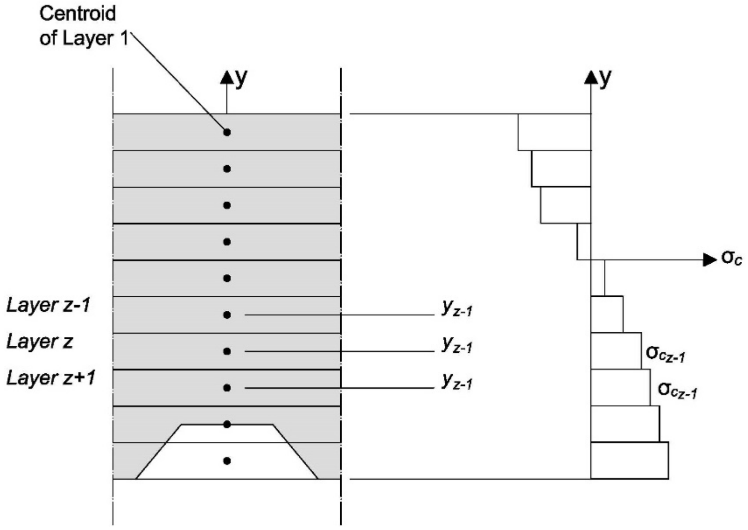
Centroid of Layer 1
y
y
σc
Layer z-1
Layer z
Layer z+1
yz-1
yz-1
yz-1
σcz-1
σcz-1

Fig 4.8 Cross-sectional discretization and stress diagram

4.5.2 Reinforcement discretization

The reinforcement discretization is the same of concrete area.

The area of steel reinforcement on each layer is computed by the integral of circular segment:

$$Ai = \int_{x1}^{x2} \sqrt{r^2 - x^2}\, dx$$

where r (the radius of the bar) and x are shown in figure 4.9. Calling $\sqrt{r^2 - x^2} = f(x)$, the integral is approximated by the composite Simpson's formula:

$$Ai = \int_{x1}^{x2} f(x) \approx \frac{h}{3}\left[f(x1) + f(x2) + 2\sum_{j=1}^{\frac{n}{2}-1} f\left(x_{2j}\right) + 4\sum_{j=1}^{\frac{n}{2}} f\left(x_{2j-1}\right) \right]$$

$$= h/3[f(x_0) + f(x_n) + 4f(x_1) + 2f(x_2) + \cdots + 4f(x_{n-1})]$$

Where n it's the number of internal subdivisions of the interval ($x2$-$x1$). The coefficient h is equal to:

$$h = (x2 - x1)/n$$

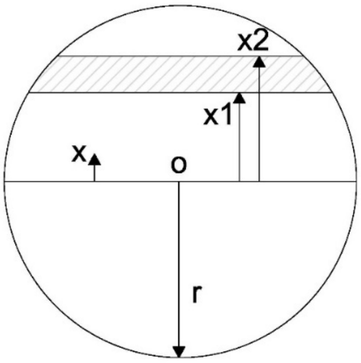

Fig 4.9 Circular segment's area

The program considers also the possibility that the quantity of reinforcement could change along the longitudinal axis of the slab. This could be useful in the case of continuous slabs, where reinforcement is concentrated mainly on the internal supports, while it is not considered around the mid-span area.

4.5.3 Metal sheeting discretization

A database was made to collect the geometric properties (figure 4.10 shows some geometric quantities contained in the database) of the most used profiles in Australia. All the profiles have a trapezoidal shape, and have been discretized with constant thickness layers. The elastic-perfectly plastic constitutive law is applied to the centroid of the layers. The number of layers and their thickness are not the same used for concrete and reinforcement.

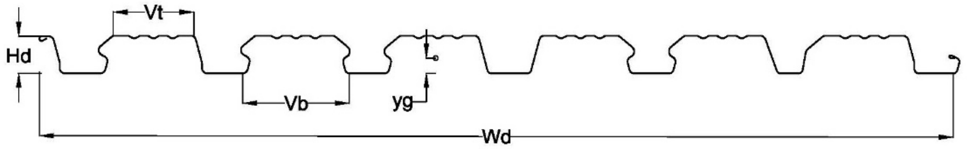

Fig 4.10 Geometric quantities of the metal sheeting

4.6 Validation of the finite element model

The finite element model has been validated by means of experimental results from tests performed on composite slabs at the Laboratory of The School of Civil and Environmental Engineering – The University of New South Wales (Gholamhoseini, 2014).

The experimental program has been already described in Chapter 2. The validation considers slabs 2LT-70-3, 3LT-70-4 and 6LT-40-0. The slabs 2LT-70-3 and 3LT-70-4 are identical and their setup have been already described in Chapter 2.

The long term deflections measured at 42 days and 240 days of drying have been compared with the deflections computed by the model.

The slab 6LT-40-0 was placed onto supports at the age of 7 days and carried only self-weight (3.84 kN/m). The slab has a different sheeting with respect to the others. The deflection at 42 days and 244 days of drying are considered in the model validation.

All the slabs remained uncracked throughout the test period.

Tables 4-2 show the results of the long term deflection for slabs 2LT-70-3 and 3LT-70-4, the ratio of the calculated long-term deflection to the measured long term deflection is also outlined:

SLAB	TEST	LINEAR		UNIFORM	
		CALCULATED	RATIO	CALCULATED	RATIO
2LT-70-3	3.27	3.50	1.07	1.148	0.35
3LT-70-4	2.74	3.50	1.28	1.148	0.42

(a) 42 days of drying

SLAB	TEST	LINEAR		UNIFORM	
		CALCULATED	RATIO	CALCULATED	RATIO
2LT-70-3	6.72	6.75	1.004	2.3863	0.149
3LT-70-4	5.84	6.75	1.155	2.3863	0.198

(b) 240 days of drying

Table 4-2 Validation of the finite element mode

Tables 4-3 are referred to the slab 6LT-40-0:

SLAB	TEST	LINEAR		UNIFORM	
		CALCULATED	RATIO	CALCULATED	RATIO
6LT-40-0	3.77	3.41	0.90	1.35	0.36

(a) 42 days of drying

SLAB	TEST	LINEAR		UNIFORM	
		CALCULATED	RATIO	CALCULATED	RATIO
6LT-40-0	4.99	5.24	1.05	2.3	0.46

(b) 244 days of drying

Table 4-3 Validation of the finite element model

The calculated deflection computed assuming a linear distribution of shrinkage in the finite element model are in good agreement with the time-dependent deflection measured during the test. The uniform shrinkage assumption leads to a severe underestimation of the long term deflection.

Once validated, the finite element model has been used to predict the in-service behaviour of composite slabs, in terms of cracked region and total and incremental deflection.

5 Refined Design Analysis

5.1 Introduction

This chapter presents the results of the application of the finite element method (FEA) to the design of composite steel-concrete structures.

The same case studies of chapter 3 have been considered and the FEA results have been used to evaluate the accuracy of the simplified design service models.

In the first part of the chapter, the FEA has been used to identify a suitable slab thickness which satisfy the serviceability limit state requirements by considering shrinkage effects based on the gradient representation.

In the second part of the chapter, the finite element analysis takes as input the thickness of the slabs designed according to (AS2327 Draft, 2015) for the linear shrinkage profile and to the (AS3600, 2009) for the uniform shrinkage profile. The results are then compared in terms of incremental deflection and total deflection.

The chapter provides the results for profile sheeting 1 (figure 3.5a), since the same considerations are valid also for profile 2 (figure 3.5b), whose results are described in the appendix.

5.2 Design of the thickness using FEA

Figures 5.1 and 5.2 show the thicknesses obtained with FEA and simplified procedure based on (AS2327 Draft, 2015). The ratios of the thickness computed by code's simplified approach to the thickness computed by FEA are also depicted.

For the ease of notation, the results obtained with the simplified approach are referred to as "Code" in the following.

When the incremental check is considered in the design, the FEA returned slightly higher values of thicknesses of the slabs than the analysis from code (figure 5.1).

Conversely, the code model produced higher values of the slab depth than the FEA if the incremental check is removed, as shown in figures 5.2.

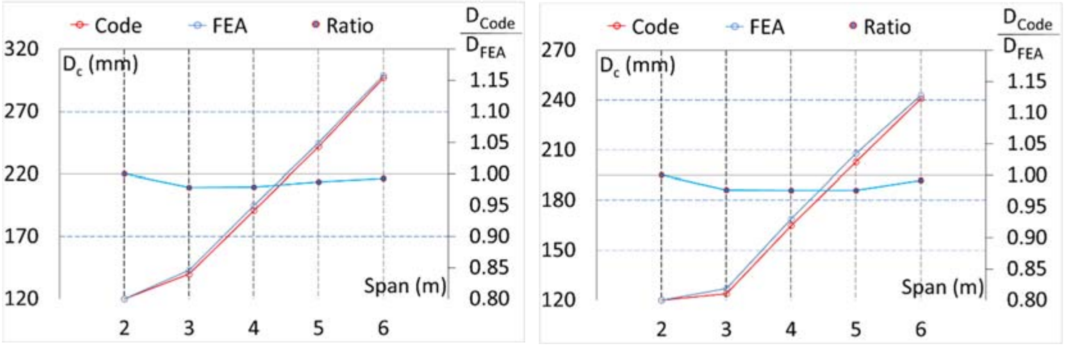

(a) Propped (b) Unpropped

Fig 5.1 Comparison on the designed depth between Code and FEA for profile 1, with incremental check (Q=3 kPa)

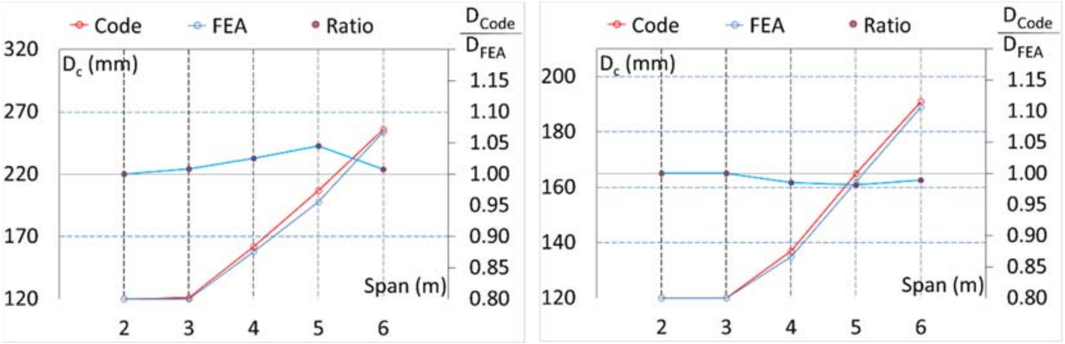

(a) Propped (b) Unpropped

Fig 5.2 Comparison on the designed depth between Code and FEA for profile 1, with no incremental check (Q=3 kPa)

The next sections show in detail the two cases, incremental deflection and total deflection, to better investigate the results obtained in this section.

5.3 Comparisons on deflection between FEA and code approach

5.3.1 General remarks

In this paragraph, the depth of the slabs designed according to codes (AS2327 Draft, 2015; AS3600, 2009) has been used as input in the refined analysis.

The deflection values from finite element and code analysis are reported in tables followed by their ratios $\delta_{\mathrm{Code}}/\delta_{\mathrm{FEA}}$. The last two columns of the tables report the inertia ratio for the code approach $I_{\mathrm{eff}}/I_{\mathrm{uncr}}$ and for the refined approach $I_{\mathrm{eq}}/I_{\mathrm{uncr}}$. The former expresses the ratio between the effective second moment of area I_{eff} (equation 3.5) and the uncracked inertia of the slab I_{uncr}. The latter is related to the quantity I_{eq}, which is an average value of inertia in relation to the extent of the cracked portion of the slab. It is computed according to the following equation:

$$I_{eq} = \frac{I_{cr,av}L_{cr} + I_{uncr}L_{uncr}}{L}$$

in which the term L_{cr} is the length of the portion of the slab in which cracks occurs, L_{uncr} is the uncracked length of the slab and $I_{\mathrm{cr,av}}$ is an average value of the cross-sectional inertia in the cracked portion of the slab. Its value refers to the final time of the analysis.

Despite the terms I_{eq} and I_{eff} are different from each other, they both represent the level of cracking on the slab. When the slab is uncracked, the two inertia ratios are equal to one. When the slab is cracked, the two inertia ratios are less than one.

5.3.2 Incremental deflection

The section considers the cases in which the incremental check has been taken into account for the composite slab design. Tables 5-1 shows the results for slabs with metal sheeting profile 1, considering a linear shrinkage profile:

Incremental Deflection						
L_{span}	Depth	$\delta_{incr\text{-}Code}$	$\delta_{incr\text{-}FEA}$	$\delta_{Code}/\delta_{FEA}$	I_{ef}/I_{uncr}	I_{eq}/I_{uncr}
[m]	[mm]	[mm]	[mm]	[.]	[.]	[.]
2	120	2.46	2.55	0.96	1.00	1.00
3	140	5.52	5.72	0.96	1.00	1.00
4	191	7.40	7.66	0.97	1.00	1.00
5	242	9.34	9.65	0.97	1.00	1.00
6	297	11.23	11.51	0.98	0.98	1.00

(a) Propped

Incremental Deflection						
L_{span}	Depth	$\delta_{incr\text{-}Code}$	$\delta_{incr\text{-}FEA}$	$\delta_{Code}/\delta_{FEA}$	I_{ef}/I_{uncr}	I_{eq}/I_{uncr}
[m]	[mm]	[mm]	[mm]	[.]	[.]	[.]
2	120	2.22	2.30	0.97	1.00	1.00
3	124	5.47	5.66	0.97	1.00	1.00
4	165	7.31	7.56	0.97	1.00	1.00
5	203	9.19	9.48	0.97	1.00	1.00
6	241	10.97	11.29	0.97	1.00	1.00

(b) Unpropped

Table 5-1 Comparison on the incremental deflection between Code and FEA for profile 1 (linear shrinkage, Q=3 kPa)

The two approaches produce similar value of incremental deflection. The cracking condition does not influence the results in this case, because the slabs are uncracked for both the two approaches (except slab with span length equal to 6 m).

The analyses based on code return slightly non-conservative values with respect to the ones from FEA. This result is consistent with the one shown in section 5.2 when the incremental check is considered in the design.

5.3.3 Total deflection

In this paragraph, the incremental check has not been considered within the design criteria and the comparisons are focused on the total deflection values. Tables 5-2 shows the results for slabs with profile 1:

Total Deflection						
L_{span}	Depth	$\delta_{tot\text{-}Code}$	$\delta_{tot\text{-}FEA}$	$\delta_{Code}/\delta_{FEA}$	I_{ef}/I_{uncr}	I_{eq}/I_{uncr}
[m]	[mm]	[mm]	[mm]	[.]	[.]	[.]
2	120	4.30	4.42	0.97	1.00	1.00
3	121	11.88	11.73	1.01	0.86	1.00
4	162	15.99	15.29	1.05	0.78	1.00
5	207	19.90	18.36	1.08	0.71	1.00
6	256	23.88	23.37	1.02	0.65	0.90

(a) Propped

Total Deflection						
L_{span}	Depth	$\delta_{tot\text{-}Code}$	$\delta_{tot\text{-}FEA}$	$\delta_{Code}/\delta_{FEA}$	I_{ef}/I_{uncr}	I_{eq}/I_{uncr}
[m]	[mm]	[mm]	[mm]	[.]	[.]	[.]
2	120	3.93	4.04	0.97	1.00	1.00
3	120	9.71	9.98	0.97	1.00	1.00
4	135	15.84	16.28	0.97	1.00	1.00
5	162	19.96	20.48	0.97	1.00	1.00
6	189	23.88	24.46	0.98	1.00	1.00

(b) Unpropped

Table 5-2 Comparison on the total deflection between Code and FEA for profile 1 (linear shrinkage, Q=3 kPa)

In table 5-2a it is shown that the code produces conservative results (i.e ratios of the incremental deflection ($\delta_{Code}/\delta_{FEA}$ larger than one) when the values of the code inertia ratio are lower than the values of the FEA inertia ratio. It means that the code approach produced more cracks than the refined approach.

If the slab is uncracked in both models, FEA returns higher deflections than the code approach.

5.3.4 Considerations on uniform shrinkage model

Tables 5-3 shows the results assuming a uniform shrinkage profile and considering the incremental check as design criterion:

		Incremental Deflection				
L_{span} [m]	Depth [mm]	$\delta_{incr\text{-}Code}$ [mm]	$\delta_{incr\text{-}FEA}$ [mm]	$\delta_{Code}/\delta_{FEA}$ [.]	I_{ef}/I_{uncr} [.]	I_{eq}/I_{uncr} [.]
2	120	2.16	1.77	1.33	0.62	1.00
3	136	5.96	4.95	1.20	0.49	0.90
4	177	7.93	5.79	1.37	0.53	1.00
5	223	9.89	7.18	1.38	0.53	1.00
6	274	11.95	8.48	1.41	0.52	1.00

(a) Propped

		Incremental Deflection				
L_{span} [m]	Depth [mm]	$\delta_{incr\text{-}Code}$ [mm]	$\delta_{incr\text{-}FEA}$ [mm]	$\delta_{Code}/\delta_{FEA}$ [.]	I_{ef}/I_{uncr} [.]	I_{eq}/I_{uncr} [.]
2	120	1.44	1.52	0.95	1.00	1.00
3	120	5.98	4.18	1.43	0.56	1.00
4	145	7.74	6.14	1.26	0.70	1.00
5	169	9.74	8.20	1.19	0.77	1.00
6	193	11.87	10.31	1.15	0.81	1.00

(b) Unpropped

Table 5-3 Comparison on the incremental deflection between Code and FEA for profile 1 (uniform shrinkage, Q=3 kPa)

The ratios of the incremental deflection $\delta_{Code}/\delta_{FEA}$ are larger than one (excluding the unpropped slab of span length equal to 2 m). The code approach results in larger deflections than those calculated with the finite element model.

The values of the code inertia ratio are quite low, while almost all the values of FEA inertia ratio are equal to one.

In this case, the two models exhibit larger differences than the those observed for the linear shrinkage case.

In summary, this chapter has shown the differences on the design using the finite element approach and the simplified approach based on the Australian codes (AS3600, 2009; AS2327 Draft, 2015).

Considering a linear shrinkage profile through the depth of the slab, the two approaches return similar results. It was noted that the code is leads to slightly smaller deflections than the FEA, when the analysis based on the code model returns uncracked slabs. These differences could be eliminated by modifying the coefficient multiplying φ_{cc} in the calculation of the effective modulus used in the simplified approach, i.e. $E_{ef,sc} = \frac{E_c}{1+0.55\,\varphi_{cc}}$.

The calibration of the ageing coefficient could be performed using the results from FEA as reference. However, the modification of the coefficient would influence all the results: it would also affect the deflection of cracked slabs, which are already more conservative than the FEA deflections (as it was shown in section 5.3.3 and 5.3.4). Further analysis could be done on this topic.

The selection of the 0.55 coefficient (for the calculation of $E_{ef,sc}$) currently included in the draft code (AS2327 Draft, 2015) aimed at maintaining the material representation consistent with European guidelines e.g. (EN 1994-1.1, 2004).

The simplified approach determines higher value of cracking with respect to the FEA. This is due to the different way of accounting for cracking: the code equations evaluate cracks considering the short-term component of the live load (0.7Q) and the shrinkage deformation at the final time of drying. The finite element method evaluates cracks along the time considering the long-term component of the live load (0.4Q), the appropriate shrinkage deformation at i-th time step and the effect of the creep (i.e reduction of the tensile stress on the bottom of the slab).

The slabs are more likely to crack when the incremental check is not considered for the design because in this case the total deflection limit governs the design which leads to thinner slabs (i.e. therefore, more prone to cracking).

In the case of unpropped configuration, the slabs are less likely to crack than the slabs prepared with propped construction. In the case of unpropped construction, the self-weight of the wet concrete is carried by the steel sheeting which acts as permanent formwork, while all loads applied after the removal of the props are resisted by the composite action. In the case of propped construction, the composite member resists all applied loads, including its self-weight.

The simplified approach produces more cracking when a uniform shrinkage distribution is considered with respect to a linear shrinkage distribution. This is because the linear shrinkage profile presents a free shrinkage deformation at the bottom of the slab which is 0.2 times the same quantity of the uniform shrinkage (see equations 2.17 and 2.18). Considering equations (3.6) and (3.7), it can be understood that the value of σ_{cs} is high for uniform shrinkage profile and M_{cr} is more penalized than the linear shrinkage case.

6 Conclusions

6.1 Introduction

The outcomes of this study are summarized and conclusion based on this study are presented in this chapter followed by the recommendations for future work.

6.2 Concluding remarks

This thesis represents a preliminary evaluation of the instantaneous and time dependent behaviour of composite steel-concrete slabs. Particular attention is given to a review of the design serviceability models available in current international guidelines and literature.

In chapter 3, a parametric study has been performed for the design of composite steel-concrete slab. The slab length has been varied and the thickness of the slab has been obtained.
The design has taken into consideration the ultimate limit states and the serviceability limit states of composite slabs. The ultimate limit states formulation is based on the Australian draft code for composite steel concrete structures (AS32327 Draft, 2015). Three serviceability models has been considered which are based on three different assumptions: linear shrinkage profile through the depth of the slab (model A), uniform shrinkage profile through the depth of the slab (model B), and no shrinkage effect considered (model C).

The results of this chapter highlights the serviceability limit states govern the design of composite steel-concrete slab: the incremental deflection governs the design in all the considered cases for linear shrinkage model (model A) and uniform shrinkage model (model B). The total deflection is the most restrictive design criterion when the incremental check is omitted. The ultimate limit states never affect the design and are far to be overpassed.

The ultimate limit states are slightly more important in the model C than the ultimate limit states in models A and B. For small spans they could be significant if the lower limit on thickness (120 mm) is neglected.

In general, the differences on the three models tend to amplify for large span. This is due to the fact the shrinkage deflection linearly depends on the span length. If the span is large, the shrinkage deflection tend to get importance on the overall deflection.

The three models result different values of designed thickness of the slab. The model C returns the smallest value of depths and is the most non-conservative model. The differences between the linear shrinkage and uniform shrinkage models are lower but still significant: the model A is always more conservative than model B for large span. The model A has been resulted less conservative than model B occasionally, when the slab length is not large (approximately up to 3 m). This is because the effects of shrinkage on the overall deflection are not so important in these cases and model B considers the slab more cracked than the model A. A more cracked slab tends to deflect more than an uncracked slab, then it is necessary a thicker slab to satisfy the deflection limits.

These trends are valid for both propped and unpropped slabs. A slab can be cast without using props when its span length is approximately up to 3 m. The most important results obtained for the unpropped configuration are for span length in this range.

In general, the design of unpropped slabs result thinner thickness than the design of propped slab. This is because the metal sheeting of an unpropped slab is free to deflect in the casting stage. The self-weight can be considered applied only to the metal sheeting. Furthermore, the deflection is measured from the top of the concrete slab, then it is zero at the point in the time when the slab is leveled. For this reason, the calculation of the instantaneous deflection is carried out without the contribution of self-weight.

All the comparisons have highlighted the importance of the serviceability limit state on the design. In particular, the results emphasize the importance of including shrinkage effects in the deflection calculation. Linear shrinkage model is recommended to use, because validated against long-term test on composite slabs.

Despite the differences on the design results of the three models, real slabs do not use to suffer of excessive deflection in real structures (except for isolated cases). Possible explanations can be done. Real slabs use to be continuous over two spans (at least). International standards allow to consider a continuous slab as a series of simply supported slabs. However, a continuous slab tends to deflect less than a simply supported slab.

Another possible explanation is the floor finishes could influence the drying shrinkage. The floor finishes could mitigate the shrinkage effects and the deflection of the slab.

Moreover, it is worth to outline the aim of the presented models is the design of composite slab, providing a good safety margin with respect to real structures.

Chapter 4 presented the non-linear finite element model for the solution of the serviceability limit states of composite slabs (FEA). The model has been validated with experimental test performed by the School of Civil and Environmental Engineering of The University of New South Wales (Gholamhoseini, 2014). As a matter of comparison, FEA has been performed for both the three models of shrinkage. It has been notice that the linear shrinkage is the best way of modeling the effect of shrinkage on the slab deflection.

Chapter 5 compares the design results based on codes and FEA.

The models differ to each other on the evaluation of cracking. The code model result higher level of cracking than the finite element model. The code equations evaluate cracks considering the short-term component of the live load and the shrinkage deformation at the final time of drying. The finite element evaluates cracks along the time considering the long-term component of the live load and the appropriate shrinkage deformation at i-th time step. The finite element considers the reduction in the tensile stress on the bottom of the slab due to creep effects.

The differences on the two models are amplified for the uniform shrinkage profile. As already explained above, the uniform shrinkage determines more cracks as the linear shrinkage.

Both the models result unpropped slabs less cracked than propped slabs, because the self-weight load is not considered in the instantaneous load combination of unpropped slabs.

The comparisons have shown the two models give similar results for linear shrinkage profile. However, the code approach results less conservative than FEA if the slab is considered uncracked by the models. This is due to the fact the code approach uses the age-adjusted effective modulus method for accounting the shrinkage effects. The ageing coefficient is the same for the case of cracked and uncracked slabs.

It is not possible to have a perfect calibration of the coefficient for both the configurations. The current value is a good compromise for cracked and uncracked slabs. The ageing coefficient value of the code (AS32327 Draft, 2015) is contained in other international guidelines (EN 1994-1.1, 2004).

The code approach results more conservative than FEA if the slab is considered to be cracked by the code model (or both).

The differences between the two models get higher in the case of uniform shrinkage approach, because of the high level of cracks reported by the code model (as already explained).

6.3 Recommendations for future work

The following areas of research might be considered as the basis of the future research work to extend the work presented in this thesis:

1. Evaluation of the shrinkage effects on the response of continuous slabs:

   The study evaluates the behaviour of simply supported slabs. Real slabs use to be continuous over two spans. This work should be extended to statically indeterminate slabs. In this case creep and shrinkage can lead to a significant change in the support reactions, and hence significant changes in the internal actions on the slabs.

   It is possible the occurrence of cracking on the concrete in proximity of internal supports. Cracking limit state has to be considered for taking into account the corrosion on the top reinforcement of the slab.

2. Influence of the floor finishes on the drying shrinkage:

   The shrinkage strain profile through the depth of real slabs could be different from the one of slabs tested in laboratory. It is possible the floor finishes influence the drying shrinkage of real slabs.

   Experimental studies could be performed to evaluate the influence of floor finishes on the shrinkage profile. It would be possible to identify finishes which mitigate the effect of shrinkage. This would allow to design thinner slab than at present.

3. Calibration of the ageing coefficient of the effective modulus of shrinkage:

   The study highlighted the approach of the draft code (AS32327) is not always more conservative than the finite element model. A possible solution should be the calibration of the ageing coefficient of the effective modulus used in the shrinkage deflection. The calibrated coefficient needs to well adapt to both cracked and uncracked slabs.

References

Abdullah, Samuel Easterling. (2009). New evaluation and modeling procedure for horizontal shear bond in composite slabs. *Journal of Constructional Steel Research*, 891-899.

Al-Deen, R. V. (2011). Full-scale long-term and ultimate experiments of simply supported composite beams with steel deck. *J Constr Steel Res*, 1658-1676.

Al-deen, Ranzi. (2015). Effects of non-uniform shrinkage on the long-term behavior of composite steel-concrete slabs. *International journal of steel structures.*

Al-deen, Ranzi. (2015b). Effects of non-uniform shrinkage on the long-term behavior of composite steel-concrete slabs. *International journal of steel structures.*

Al-deen, Ranzi, Uy. (2015). Non uniform shrinkage in simply-supported composite steel-concrete slabs. *Steel and Composite Structures, An International Journal.*

Al-Deen, Ranzi, Vrcelj. (2011). Full Scale Long-Term and ultimate experiments of simply supported composite beams with steel deck. *J Constr Steel Res.*

AS2327 Draft. (2015).

AS3600. (2009).

Bazant. (1972). Prediction of concrete creep effects using age'adjusted effective modulus method. *American Concrete Institute Journal, 69*(4), 212-217.

Bode Sauerborn. (n.d.).

Bode, Dauwell. (1999). Steel-concrete composite slabs - design based on partial connection. *Proceedings of Steel and Composite Structures International Conference.* Delft.

Bode, Sauerborn. (1992). Modern design concept for composite slabs with ductile behaviour. *Proceeding of conference on composite construction in steel and concrete II* (pp. 125-141). ASCE.

Bradford. (2010). Generic modelling of compoaite steel-concrete slabs subjected to shrinkage, creep and thermal strains including partial interaction. *Eng struct.*

CEB. (1984). Design Manual on structural effects of time-dependent behaviour of concrete CEB. *Comite' Euro International du Beton.*

Dilger, Neville. (1971). Metohd of creep analysis of structural members. *ACI.*

EN 1992-1-1. (2004).

EN 1994 - 1.1. (2004).

Ghali, Favre. (1986). Stress and deformations of composite members. *Chapman and Hall.*

Gholamhoseini, A. (2014). *Time-dependent behaviour of composite concrete slabs.*

Gilbert. (1988). Time-dependent analysis of composite steel-concrete sections. *Elsevier Science Publishers.*

Gilbert, Bradford, Gholamhoeiseni, Chang. (1999). The effects of shrinkage on the long-term deformation of composite concrete slabs. *Proceedings of Eurosteel.*

Gilbert, Bradford, Gholamhoseini, Chang. (2011). Effect of shrinkage on the long term stresses and deformations of composite concrete slabs. *Proceedings of CONCRETE.*

Gilbert, Ranzi. (2010). *Time-dependent behaviour of concrete structures.* London: Spon Press.

Johnson. (2004). *Composite Structures of Steel and Concrete.* Blackwell Publishing.

Koukkari. (1999). Steel sheet in a post-tensioned composite slab. *Proceedings of Eurosteel*, 199-201.

Krell. (1977). Composite Steel-Deck Concrete Floor Systems - Discussion of the Paper. *Journal Of the Structural Division ASCE Vol 103.*

McHenry. (1943). A new aspect of creep in concrete and its application to design. *Proceedings of the ASTM*, *43*, pp. 1069-1084.

Montgomery, Kulak, Shwartsburd. (1983). Deflections of a composite floor system. *Can J Civ Eng*, 192-204.

Ohlers, Bradford. (1999). *Elementary Behaviour of Composite Steel and Concrete Structural Mewmbers.* Oxword:Butterworth-Heinemann.

Ong, Mansu. (1986). Shear-bond capacity of composite slabs made with profiled sheeting. *The International Journal of Cement Composites and Lightweight Concrete*, 231-237.

Patrick, Bridge. (1990). *Parameters affecting the design and behaviour of composite slabs.* International Association for Bridge and Structural Engineering.

Patrick, Poh. (1990). Controlled Test for Composite Slab Design Parameters. *IABSE Symposium on Mixed Structures Including New Materials.* Brussels.

Patrick, Russel. (1994). Partial shear connection design of composite slabs. *Engineering Structures, 16.*

Patrick, Russel. (1994). Review of concepts concerning bond of steel decking. *International Speciality Conference on Cold-Formed Steel Structures*, (pp. 335-359).

Poh, Attard. (1991). *Analytical Modelling of Load-Deflection Behaviour of One Way Simply Supported Composite Slabs with Interface Slip.* Monash University Cibil Engineering Report.

Porter, Ekberg. (1975). Design Recommendations for Steel Deck Floor. *International Speciality Conference on Cold-Formed Steel Structures.*

Porter, Ekberg. (1975). Design vs Test Results for Steel Deck Floor Slabs. *International Speciality Conference on Cold-Formed Steel Structures.*

Ranzi, Al-Deen, Ambrogi, Uy. (2013). Long-term behaviour of simply-supported post-tensioned composite slabs. *Journal of Constructional Steel Research.*

Ranzi, Gilbert. (2014). In *Structural Analysis.* CRC Press.

Ranzi, Leoni, Zandonini. (2012). State of the art on the time dependent behavior of composite steel-concrete structures. *Journal of constructional steel research.*

Ranzi, Vrcelj. (2009). Closed form solutions for the long-term analysis of composite steel-concrete members subjected to non-uniform shrinkage distributions.

Proceedings of the 5th International conference on advances in steel structures (ICASS '09); Honk Kong.

Roll. (1971). Effects of differential shrinkage and creep on a composite steel-concrete structure. *ACI special pubblication, 27*, 187-214.

Schuster. (1972). Composite steel-deck-reinforced concrete systems failing in shear-bond. *Ninth Congress of the International Association for Bridge and Structural Engineering.* Zurich.

Stark. (1978). Design of composite floors with profiled steel sheet. *Internationa Speciality Conference on Cold-Formed Steel Structures.*

Stark, Brekelmans. (1990). Plastic deisgn of continuos composite slabs. *J. Construct. Steel Research*, 23-47.

Taplin. (1992). *Testging of Simply Supported Slabs with Inteface Slip.* Master of Engineering Science Minor Thesis, Monash University.

Tazawa , Miyazawa . (1992). Autogenous shrinkage of cement paste with condensed silica fume. *Proceedings of the 4th CANMET/ACI International Conference on Fly Ash, Silica Fume, Slag and Natural Pozzolans in Concrete* (pp. 875-894). ACI.

Tehnovuori, Leskela. (1998). Longitudinal shear resistance of composite slabs. *Journal of Constructional Steel Research*, 46.

Tenhovuori, Karkkainen, Kanerva. (1996). Parameters and definitions for classifying the behaviour of composite slabs. *Proceedings of conference on composite construction in steel and concrete III* (pp. 752-765). ASCE.

Trost. (1967). Auswirkungen des Superpositionsprinzips auf Kriech- und Relaxations-Probleme bei beton und Spannbeton. *Beton- und Stahlbetonbau.*

UY. (1997). Long-term service-load behaviour of simply supported profiled composite slabs. *Proc Inst Civ Enf Struct Build*, 193-208.

Veljkovic. (2000). Behaviour and design of shallow composite slab. *Proceedings of conference on Composite Construction in Steel and Concrete.* Alberta: ASCE.

A1 Material Properties

A.1.1 Concrete

The proprieties and deformations of concrete used in this thesis to predict deflections and cracks widths are the characteristic flexural tensile strength, elastic modulus, creep coefficient and shrinkage strain.

The elastic modulus is needed in the analysis of structures to estimate the stiffness of each member and determinate the internal actions. It is also required to estimate the instantaneous deformations caused by internal actions and stresses induced by imposed deformations. The tensile strength of concrete is required to determinate the extent of cracking due to both applied load and shrinkage. The creep coefficient associated with a particular time period and a particular loading regime is needed to estimate the time-dependent deformation of the structure, and magnitude and rate of shrinkage strain is required to predict the development of load-independent deformations with time and the onset of time-cracking.

This chapter introduces the formulation from Australian Standard for Concrete Structures, AS3600-2009 to predict concrete compressive strength, tensile strength and the elastic modulus. Models are also presented for predicting creep coefficient and shrinkage strains.

A.1.1.1 Strength (AS3600-2009, 3.1.1)

AS3600-2009, 3.1.1.1 The characteristic compressive strengths *fc'* of the standard strength grades are 20 MPa, 25 MPa, 32 MPa, 40 MPa, 50 MPa, 65 MPa, 80 MPa and 100 MPa.

AS3600-2009, 3.1.1.2 In the absence of more accurate data, the mean value of the in situ compressive strength f_{cmi} shall be taken as 90% if the mean value of the cylinder f_{cm}

AS3600-2009, 3.1.1.2 In absence of more accurate data, the characteristic flexural tensile strength of concrete $f'_{ct,f}$ shall be taken as:

$f'_{ct,f} = 0.6\sqrt{f'_c}$ at 28 days and after curing.

AS3600-2009, 3.1.3 For normal-weight concrete, the density ρ may be taken as 2400 kg/m^3

A.1.1.1 Modulus of elasticity (AS3600-2009, 3.1.2)

The mean modulus of elasticity of concrete at the appropriate age E_{cj} shall be either:

$(\rho^{1.5})x(0.043\sqrt{f_{cmi}})$ (In megapascals) when $f_{cmi} \leq 40\ MPa$; or

$(\rho^{1.5})x(0.024\sqrt{f_{cmi}} + 0.12)$ (In megapascals) when $f_{cmi} > 40\ MPa$

An estimate variations of the elastic modulus with time

$$E_c(t) = \left(e^{s(1-\sqrt{28/t}}\right)^{0.5} E_c(28)$$

Where s is a coefficient which depends on the type of cement

=0.25 for cement of strength Classes CEM 32.5 R, CEM 42.5 N (class N)

A.1.1.2 Creep coefficient (AS3600-2009, 3.1.8.3)

If results from tests are not available for predicting creep coefficient, analytical methods are necessary. The approach from AS3600-2009 is presented here. This method does not account for such factors as aggregate type, cement type, cement replacement materials and more, but it does provide an estimate of the creep coefficient for concrete suitable for routine use in structural design.

The creep coefficient at any time may be calculated from:

$$\varphi(t,\tau) = k_2 k_3 k_4 k_5 \varphi_{basic}$$

The basic creep coefficient φ_{basic} is given in table A1-1

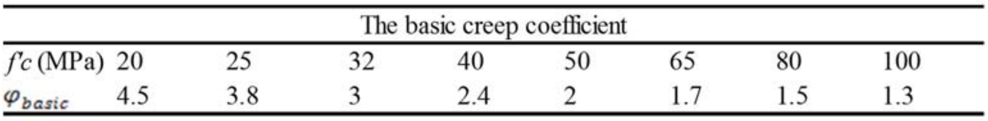

The basic creep coefficient

$f'c$ (MPa)	20	25	32	40	50	65	80	100
φ_{basic}	4.5	3.8	3	2.4	2	1.7	1.5	1.3

Table A- 1 Value for the basic creep coefficient

The factor k_2 describes the development of creep with time. It depends on the hypothetical thickness, t_h, the environment and the time after loading and is given by:

$$k_2 = \frac{\alpha_2 (t - t_0)^{0.8}}{(t - t_0)^{0.8} + 0.15 t_h}$$

$$\alpha_2 = 1.0 + 1.12 e^{-0.008 t_h}$$

The hypothetical thickness is defined as

$$t_h = 2A/u_e$$

Where A is the cross-sectional area of the member and u_e is that portion of the section perimeter exposed to the atmosphere plus half the total perimeter of any voids contained within the section.

The factor k_3 depends on the age at first loading t_0 (in days) and is given by:

$$k_3 = \frac{2.7}{1 + \log(t_0)}$$

The factor k_4 takes into account the environment:

$k_4 = 0.70$ for an arid environment

$k_4 = 0.65$ for an interior environment

$k_4 = 0.60$ for a temperate environment and

$k_4 = 0.50$ for a tropical/coastal environment.

The factor *k5* is a modification factor for high strength, which shall be taken as

$k_5 = 1.0$ for $f'_c \leq 50MPa$; or

$k_5 = (2.0 - \alpha_3) - 0.02(1.0 - \alpha_3)f'_c$ for $f'_c \geq 50MPa$

The factor $\alpha_3 = \dfrac{0.7}{k_2 \alpha_2}$

A.1.1.3 Shrinkage strain (AS3600-2009, 3.1.7)

AS3600-2009, 3.1.7.2 When the design shrinkage strain of concrete (ε_{sh}) is to be calculated, it shall be determined as the sum of the chemical (autogenous) shrinkage strain ($\varepsilon_{sh,e}$) and the drying shrinkage strain $\varepsilon_{sh,d}$.

$\varepsilon_{sh} = \varepsilon_{sh,e} + \varepsilon_{sh,d}$Endogenous shrinkage is taken to be the sum of chemical (or autogenous) shrinkage and thermal shrinkage and is assumed to develop relatively rapidly and to increase with concrete strength. Drying shrinkage develops more slowly and decreases with concrete strength.

The autogenous shrinkage is given by:

$$\varepsilon_{sh,e} = \varepsilon^{*}{}_{sh,e}\left(1.0 - e^{-0.1t}\right)$$

Where t is the time (in days) after setting and $\varepsilon^{*}{}_{sh,e}$ is the final autogenous shrinkage and may be taken as

$$\varepsilon^{*}{}_{sh,e} = (0.06 f'_c - 1.0) \cdot 50 \cdot 10^{-6}$$

At any time after the commencement of drying $(t - t_d)$ the drying shrinkage may be taken as:

$$\varepsilon_{sh,d} = k_1 k_4 \varepsilon_{sh,d,b}$$

Where k_1 is given in by:

$$k_1 = \frac{\alpha_1 (t - t_d)^{0.8}}{(t - t_d)^{0.8} + 0.15 t_h}$$

With

$$\alpha_1 = 0.8 + 1.2 e^{-0.005 t_h}$$

The factor k_4 is the same used for creep coefficient computation.

The basic drying shrinkage $\varepsilon_{sh,d}$ is given by:

$$\varepsilon_{sh,d,b} = (1.0 - 0.008 f'_c) \varepsilon^*{}_{sh,d,b}$$

Where $\varepsilon^*{}_{sh,d,b}$ is the final drying basic shrinkage strain. It shall be taken as $800 \cdot 10^{-6}$ for good aggregate quality and $1000 \cdot 10^{-6}$ when aggregate quality is uncertain

A.1.2 Steel reinforcement (AS3600-2009, 3.2)

AS3600-2009, 3.2.1 Characteristic yield strength for D500L: $f_{sy} = 500\ MPa$

AS3600-2009, 3.2.2 $E_s = 200000\ MPa$

A2 Additional Results Chapter 3

A2.1 Influence of the live load on total deflection

A2.1.1 Profile 1

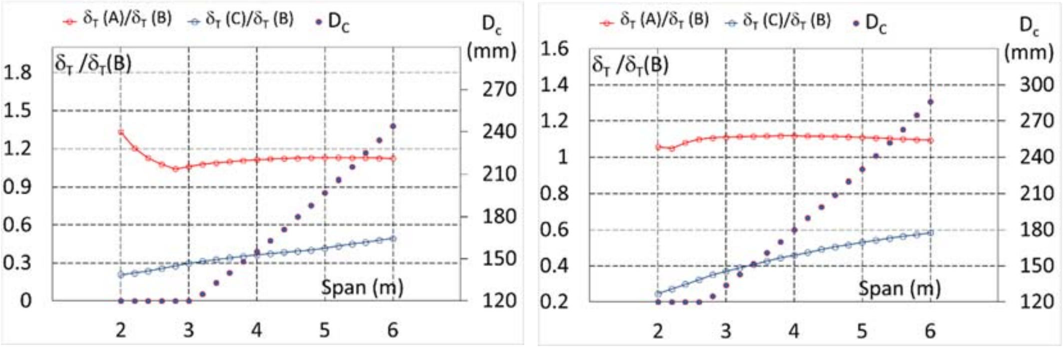

(a) Q = 3 kPa, propped slab (b) Q = 10 kPa, propped slab

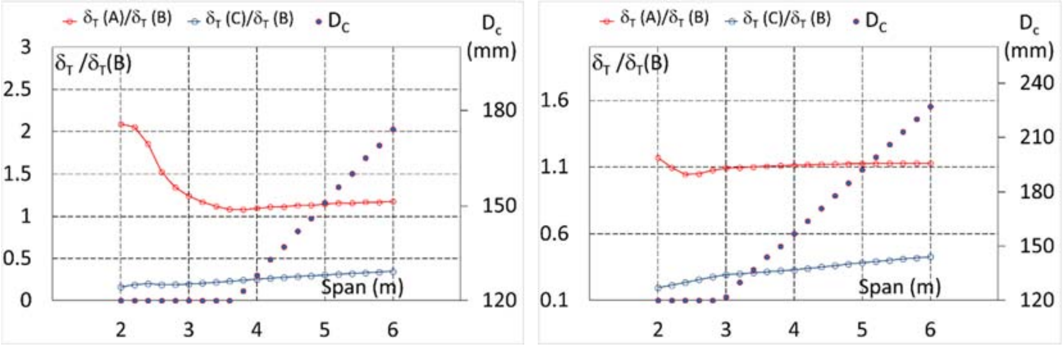

(c) Q = 3 kPa, unpropped slab (d) Q = 10 kPa, unpropped slab

Fig A- 1 Comparisons among total deflection computed using the models A, B and C for the profile 1

A2.1.2 Profile 2

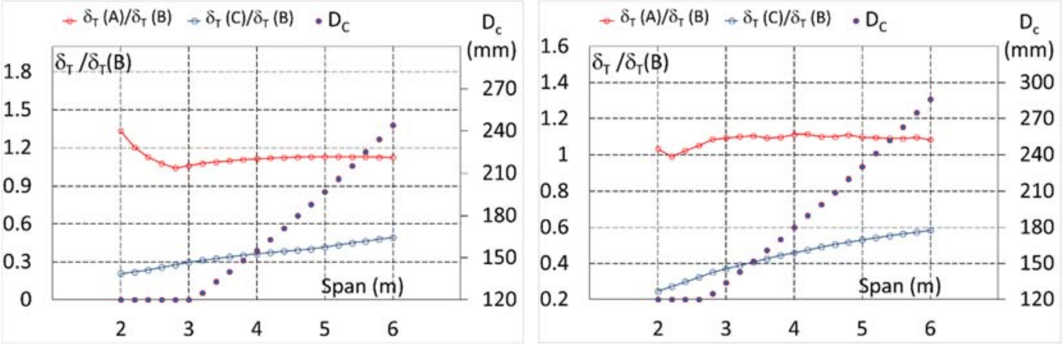

(a) Q = 3 kPa, propped slab (b) Q = 10 kPa, propped slab

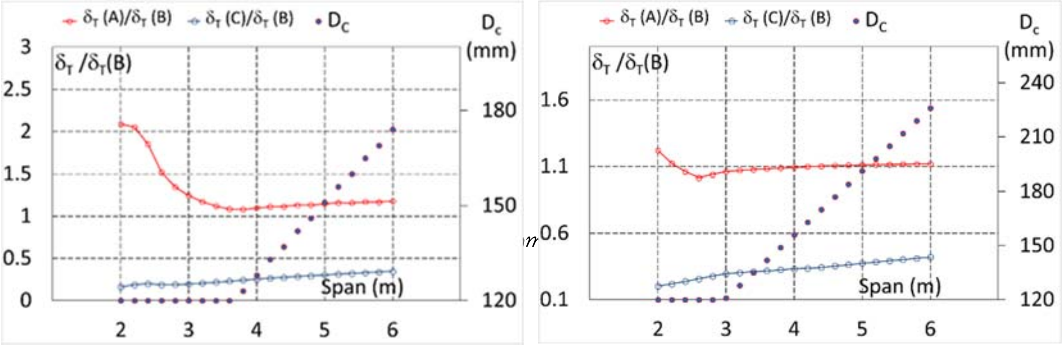

(c) Q = 3 kPa, unpropped slab (d) Q = 10 kPa, unpropped slab

Fig A- 2 Comparisons among total deflection ratio computed using the models A, B and C for the profile 2

A2.2 Influence of the thickness of the profiled on total deflection

A2.2.1 Profile 1

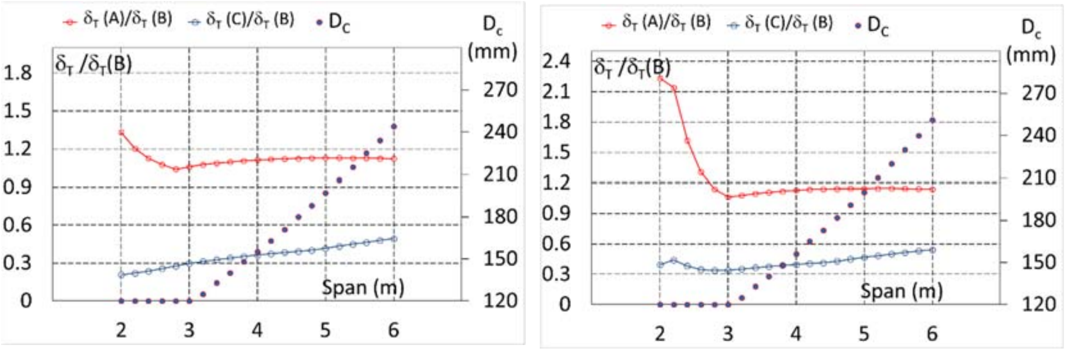

(a) profile thickness = 1 mm
propped slab

(b) profile thickness = 0.6 mm
propped slab

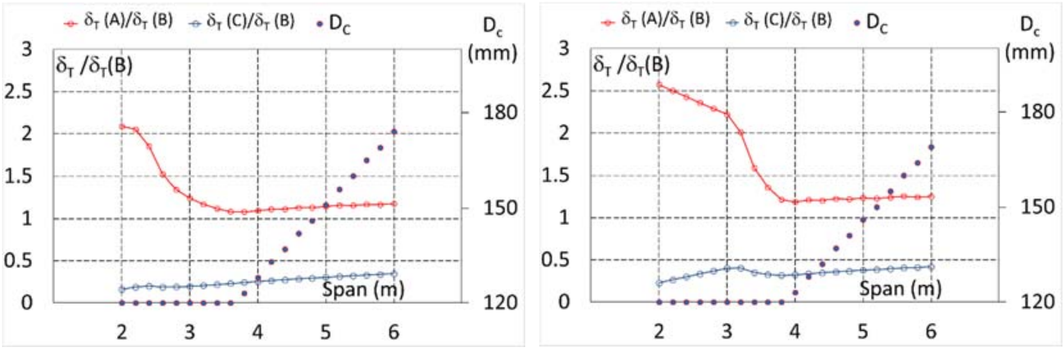

(c) profile thickness = 1 mm
unpropped slab

(d) profile thickness = 0.75 mm
unpropped slab

Fig A- 3 Comparisons among total deflection computed using the models A, B and C for the profile 1

A2.2.2 Profile 2

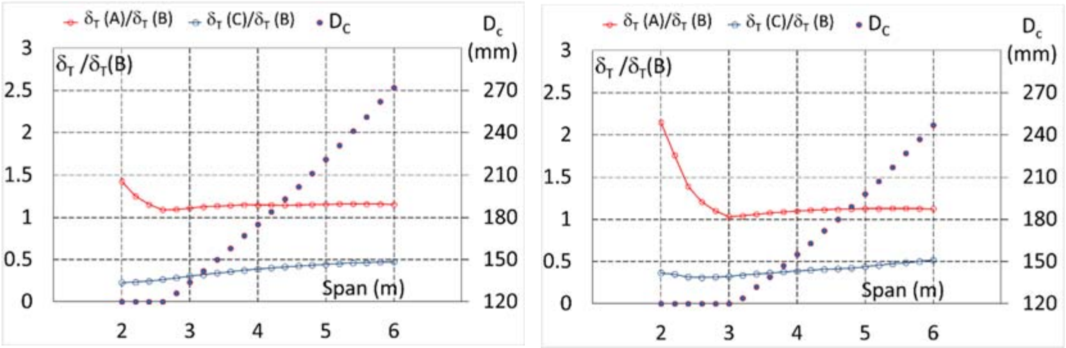

(a) profile thickness = 1 mm
propped slab

(b) profile thickness = 0.75 mm
propped slab

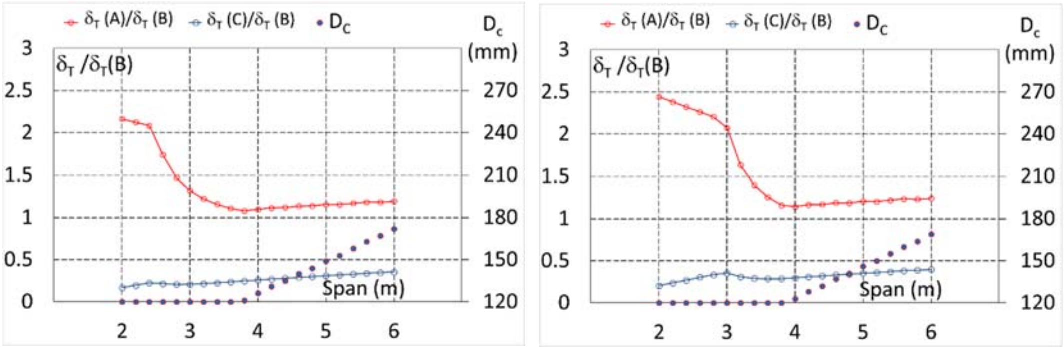

(c) profile thickness = 1 mm
unpropped slab

(d) profile thickness = 0.75 mm
unpropped slab

Fig A- 4 Comparisons among total deflection computed using the models A, B and C for the profile 2

A3 Additional Results Chapter 5

A3.1 Comparisons between FEA and code for slabs with profile 2

A3.1.1 Design of the thickness for profile 2 using FEA

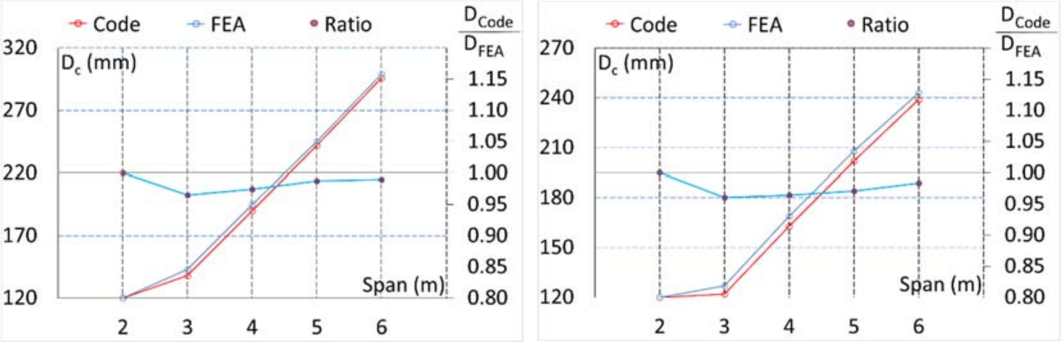

(a) Propped (b) Unpropped

Fig A- 5 Comparison on the designed depth between Code and FEA for profile 2, with incremental check (Q=3 kPa)

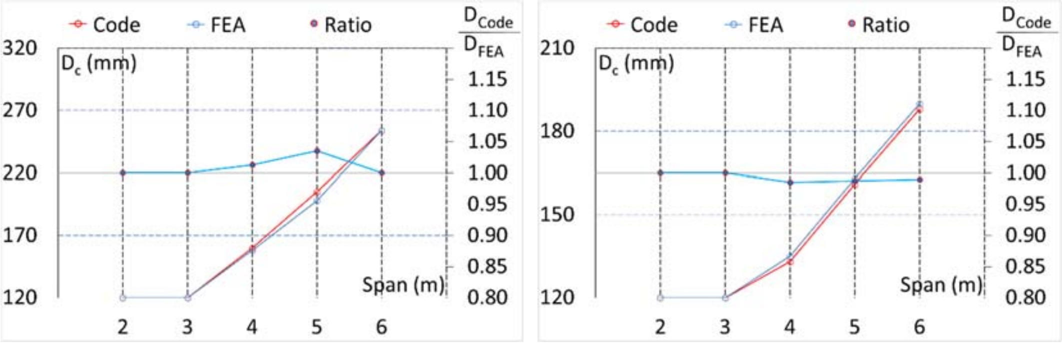

(a) Propped (b) Unpropped

Fig A- 6 Comparison on the designed depth between Code and FEA for profile 2, with no incremental check (Q=3 kPa)

A3.1.2 Comparisons on incremental deflection for profile 2

		Incremental Deflection				
L_{span}	Depth	$\delta_{incr\text{-}Code}$	$\delta_{incr\text{-}FEA}$	$\delta_{Code}/\delta_{FEA}$	I_{ef}/I_{uncr}	I_{eq}/I_{uncr}
[m]	[mm]	[mm]	[mm]	[.]	[.]	[.]
2	120	2.32	2.48	0.94	1.00	1.00
3	138	5.48	5.75	0.95	1.00	1.00
4	190	7.35	7.66	0.96	1.00	1.00
5	242	9.21	9.60	0.96	1.00	1.00
6	296	11.23	11.53	0.97	1.00	1.00

(a) propped

		Incremental Deflection				
L_{span}	Depth	$\delta_{incr\text{-}Code}$	$\delta_{incr\text{-}FEA}$	$\delta_{Code}/\delta_{FEA}$	I_{ef}/I_{uncr}	I_{eq}/I_{uncr}
[m]	[mm]	[mm]	[mm]	[.]	[.]	[.]
2	120	2.11	2.23	0.95	1.00	1.00
3	122	5.54	5.63	0.98	1.00	1.00
4	163	7.37	7.57	0.97	1.00	1.00
5	202	9.22	9.44	0.98	1.00	1.00
6	239	11.22	11.33	0.99	1.00	1.00

(b) unpropped

Table A- 2 Comparison on the incremental deflection between Code and FEA for profile 2 (linear shrinkage, Q=3 kPa)

A3.1.3 Comparisons on total deflection for profile 2

		Total Deflection				
L_{span} [m]	Depth [mm]	$\delta_{tot\text{-}Code}$ [mm]	$\delta_{tot\text{-}FEA}$ [mm]	$\delta_{Code}/\delta_{FEA}$ [.]	I_{ef}/I_{uncr} [.]	I_{eq}/I_{uncr} [.]
2	120	4.20	4.30	0.98	1.00	1.00
3	120	11.42	11.59	0.98	0.97	1.00
4	160	15.92	15.43	1.03	0.82	1.00
5	205	19.90	18.53	1.07	0.74	1.00
6	254	23.91	21.31	1.12	0.67	1.00

(a) propped

		Total Deflection				
L_{span} [m]	Depth [mm]	$\delta_{tot\text{-}Code}$ [mm]	$\delta_{tot\text{-}FEA}$ [mm]	$\delta_{Code}/\delta_{FEA}$ [.]	I_{ef}/I_{uncr} [.]	I_{eq}/I_{uncr} [.]
2	120	3.83	3.92	0.98	1.00	1.00
3	120	9.46	9.67	0.98	1.00	1.00
4	133	15.90	16.28	0.98	1.00	1.00
5	161	19.86	20.34	0.98	1.00	1.00
6	188	23.81	24.34	0.98	1.00	1.00

(b) unpropped

Table A- 3 Comparison on the total deflection between Code and FEA for profile 2 (linear shrinkage, Q=3 kPa)

A3.1.4 Comparisons with uniform shrinkage distribution

Incremental Deflection						
L_{span}	Depth	$\delta_{incr\text{-}Code}$	$\delta_{incr\text{-}FEA}$	$\delta_{Code}/\delta_{FEA}$	I_{ef}/I_{uncr}	I_{eq}/I_{uncr}
[m]	[mm]	[mm]	[mm]	[.]	[.]	[.]
2	120	2.15	1.68	1.28	0.67	1.00
3	134	5.97	4.20	1.42	0.49	1.00
4	175	7.97	5.77	1.38	0.53	1.00
5	221	9.93	7.17	1.39	0.54	1.00
6	272	12.00	8.47	1.42	0.53	1.00

(a) propped

Incremental Deflection						
L_{span}	Depth	$\delta_{incr\text{-}Code}$	$\delta_{incr\text{-}FEA}$	$\delta_{Code}/\delta_{FEA}$	I_{ef}/I_{uncr}	I_{eq}/I_{uncr}
[m]	[mm]	[mm]	[mm]	[.]	[.]	[.]
2	120	1.36	1.43	0.95	1.00	1.00
3	120	5.50	3.96	1.39	0.60	1.00
4	142	7.83	6.15	1.27	0.69	1.00
5	166	9.74	8.22	1.18	0.78	1.00
6	190	11.76	10.33	1.14	0.83	1.00

(b) unpropped

Table A- 4 Comparison on the incremental deflection between Code and FEA for profile 2 (uniform shrinkage, Q=3 kPa)